DOT/FAA/SA-88/1

Advanced System
Acquisition Service
Washington, D.C. 20591

Observations of a Thunderstorm Generated Gust Compared with Solitary Wave Theory

DTIC FILE COPY

R. J. Doviak
NOAA, Environmental Research Laboratories
National Severe Storms Laboratory
Norman, OK 73069

S. Chen
Pennsylvania State University
State College, PA 16801

DTIC
ELECTE
OCT 1 4 1988
C&D

June 1988

Final Report

This document is available to the public
through the National Technical Information
Service, Springfield, Virginia 22161.

U.S. Department of Transportation

Federal Aviation Administration

88 1013 066

NOTICE

1. Report No. DOT/FAA/SA-88/1	2. Government Accession No.	3. Recipient's Catalog No
4. Title and Subtitle OBSERVATIONS OF A THUNDERSTORM GENERATED GUST COMPARED WITH SOLITARY WAVE THEORY		5. Report Date June 1988
		6. Performing Organization Code
7. Author's) R. J. Doviak and S. Chen*		8. Performing Organization Report No.
9. Performing Organization Name and Address National Severe Storms Laboratory 1313 Halley Circle Norman, OK 73069		10. Work Unit No. (TRAIS)
		11. Contract or Grant No. DTFA01-80-Y-10524
		13. Type of Report and Period Covered
12. Sponsoring Agency Name and Address Department of Transportation Federal Aviation Administration Advanced System Acquisition Service Washington D.C. 20590		Final Report
		14. Sponsoring Agency Code FAA/ASA-220

15. Supplementary Notes

* Parts of this report were prepared while the author was at the Cooperative Institute for Mesoscale Meteorological Studies, University of Oklahoma, Norman, Oklahoma.

16. Abstract

Observations suggest that solitary and other nonlinear waves might be a source of wind shear hazard to safe flight, and thus should be studied both experimentally and theoretically. A derivation of the Benjamin-Davis-Ono (BDO) equation by a perturbation method is reviewed and extended to the case in which the fluid is in sheared flow. For nonsheared flows, our solution for the upper layer differs markedly from Benjamin's, which doesn't satisfy his specified boundary conditions. The internal steady-state solitary wave, described by the solution of the BDO equation, is compared with a boundary layer solitary wave observed with NSSL's Doppler radar, a network of eight meteorological stations, and a 444-m-tall instrumented tower. Wave-induced vertical transport of the horizontal momentum of the strongly sheared ambient air contributed much to the observed wind perturbations and horizontal wind shear. It is shown that agreement between the theoretical results of the weakly nonlinear theory of BDO and observations of wind and temperature at the surface is coincidental because wave advection and frictional drag markedly affect wave properties. Only tall tower and Doppler radar measurements above the ground provided the necessary data to determine that the observed solitary wave was strongly nonlinear, and that it trapped thunderstorm outflow, which leaked out the rear of the wave. Wave amplitude data, far above (i.e., ≤ 200 m) the ground, show fairly good agreement with numerical results from strongly nonlinear theory. Wind shear produced by the solitary wave appears to be significant, even though it is 60 km from the storm that initiated it. Because large-amplitude waves have amplitude-dependent speeds, and because the wave-generating thunderstorm traversed the moving atmosphere at an effective "supersonic" velocity, we derived a modified Mach relation to compute wave speed from the measured storm velocity and the convex shape of the wave front. Comparison with wave speeds computed from tracking wave front positions along lines of energy propagation paths show fairly good agreement.

17. Key Words Wind Shear Weather Thunderstorm Solitary Wave Theory	18. Distribution Statement Document is available to the U.S. public through the National Technical Information Service, Springfield, Virginia 22161.

19. Security Classif. (of this report) Unclassified	20. Security Classif. (of this page) Unclassified	21. No. of Pages 144	22. Price

Form DOT F 1700.7 (8-72)   Reproduction of completed page authorized

A

Contents

Preface

ABSTRACT

Observations suggest that solitary and other nonlinear waves might be a source of wind shear hazard to safe flight and thus should be studied both experimentally and theoretically. A derivation of the Benjamin-Davis-Ono (BDO) equation by a perturbation method is reviewed and extended to the case in which the fluid is in sheared flow. For nonsheared flows, our solution for the upper layer differs markedly from Benjamin's, which doesn't satisfy his specified boundary conditions. The internal steady-state solitary wave, described by the solution of the BDO equation, is compared with a boundary layer solitary wave observed with NSSL's Doppler radar, a network of eight meteorological stations, and a 444-m-tall instrumented tower. Wave-induced vertical transport of the horizontal momentum of the strongly sheared ambient air contributed much to the observed wind perturbations and horizontal wind shear. It is shown that agreement between the theoretical results of the weakly nonlinear theory of BDO and observations of wind and temperature at the surface is coincidental because wave advection and frictional drag markedly affect wave properties. Only tall tower and Doppler radar measurements above the ground provided the necessary data to determine that the observed solitary wave was strongly nonlinear, and that it trapped thunderstorm outflow, which leaked out the rear of the wave. Wave amplitude data, far above (i.e., $\gtrsim 200$ m) the ground, show fairly good agreement with numerical results from strongly nonlinear theory. Wind shear produced by the solitary wave appears to be significant, even though it is 60 km from the storm that initiated it. Because large-amplitude waves have amplitude-dependent speeds, and because the wave-generating thunderstorm traversed the moving atmosphere at an effective "supersonic" velocity, we derived a modified Mach relation to compute wave speed from the measured storm velocity and the convex shape of the wave front. Comparison with wave speeds computed from tracking wave front positions along lines of energy propagation paths shows fairly good agreement.

List of Frequently-Used Symbols

c group velocity for a wave of finite amplitude (Eq. 2.26b)

c' Tne prime above and to the right of c denotes the group velocity of the wave in the medium advecting the wave (p. 73).

c_m group velocity of wave (in a still medium) computed using the modified Mach relation (Eq. 3.5)

c_0 phase speed of an extremely long wavelength disturbance of infinitesimal amplitude. It is the eigenvalue of the eigenfunction equation (Eq. 2.12c).

c_{oo} a scaling velocity equal to the speed of a linear wave of extremely long length propagating in a medium composed of two homogeneous layers having a $\Delta\theta_{vo}$ difference in θ_{vo} equal to the total change in θ_{vo} of the actual atmosphere (p. 100)

c_t group velocity (in a still medium) obtained by tracking the wave position along the ray as a function of time (Table 3.1, p. 74)

c_1 the increase in wave speed (group velocity) caused by finite wave amplitude (p. 26)

D_p the direction of the wave's perturbation velocity (Fig. 5b, p. 50)

f a factor of the stream function dependent upon x and t (p. 16)

$\vec{g}$ acceleration due to gravity (p. 11)

H height of the upper boundary where $w = 0$ (p. 101)

$H\{f\}$ Hilbert transform of the function f (p. 8)

h depth of stratified layer lying beneath an open ended neutral layer (p. 7)

h_e the effective height of the radar beam (p. 82)

h_s vertical scale of lower layer stratification (p. 3)

$\vec{k}$ vector wave number (p. 11)

$\ell_{1/2} = 2\lambda$ wave's half-amplitude width perpendicular to the wave front (p. 63)

N Brunt-Väisälä frequency (p. 17)

r radial distance along the radar beam

$s = h_s^{-1}$ reciprocal of vertical scale of lower layer stratification (p. 3)

t time (p. 4)

t_e equivalent time to describe changes in wave characteristics along its front (p. 87)

u horizontal wind component perpendicular to front (p. 13)

u_a, v_a ambient wind averaged over a 10-minute period (p. 41)

u_0, v_0 ambient wind components immediately prior to the wave (p. 45)

u_t, v_t velocity due to turbulence (Eq. 3.3)

u_2, w_2 the horizontal u_2 and vertical w_2 components of wind perturbation produced by the wave if it were propagating in the x direction in a shearless environment (Eq. 3.3)

V_{ro} Doppler velocity of the ambient air immediately before the wave (p. 81)

V_s storm speed (Eq. 3.5)

$\vec{V}_{KH}$ the vector velocity perturbation generated by Kelvin-Helmholtz waves (Eq. 3.3)

$|\vec{v}_p|$ the peak speed of the wave's perturbation velocity (p. 57)

v_{rp} Doppler velocity at the peak of the wave (Table 3.2, p. 83)

$v_r(r)$ Doppler (radial) velocity as a function of range r (p. 74)

$\vec{v}_{to}$ the speed, along the wavefront, of trapped thunderstorm outflow (Eq. 3.3)

$\vec{v}_2$ the two component (u_2, w_2) vector velocity perturbation of the wave (Eq. 3.3)

w vertical wind component (p. 13)

x horizontal coordinate axis perpendicular to wave front (p. 4)

$\tilde{x} \equiv x - ct$ (p. 32)

z vertical coordinate axis (p. 15)

z_0 height of stagnate air (p. 93)

α, β parameters in the equation of wave evolution (Eq. 2.24a)

γ angle between source path and a line tangent to wave front (p. 12)

$\Delta u_0, \Delta v_0$ change in u, v due to vertical transport of horizontal momentum, (p. 84)

δ vertical displacement produced by wave (p. 4)

δ_m maximum vertical displacement of air produced by the wave (p. 3)

$\epsilon = h_s / \lambda$ (p. 15)

θ_e equivalent potential temperature

θ_{vo} the virtual potential temperature of the ambient air (p. 17)

λ wave's half-width at half amplitude (p. 6)

μ angle that ray path makes with storm path

ξ scaled and translated x coordinate (p. 15)

ρ_0 density of incompressible fluid having an N equivalent to that of the atmosphere (p. 16)

τ scaled time coordinate (p. 15)

ϕ_c median azimuth of a sector over which Doppler velocities were averaged (p. 77)

ϕ_F azimuth of a line tangent to the front (Fig. 5a)

ϕ_s azimuth of storm track (p. 72)

$\phi(z)$ the z dependent part of the perturbation stream function

$\tilde{\psi}$ stream function in coordinate system translating with group velocity c (Eq. 2.35a)

$\psi \equiv \varepsilon\psi_1$ perturbation stream function for the variables u, w, etc. (p. 29).

$\psi_{max} = \varepsilon\psi_0$ peak amplitude of the perturbation stream function for variables u, w, etc. (p. 98)

ψ_0 peak amplitude of the perturbation stream function ψ_1 (Eq. 2.28a)

$\psi_1 \equiv f(\xi,\tau)\phi(z)$ first-order perturbation stream function for the perturbation variables u_1, w_1, etc. (p. 16)

$\psi_1^{(\ell)}$ perturbation stream function in the lower stratified layer (Eq. 2.29)

1.0. INTRODUCTION

Research at the National Center for Atmospheric Research and the University of Chicago has made the aviation community aware of wind shear hazards accompanying damaging downdrafts, currently called downbursts or, if of small diameter (i.e., 0.4 to 4 km), microbursts (Wilson et al., 1984; Fujita and Wakimoto 1983). However, these are not the only weather phenomena that can contain wind shear dangerous to an aircraft on its ascent from or descent into air terminals. Tornadoes and/or their larger diameter parent circulations, called mesocyclones, have caused crashes. A headwind change of 15 m s^{-1} (30 kt) or more could be expected in 1 km of flight through a mesocyclone (Doviak and Lee, 1985). On October 6, 1981, a Fokker F-28 commercial aircraft was observed exiting a thunderstorm cloud base at the location of a tornado, which sheared a wing from its fuselage (Wolliswinkel and Bierdrager, Private Communication).

Hazardous low-altitude shear has been associated with mountain lee waves, sea breezes, cold frontal passages, and more recently, with large-amplitude gravity wave disturbances. Gossard (1983) observed gravity waves that had wind speed changes of as much as 20 m s^{-1} (40 kt) in a distance of 5 km (3 mi).

In this report, we focus our attention on gravity waves that can have large amplitude yet short width (wavelength) and consequently strong shear, but which can travel hundreds of kilometers from the source with relatively little attenuation of possibly hazardous shear. These gravity waves, known as solitary waves, have been recently identified as a significant source of low-altitude shear (Christie and Muirhead, 1983a).

A solitary wave is a remarkably large-amplitude, single-crested, wave, first observed in the ocean where ships, sailing on an otherwise smooth sea,

are struck violently by a mountainous wave, which can send the vessels on their beam ends and sweep their decks from stem to stern. All this can occur in a matter of 5 minutes, after which the sea returns to its originally peaceful condition (Corliss, 1977).

It is not known whether these oceanic solitary waves are ever accompanied by atmospheric disturbances of similar form, but there is evidence that some of these ocean rogue waves occur with wind shifts. Furthermore, solitary ocean waves that strike the west coast of South America and the so-called Death waves on the west coast of Ireland are said to be precursors of storms (Corliss, 1977). A storm-generated atmospheric wave might induce an oceanic solitary wave, although subaqueous volcanic activity is more commonly thought to be responsible. The ease with which solitary waves can be generated in the laboratory (Maxworthy, 1980) suggests that large-amplitude nonlinear waves might be a commonly occurring feature in the lower atmosphere whenever suitable boundary layer conditions exist and sources are active.

The first definitive observations of the atmospheric solitary waves were made in 1976 with the Australian National University's Warramunga Infrasonic Array near Tenant Creek in northern Australia (Christie, et al., 1978). Atmospheric solitary waves are observed to occur either as single isolated waves of elevation or, more commonly, as groups of spatially separated amplitude-ordered sequences of solitary waves. In their early stage of formation, they are partially resolved waves associated with the actively evolving leading edge of a disintegrating longer wave disturbance (Christie and Muirhead, 1983a). The number of waves that evolve depends on the scale size of the initial disturbance--the larger the scale size, the larger the number of waves that can be generated (Whitham, 1974, Ch. 14, p. 595). Christie and Muirhead (1982) showed, through numerical simulations, how disturbances of long wavelength evolve into short, solitary ones.

Individual solitary waves are most commonly observed with amplitudes between 300 and 1000 m (900 to 3,000 ft) and effective horizontal lengths ranging from 0.5 to 6 km (0.3 to 5 mi). They usually propagate with speeds between 6 and 16 m s^{-1} (12 and 32 kt) but, on occasion, they have been observed to propagate with speeds exceeding 30 m s^{-1} (60 kt). Atmospheric solitary waves propagate along horizontal waveguides formed by layers of strongly positive potential temperature lapse rates. Solitary waves can grow in amplitude as their width decreases, thereby increasing shear, and their speed exceeds the speed of long-wavelength disturbances (e.g., a bore) by an amount proportional to wave amplitude. Thus, solitary waves have supercritical speeds.

Long-wavelength disturbances of small amplitude experience little dispersion and accompanying change in shape, resulting in long lifetimes. Short-wavelength disturbances of small amplitude, on the other hand, experience significant dispersion and thereby disintegrate quickly. However, long-wavelength disturbances of large amplitude break, whereas large-amplitude solitary waves of permanent form must have short-wavelength. Thus, the tendency of a large-amplitude disturbance to steepen and to break because of nonlinearity is offset by the dispersion, which tends to smooth the disturbance. This inverse relation between wave amplitude and its width (often the half-amplitude width is used to measure width) required for solitary waves ceases when the wave's displacement amplitude δ_m increases to a height about equal to the scale h_s of stratification, at which point recirculating air appears in the wave, causing the width to increase (Tung et al., 1982).

Although the evolutionary growth of solitary waves is observed in numerical model simulations, it is yet to be confirmed that such growth occurs in the atmosphere. Furthermore, it remains to be proved by observation that such

waves do evolve to large amplitude and short wavelengths that they constitute a hazard to aircraft. We show, later in this report (Chapter 4), results of observations suggesting that shear generated by solitary waves can have a significant effect on aircraft performance. Solitary waves that produce low-altitude wind shear require strong stability of the atmosphere close to the earth's surface and near-neutral stability above (Crook, 1986). Thus it is likely that many significant events may pass unobserved because such stable conditions usually occur in the late night or early morning hours when visual observations are sparse. However, the cold air outflow of a thunderstorm can also form a stable layer, and then the outflow of other thunderstorms passing over this layer can initiate waves (Doviak and Ge, 1984). Solitary waves might be one of the most insidious forms of wind shear because they usually occur, without warning, as unexpected clear air disturbances far from any storms. Yet they can harbor shears that might be destructive to aircraft and crew.

The solitary wave, by its essentially nonlinear nature, occupies a unique place in the development of a theory of wave propagation in fluids. The classical solitary wave was first observed by the Scottish scientist and engineer John Scott Russell (1840), on the free surface of shallow water in a canal of uniform depth h_s. Although he spent years trying to understand this solitary wave, his observation remained unexplained in his lifetime. Subsequently, Boussinesq (1871) and Rayleigh (1876) independently derived approximations for the speed of propagation c and the form $\delta(x)$ of the vertical displacement profile at the free surface. They found, to first order in the relative amplitude $\alpha = a/h_s \ll 1$, a solitary wave solution described by

$$\delta(x) = a \operatorname{sech}^2[\frac{(x-ct)}{w_\perp}], \qquad (1.1)$$

-4-

where a is the maximum vertical displacement, c the wave speed, and $w_\perp$ the wave width, measured perpendicular to the wave front, and is determined both by the wave amplitude and characteristics of the canal.

It was not until 1895 that two Dutch scientists (Korteweg and de Vries, 1895) derived their often-cited nonlinear differential equation, which precisely describes the characteristics of solitary waves propagating in one direction on the surface of a shallow canal, and which is the theoretical confirmation of Scott Russell's observations. Korteweg and de Vries showed that the time evolution of small, but finite amplitude, dispersive shallow water waves is described, in the first approximation, by the nonlinear partial differential equation (KdV equation)

$$\frac{\partial \delta}{\partial t} + c_0 \frac{\partial \delta}{\partial x} + \frac{3c_0}{2h} \delta \frac{\partial \delta}{\partial x} + \frac{c_0 h_s^2}{6} \frac{\partial^3 \delta}{\partial x^3} = 0, \tag{1.2}$$

where $c_0 = (gh_s)^{1/2}$ is the phase speed of a wave of infinitesimal amplitude (Whitham, 1974, Ch. 14, p. 463).

The observations of Scott Russell and the KdV equation were not widely appreciated until the significance of solitary waves as an important stable state of some nonlinear systems was realized in the mid-1960's. A crucial discovery in the development of the KdV theory was that solitary waves of different amplitudes, and hence of different speeds, pass through one another without any permanent loss of identity and suffer only phase shifts, even though nonlinear distortion is quite significant during the interaction. This phenomenon was discovered from numerical solutions of the KdV equation by Zabusky and Kruskal (1965), who coined the term "soliton" for any solitary wave having this property. The solitary wave has since appeared in many

-5-

fields of applied mathematics such as meteorology, fluid mechanics, electronic engineering, and laser physics.

Korteweg and de Vries also showed that Eq. (1.2) describes steady propagating, periodic waves that can be described mathematically by the square of a Jacobian elliptic cosine function $cn(x|m)$ for which they coined the term "cnoidal" waves. The modulus m of the elliptic function is equal to $(a\ell^2/h_s^3)^{1/2}$ where ℓ is a characteristic horizontal scale of the wave (Whitham, 1974, Ch. 14, p. 456). The length scale ℓ is a rough measure of wave width w and not necessarily of the distance (which could be vastly larger than ℓ) between wave crests. Thus the smaller is ℓ, the smaller is the width of the wave, but waves could be spaced far apart. In the limit as $m \to 0$, the elliptic cosine reduces to an ordinary cosine wave in which the wavelength (i.e., the separation between crests) $\lambda = 2\pi\ell\sqrt{3}$. When $m \to 1$, the wavelength λ becomes infinite and the elliptic cosine becomes the hyperbolic secant function (i.e., Eq. 1.1) in which wave width $w = (4h_s^3/3a)^{1/2}$ and wave speed $c = c_0(1+3a/2h_s)$. These latter relations for wave width and speed show, for waves of permanent form in shallow water, that the width of larger amplitude waves is shorter and wave speed is faster.

Since the 1950's, a number of investigations have been carried out on internal solitary waves in a fluid of finite depth. Keulegen (1953) and Long (1956) pioneered this field by investigating solitary waves in a system with two layers of different densities bounded by two rigid planes at the top and bottom surfaces. Peters and Stoker (1960) used a free surface at the top of the upper layer. The theory of internal solitary waves in fluids, whose density varies continuously with height, has been developed by Peters and Stoker (1960), Ter-Krikorov (1963), Long (1965), Benney (1966), Benjamin (1966) and several others. More recently, Egger (1983) gave a theoretical analysis of

internal atmospheric solitary waves in a two-layer fluid of finite depth, with a fixed upper boundary, by using the KdV-Burgers equation, in which the second derivative term is added to the KdV equation as a dissipation term. However, the finite depth of the fluid, implying the influence of both lower and upper boundaries, is an essential specification of theoretical models treated in all these works.

Levi-Civita (1925) proved the mathematical existence of internal, two-dimensional, periodic waves of finite amplitude and permanent form in water of infinite depth. Benjamin (1967) and Davis and Acrivos (1967a) independently presented the results of theoretical and experimental investigations of an entirely new class of internal solitary waves for the case where the fluid density varies only within a thin layer of thickness h, which is much smaller than the total depth and smaller than the effective horizontal length scale $\lambda(\varepsilon = h/\lambda \ll 1)$. *Since we shall not, in this work, deal with periodic waves,* we henceforth choose the symbol λ to represent the horizontal scale of the wave. Furthermore, in situations where there might be a train of n quasi-periodic solitary waves, λ_n characterizes the width of each wave and not the distance separating them. Benjamin (1967) found a steady-state, periodic solution for displacement δ of streamlines in a two-fluid system in which the upper fluid of constant density extends to infinity above a lower fluid of depth h, whose density varies with height above a horizontal rigid surface. Its limit form of infinite period is the solitary wave solution,

$$f(x) = \frac{a\lambda^2}{x^2 + \lambda^2},\qquad(1.3)$$

where a is the wave amplitude (or displacement) and λ the half-width at half-maximum amplitude.

Ono (1975) developed the theory for the time-dependent problem and de-
rived an evolution equation for unsteady-state deep-fluid solitary waves, us-
ing the nonlinear perturbation method. The evolution equation takes the fol-
lowing form:

$$\frac{\partial f}{\partial \tau} + \alpha f \frac{\partial f}{\partial \xi} - \beta \frac{\partial^2}{\partial \xi^2} H\{f\} = 0 \qquad (1.4)$$

where $H\{f\}$ denotes the Hilbert transform of f, and τ and ξ are scaled time and
space coordinates (Section 2.2). Equation (1.4) has been named the Benjamin-
Davis-Ono (BDO) equation, which is the deep-fluid counterpart of the KdV equa-
tion. An N-soliton solution of (1.4) has been found recently by Chen et al.,
(1979) and by Matsuno (1979).

The possible existence of atmospheric solitary waves was suggested by
several authors in the late 1940's and early 1950's. The first direct evi-
dence for atmospheric solitary waves appears to be the detailed description by
Abdullah (1955) of a large amplitude disturbance that propagated over Kansas
during the early daytime hours (0700 CST-1100 CST) of June 29, 1951. This
disturbance, which produced a surface pressure increase of 3.4 mb, took the
form of an elevated disturbance propagating on an inversion at a height of
about 2 km AGL. The disturbance wavelength was about 150 km and the wave was
observed to travel with approximately constant speed between 18 and 24 m s^{-1}
over a distance of nearly 800 km. There was a cold front extending over Colo-
rado, New Mexico, and Oklahoma. Abdullah concluded that the genesis of the
solitary wave was due to the interaction between the cold front and an inver-
sion layer. He also mentioned that there were some scattered showers in the
region where this wave passed, and it is reasonable to assume that these

showers resulted from the condensation caused by lifting the air over the wavecrest.

A survey of long-period digital records from an ultra-sensitive microbarograph array led to the initial discovery (Christie et al., 1978) of short wavelength internal solitary waves in the planetary boundary layer. The boundary layer solitary waves, commonly called "morning glories," observed recently in Australia have an effective wavelength of only a few kilometers (Clarke, 1972; Neal et al., 1977; Christie et al., 1979; Christie et al., 1981; Clarke et al., 1981). The morning glory is a wind squall or succession of wind squalls, frequently accompanied by one or more single-humped pressure disturbances, and is visually characterized by a long roll-cloud or series of such clouds. It often occurs in the early morning in the Gulf of Carpentaria area of northern Australia. The detailed studies of this type of phenomenon observed at Tennat Creek and Burketown in Northern Australia (Christie et al., 1979) have shown that these nonlinear wave disturbances occur as individual isolated solitons, and as amplitude-ordered solitary wave packets which propagate as predominantly interfacial disturbances along a boundary-layer inversion. Clarke et al. (1981) concluded that the morning glory is an undular bore propagating on the nocturnal and/or maritime inversion. Its source region appears to lie where a deeply penetrating sea-breeze front interacts with a developing nocturnal inversion.

Similar phenomena are also observed over inland areas of the North American continents (Haase and Smith, 1984; Doviak and Ge, 1984). However, instead of sea-breeze fronts, thunderstorms are more likely to be the source of these solitary waves. A detailed case study of a morning glory in the early morning of June 9, 1982, in central Oklahoma, has been given by Haase and Smith (1984). The authors interpreted this disturbance to be an internal undular

bore propagating within a low-altitude stable layer topped by a deeper upper layer of near neutral stability. Satellite imagery shows that the disturbance was associated with a cluster of rapidly growing intense thunderstorm cells several hundred kilometers to the north.

The mechanisms that lead to the production of solitary waves in the atmosphere are, generally speaking, not well understood at the present time. The observations suggest that the genesis of atmospheric solitary wave disturbances may be attributed to a wide variety of processes including middle-latitude cold frontal activity (Abdullah, 1955), the interaction of katabatic flow with the nocturnal inversion (Christie et al., 1978), deep penetrating sea-breeze fronts (Clarke et al., 1981; Christie and Muirhead, 1983a), and intense thunderstorm activity (Doviak and Ge, 1984).

2.0. THEORETICAL ANALYSIS

2.1. Fundamentals of Linear and Weakly Nonlinear Wave Theory

For almost any flow in an inviscid fluid we can start with the equation of motion,

$$\frac{\partial \vec{u}}{\partial t} + (\vec{u} \cdot \nabla)\vec{u} = -\frac{1}{\rho} \nabla p - \vec{g},$$ (2.1)

which is nonlinear. The solutions of (2.1) can describe waves that evolve and break due to the nonlinear term. For the purposes of analysis, we make approximations to simplify this basic equation.

At this point, we draw attention to two important approximations in the theory of wave propagation. The internal waves that we shall describe can be sorted into two types: (i) linear, small-amplitude, periodic waves and, (ii) weakly nonlinear long waves (long waves so-called because their horizontal wavelengths are much larger than the depth of the density inhomogeneity). For the first type (see Yih, 1960), the equations of motion are linearized by assuming that the wave amplitude is much smaller than the depth of the region in which density (or potential temperature for atmospheric waves) changes significantly and that products of perturbations are assumed negligible compared with linear terms. The subsequent development yields an infinite number of modes of linear dispersive traveling periodic waves. This approximation has been commonly used in fluid flow studies, which show that the solutions of Eq. (2.1) take the following form:

$$\vec{u} = \vec{A}e^{i(\vec{K} \cdot \vec{r} - \omega t)},$$ (2.2)

-11-

which is a good approximation for extremely small-amplitude waves. Neverthe-less, many waves observed in the oceans and the atmosphere have appreciable amplitude and, as a consequence, are nonsinusoidal. Because of wave disper-sion, it is not possible to find a solitary wave of permanent shape from the linearized equations of motion. On the other hand, the analysis of weakly nonlinear, long internal waves, yields solitary waves of permanent form (Ben-jamin, 1966).

Generally speaking, there are two important characteristics of a wave disturbance. One is nonlinearity, which steepens the wave's leading edge, in-creases shear, and, if sufficiently strong, causes the wave to break with rapid dissipation of wave energy. The other is dispersion, which smooths sharpness because the steepened wave comprises many Fourier components that propagate at different speeds. In this case, the wave cannot maintain its sharpness and large amplitude. Considered together, a balance of these two opposing tendencies may permit permanency of large-amplitude strong shear dis-turbances. Weakly nonlinear long waves are characterized by two small parame-ters: γ, which measures nonlinearity, is the ratio of wave amplitude a to the vertical scale h_s of the stratified layer; $\varepsilon = h_s/\lambda$ (the ratio of h_s to the wavelength scale λ) measures dispersion.

When the stratified layer occupies the entire depth of a shallow fluid, the appropriate evolution equation is the KdV equation (1.2) for which the balance between nonlinearity and dispersion requires that $\gamma = \varepsilon^2$ (see, for in-stance, Benney, 1966). When the fluid extends vertically to infinity and the stratified layer inside it is shallow, the appropriate evolution equation is the BDO equation for which the balance between nonlinearity and dispersion requires that ε be linearly related to γ (i.e., $\varepsilon = k\gamma$, where k is a constant of proportionality that is dependent upon the temperature profile and wave

mode number [Benjamin, 1967]. Koop and Butler (1981) presented the results of an experimental investigation characterizing solitary waves in terms of their shape and amplitude-wavelength scale relationship for shallow and deep-water configurations.

2.2. The Governing Equations

We consider two-dimensional motions of a dissipationless incompressible fluid that is stably stratified in the vertical direction. The governing equations in the stationary Cartesian frame (i.e., earth frame) are the Navier-Stokes equations:

$$\frac{\partial u}{\partial t} + u\frac{\partial u}{\partial x} + w\frac{\partial u}{\partial z} = -\frac{1}{\rho}\frac{\partial p}{\partial x}, \tag{2.3}$$

$$\frac{\partial w}{\partial t} + u\frac{\partial w}{\partial x} + w\frac{\partial w}{\partial z} = -\frac{1}{\rho}\frac{\partial p}{\partial z} - g \tag{2.4}$$

and the mass continuity equation which, for incompressible fluids, provides the two independent equations:

$$\frac{\partial \rho}{\partial t} + u\frac{\partial \rho}{\partial x} + w\frac{\partial \rho}{\partial z} = 0, \tag{2.5}$$

$$\frac{\partial u}{\partial x} + \frac{\partial w}{\partial z} = 0 \tag{2.6}$$

where u and w are, respectively, the horizontal and vertical velocities, p is the pressure, and ρ is the density.

In this section, we follow a derivation of the BDO equation by a singular perturbation method (Ono, 1975), but extend it to the case in which the fluid is in sheared flow. The ambient fluid considered here is separated into (i) a

stably stratified and sheared lower region ($0 < z < h$) for which a long-wave approximation can be made; and (ii) the homogeneous upper region ($z > h$) in which the wave motion is coupled to that in the lower region (Fig. 1). Although the inhomogeneous layer has a depth h, it is the vertical scale h_s of the inhomogeneity that is of crucial importance in determining wave properties. The vertical scale, usually less than h, is roughly the depth within which density changes sharply with height. In other words, it is the thickness of the layer within which the Brunt-Väisälä frequency is significantly higher than in the surrounding regions.
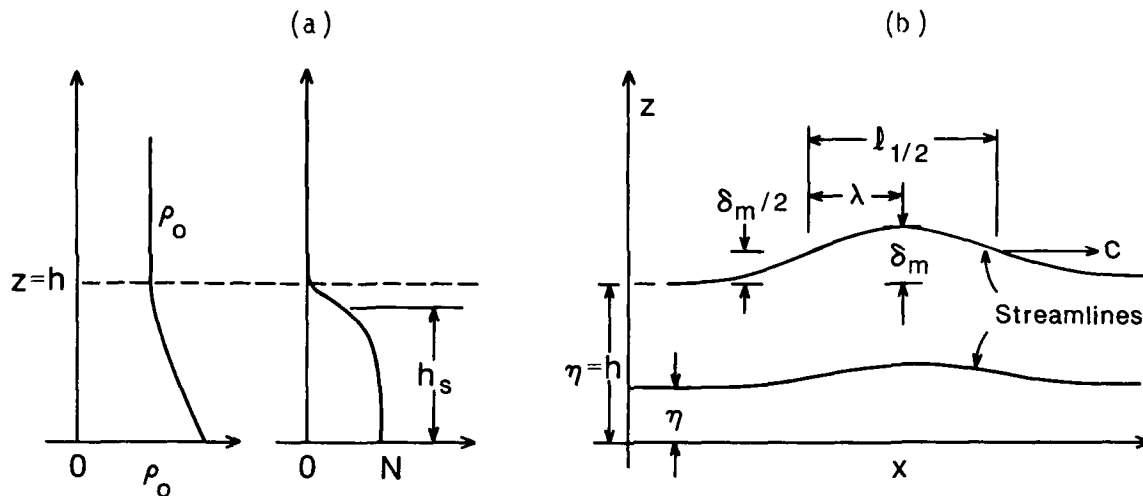
Figure 1a. Profiles of density ρ_0 and Brunt-Väisälä frequency N.
   1b. Wave characteristics (of a streamline) for a long wave (i.e., $\lambda \gg h$) of finite amplitude. η is the asymptotic height of the streamlines and δ_m is the maximum displacement.

2.2.1. Lower-layer equations

In order to reduce the equations of motion to a manageable form, we employ perturbation theory and seek modified equations applicable to waves whose length is long (as observed for the case under discussion herein) compared

with the vertical scale h_s of the stable layer. By following the procedure outlined by Dodd et al. (1982, Chapter 5), we use the dispersion relation $\omega = kc_0(1-\beta|k|)$, appropriate for long waves in fluids of infinite depth (Benjamin, 1967) to derive the coordinate transformations:

$$\xi = \epsilon(x - c_0 t), \qquad (2.7a)$$

$$\tau = \epsilon^2 t, \qquad (2.7b)$$

$$z = z, \qquad (2.7c)$$

where k is the wavenumber, c_0 is the phase speed of extremely long (i.e., $k \to 0$) infinitesimal waves in the stratified flow, and β is a constant. For a two fluid media having density ρ_1 in a lower layer of depth h_1 and ρ_2 in the infinitely deep upper layer, $\beta = \frac{1}{2}(\frac{\rho_2}{\rho_1}) h_1$. The purpose of transforming the scales of space and time is to extract, from the Navier-Stokes equations, simplified equations that are relevant to the description of the wave phenomena of interest (i.e., waves of characteristic length λ large compared with h_s). In order to have derivatives with respect to ξ, when scaled by h_s, to be of the same order of magnitude as the functions differentiated (Benjamin, 1967), we set $\epsilon = h_s/\lambda$ (a definitive specification of λ is given following Eq. (2.29)).

The expansion of the dependent variables, consistent with the above coordinate transformation, can be made in terms of the small parameter ϵ so that

$$u = u_0(z) + \sum_{n=1}^{\infty} \epsilon^n u_n(\xi, z, \tau) \qquad (2.8a)$$

$$w = \sum_{n=1}^{\infty} \epsilon^{n+1} w_n(\xi, z, \tau) \qquad (2.8b)$$

-15-

$$p = p_0(z) + \sum_{n=1}^{\infty} \epsilon^n p_n(\xi, z, \tau) \qquad (2.8c)$$

$$\rho = \rho_0(z) + \sum_{n=1}^{\infty} \epsilon^n \rho_n(\xi, z, \tau) \qquad (2.8d)$$

where $u_0(z)$ is the velocity of the sheared background flow, and $p_0(z)$ and $\rho_0(z)$ are the background pressure and density. In view of the continuity Eq. (2.6), the expansion of w starts from the second order of ϵ.

Expressing the governing equations in terms of the stretched coordinates ξ, z, τ, substituting Eq. (2.8) into them, retaining only the terms to lowest order in ϵ, and reducing the system of four equations to one in terms of w_1, the following equation can be obtained:

$$\frac{\partial}{\partial z} \left[\rho_0 (c_0 - u_0) \int \frac{\partial w_1}{\partial z} d\xi \right] + \frac{\partial}{\partial z} (\rho_0 \frac{du_0}{dz} \int w_1 d\xi) - \frac{g \frac{d\rho_0}{dz}}{(c_0 - u_0)} \int w_1 d\xi = 0. \qquad (2.9)$$

By assuming a product separation of the variable w_1 in the form

$$w_1(\xi, z, \tau) = - \frac{\partial f(\xi, \tau)}{\partial \xi} \phi(z), \qquad (2.10a)$$

we can express Eq. (2.9) solely in terms of z as

$$\frac{d}{dz} \left[\rho_0 (c_0 - u_0) \frac{d\phi}{dz} \right] + \frac{d}{dz} (\rho_0 \phi \frac{du_0}{dz}) - \frac{g\phi}{(c_0 - u_0)} \frac{d\rho_0}{dz} = 0. \qquad (2.10b)$$

The variable $\psi_1 \equiv f(\xi, \tau)\phi(z)$ defines a stream function from which all variables can be derived. That is,

$$w_1 = - \frac{\partial \psi_1}{\partial \xi} \qquad (2.11a)$$

$$u_1 = \frac{\partial \psi_1}{\partial z} \qquad (2.11b)$$

$$p_1 = - \rho_0 (u_0 - c_0) \frac{\partial \psi_1}{\partial z} + \rho_0 \psi_1 \frac{du_0}{dz} \qquad (2.11c)$$

$$\rho_1 = \frac{1}{(u_0 - c_0)} \psi_1 \frac{d\rho_0}{dz} . \qquad (2.11d)$$

By using the transformation $\tilde{\phi} = [\rho_0 / \rho_0(0)]^{1/2} \phi$ we can transform Eq. (2.10b) into

$$\tilde{\phi}'' + [\frac{1}{4} (\frac{\rho_0'}{\rho_0})^2 - \frac{\rho_0''}{2\rho_0} - \frac{u_0' \rho_0'}{\rho_0 (u_0 - c_0)} - \frac{u_0''}{(u_0 - c_0)} - \frac{g \rho_0'}{\rho_0 (u_0 - c_0)^2}] \tilde{\phi} = 0, \qquad (2.12a)$$

where the primes denote differentiation with respect to z. In this differential equation all parameters of the fluid appear in the single coefficient of the $\tilde{\phi}$ term, so then we can estimate the values of the various terms to show that some can be ignored compared with the others.

In order to make the comparison using atmospheric variables, we note that Eq. (2.1) applies to the atmosphere if the Coriolis force can be neglected. It can be shown that for the disturbance wavelengths (approximately a few kilometers) to be considered in this report, Coriolis force is negligible. We now relate the density ρ_0 of the incompressible fluid to the virtual potential temperature θ_{vo} of the moist atmosphere, which has the same Brunt-Väisälä frequency N. Then both media are dynamically similar. It can be shown that it is the parcel's virtual potential temperature, a conserved quantity for unsaturated moist adiabatic processes, that determines the stability of a moist atmosphere. This temperature is defined by

$$\theta_{vo} \equiv T_{vo} (\frac{1000}{p})^{0.286} (1 - 0.23m),$$

-17-

where m is the mixing ratio, p the total air pressure, and T_v the virtual temperature. The required relationship is then

$$\rho_0(z) = \frac{\rho_0(0)\theta_{vo}(0)}{\theta_{vo}(z)},$$

where ρ_0 is the density of the incompressible fluid having the equivalent stability of the atmosphere. Substituting for ρ_0 in terms of θ_{vo} into Eq. (2.12a), we obtain

$$\tilde{\phi}'' + \left[\frac{1}{2}\frac{\theta_{vo}''}{\theta_{vo}} - \frac{3}{4}\left(\frac{\theta_{vo}'}{\theta_{vo}}\right)^2 + \frac{\theta_{vo}' u_0'}{\theta_{vo}(u_0-c_0)} - \frac{u_0''}{(u_0-c_0)} + \frac{g\theta_{vo}'}{\theta_{vo}(u_0-c_0)^2}\right]\tilde{\phi} = 0. \quad (2.12b)$$

Now changes in θ_{vo} are small compared with $\theta_{vo}(0)$ so that $\tilde{\phi} \simeq \phi$ is a good approximation. For data that we shall consider, the first three terms in the brackets are negligible compared with the other two so that the above reduces to

$$\phi'' + \left[\frac{N^2}{(u_0-c_0)^2} - \frac{u_0''}{(u_0-c_0)}\right]\phi = 0 \quad (2.12c)$$

where $N^2 \equiv g\theta_{vo}'/\theta_{vo}$. The above simplifications are consistent with the Boussinesq approximation, and Eq. (2.12c) is the Taylor-Goldstein equation for a Boussinesq fluid (Tung et al., 1981). Using Eq. (2.11d) we derive the following expression for the perturbation θ_{v1} in virtual potential temperature:

$$\theta_{v1} = \frac{\psi_1}{(u_0-c_0)}\frac{d\theta_{vo}}{dz}. \quad (2.12d)$$

Equation (2.12c) is not solved easily, especially for vertical profiles of θ_{vo} and u_0 encountered in practice. Hence, numerical solutions are

suggested. However, in order to better understand the interrelationships between atmospheric variables and the wave parameters (e.g., amplitude, speed), we seek an analytical solution. But to have the mathematical development tractable we ignore wind. Thus

$$\phi'' + \frac{N^2 \phi}{c_o^2} = 0 \qquad (2.12e)$$

will be used to characterize the eigenfunction equation for solitary wave perturbations. However, as crude as the neglect of u_o'' in Eq. (2.12c) might appear to be, the work of Tung et al. (1981) suggests that the dominant mode solitary wave solution to the nonlinear evolution equation is, except for increases in wave speed, unchanged by the presence of shear. Thus, our neglect of the u_o'' term might not impose limitations as severe as first thought. Nevertheless, further work will be required to determine the effect of wind curvature on the solitary wave evolution.

We assume that the dimensions of the stream function ψ_1 are contained in $f(\xi,\tau)$, so that, without loss of generality, we can set $\phi(h) = 1$. This is just a normalization of ϕ and does not specify a boundary condition on w_1 at $z = h$. Now $z = 0$ is assumed to be the level of the ground where vertical velocity must be zero so that

$$\phi(0) = 0 \qquad (2.12f)$$

is a boundary condition. To obtain a completely specified solution to (2.12), we need to specify an additional boundary condition. This is obtained in Section 2.2.3 where we match vertical velocity and its derivative across the

interface that separates the inhomogeneous layer $0 < z < h$ and the layer $z > h$ where θ_{vo} is assumed constant.

Now proceeding to the next order of ϵ, and invoking the same approximations, it can be shown that

$$(\frac{w_2'}{\theta_{vo}})' - \frac{g}{c_0^2} (\frac{1}{\theta_{vo}})' w_2 = J(f,\phi) \qquad (2.13)$$

where

$$J(f,\phi) = -\frac{2}{c_0} (\frac{\phi'}{\theta_{vo}})' \frac{\partial f}{\partial \tau} - \frac{1}{c_0} \{3[\frac{(\phi')^2}{\theta_{vo}}]' - \frac{2\phi'\phi''}{\theta_{vo}} - 2(\frac{\phi\phi''}{\theta_{vo}})'\} f \frac{\partial f}{\partial \xi} .$$

We now show that w_2, the second-order solution, and its derivative w_2' at $z = h$, as well as $\phi(z)$, determine the ξ,τ dependence of $f(\xi,\tau)$. To derive the equation governing $f(\xi,\tau)$, we apply the following solvability condition (Ono, 1975):

$$\int_0^h [(w_2'/\theta_{vo})' - \frac{gw_2}{\theta_{vo}'c_0^2}]\phi \, dz = \int_0^h J(f,\phi)\phi \, dz \qquad (2.14)$$

which, when satisfied, avoids a resonant solution of Eq. (2.13). Alternately, the equation governing $f(\xi,\tau)$ can be obtained by applying the boundary conditions on w_2 to the integral solution of Eq. (2.13), a procedure followed by Benjamin (1967, p. 571). Now integrating both sides of Eq. (2.14) by parts, and applying the boundary conditions, $\phi = 0$, $w_2 = 0$ at the surface $z = 0$, Eq. (2.14) becomes

$$c_0 \theta_{vo}^{-1}(h)[w_2(\xi,h,\tau)\phi'(h) - w_2'(\xi,h,\tau)] =$$

$$[2\theta_{vo}^{-1}(h)\phi'(h)-2\int_0^h \theta_{vo}^{-1}(\phi')^2 dz]\,\frac{\partial f}{\partial \tau} + \{3\theta_{vo}^{-1}(n)[\phi'(h)]^2 \tag{2.15}$$

$$-3\int_0^h \theta_{vo}^{-1}(\phi')^3 dz - 2\theta_{vo}^{-1}(h)\phi''(h)\}\, f\frac{\partial f}{\partial \xi}\,.$$

Now it is obvious that if $w_2(\xi,h,\tau)$ and its first derivative at the interface, and $\phi'(z)$ are all known, Eq. (2.15) will give a governing equation for $f(\xi,\tau)$. The boundary conditions at $z = h$ are chosen so that the lower layer solution w and its derivative w' match, to $O(\varepsilon^3)$, the upper layer solution obtained in the next section. Because we shall assume for a first-order approximation that the region above $z = h$ is homogeneous, it is easily deduced from Eq. (2.12e) that $\phi''(h) = 0$ if θ_{vo}' is continuous at $z = h$, an assumption we will make henceforth. However, if θ_{vo}' is not continuous, it can still be shown that the $\phi''(h)$ term can be neglected if $N^2(h-) \ll N^2(0)$, where $N^2(h-)$ is the Brunt-Väisälä frequency just below the interface.

2.2.2. Upper-layer equations

Because the upper layer is of infinite thickness, there is no suitable scaling parameter ε with which to stretch the coordinate axis so that spatial scales in the vertical would be roughly equal to those in the horizontal. However, because the wave in the upper layer is coupled to the one in the lower layer, each must propagate in the ξ direction with the same phase velocity. Therefore we need to adopt the coordinate transformation:

$$X = x - c_0 t$$

$$\tau = \epsilon^2 t \qquad (2.16)$$

$$z = z.$$

Now the vertical velocity in the upper layer needs to be matched to that $w(\xi, z, \tau)$ in the lower layer. But we note that $w(\xi, z, \tau)$ asymptotically approaches $\epsilon^2 w_1$ as $\epsilon \rightarrow 0$ and because the continuity equation in the coordinate frame X, z, τ is

$$\frac{\partial u}{\partial X} + \frac{\partial w}{\partial z} = 0,$$

the horizontal velocity in the region $z > h$ must also asymptotically have an ϵ^2 dependence. These conditions lead us to expand the upper layer variables in the following form:

$$u = \sum_{n=1}^{\infty} \epsilon^{n+1} U_n(X, z, \tau), \qquad (2.17a)$$

$$w = \sum_{n=1}^{\infty} \epsilon^{n+1} W_n(X, z, \tau), \qquad (2.17b)$$

$$p = p_0(z) + \sum_{n=1}^{\infty} \epsilon^{n+1} P_n(X, z, \tau), \qquad (2.17c)$$

$$\rho = \rho_0(h) + \sum_{n=1}^{\infty} \epsilon^{n+1} R_n(X, z, \tau). \qquad (2.17d)$$

The density ρ_0 (or θ_{vo}^{-1}) is assumed to be constant throughout the upper layer.

Introduction of the expressions Eq. (2.17) into the equations of motion for the coordinate frame Eq. (2.16) and elimination of U_1, P_1, and R_1 at the leading order of ϵ (i.e., ϵ^2) yields

$$\frac{\partial^2 W_1}{\partial X^2} + \frac{\partial^2 W_1}{\partial z^2} = 0(\epsilon^2). \qquad (2.18a)$$

Because the next order approximation also leads to (2.18a), then W_1 in the upper layer satisfies Laplace's equation to $0(\epsilon^3)$.

2.2.3. Matching solutions at the interface

Now a solution of Eq. (2.18a) can be obtained given the following boundary conditions:

$$W_1(X,z,\tau) \to 0 \qquad\qquad \text{as } z \to \infty \qquad (2.18b)$$

and

$$\epsilon^2 W_1(X,z,\tau) = w(\xi,z,\tau) \qquad \text{at } z = h \qquad (2.18c)$$

where $w(\xi,h,\tau)$ is the lower layer solution, to $0(\epsilon^3)$, that matches the upper-layer one at $z = h$ and $\xi = \epsilon X$. The solution of this Dirichlet problem is (Appendix A)

$$W_1(X,z,t) = \frac{2}{\epsilon\pi} \int_{-\infty}^{+\infty} \frac{(X-X')\, f(X',\tau)\, (z-h)}{[(X-X')^2 + (z-h)^2]^2}\, dX'. \qquad (2.19)$$

Now in order to solve for w_2' needed in Eq. (2.15) we match the derivatives of w across the interface. The vertical gradient of W_1 is

$$\frac{\partial W_1}{\partial z} = \frac{2}{\varepsilon \pi} \int_{-\infty}^{+\infty} (X-X')f(X',\tau) \left\{ \frac{(X-X')^2 - 3(z-h)^2}{[(X-X')^2 + (z-h)^2]^2} \right\} dX' \qquad (2.20)$$

which becomes, at $z = h$,

$$\frac{\partial W_1(X,z,\tau)}{\partial z} \bigg|_h = \frac{2}{\varepsilon \pi} \int_{-\infty}^{\infty} \frac{f(X',\tau)}{(X-X')^3} dX'.$$

This can be written in the equivalent, alternate form:

$$\frac{\partial W_1(X,z,\tau)}{\partial z} \bigg|_h = \frac{\varepsilon}{\pi} \frac{\partial^2}{\partial \xi^2} \int_{-\infty}^{+\infty} \frac{f(\xi',\tau)}{(\xi - \xi')} d\xi'. \qquad (2.21)$$

By matching the vertical gradients of w across the interface, we obtain, to $O(\varepsilon^3)$,

$$\frac{\varepsilon^2 \partial W_1(\xi,z,\tau)}{\partial z} \bigg|_h + \frac{\varepsilon^3 \partial W_2(\xi,z,\tau)}{\partial z} \bigg|_h = \frac{\varepsilon^2 \partial W_1(X,z,\tau)}{\partial z} \bigg|_h. \qquad (2.22)$$

We need to match terms with the same order of ε, but noting that $\partial W_1/\partial z$ is proportional to ε, we obtain the following boundary conditions:

$$\frac{\partial W_1(\xi,z,\tau)}{\partial z} \bigg|_h = \frac{d\phi}{dz} \bigg|_h = 0 \qquad (2.23a)$$

and

$$\frac{\partial W_2(\xi,z,\tau)}{\partial z} \bigg|_h = \frac{1}{\pi} \frac{\partial^2}{\partial \xi^2} \int_{-\infty}^{+\infty} \frac{f(\xi',\tau)}{(\xi - \xi')} d\xi' = \frac{\partial^2}{\partial \xi^2} H\{f\}, \qquad (2.23b)$$

where

$$H\{f\} \equiv \frac{1}{\pi} P \int_{-\infty}^{+\infty} \frac{f(\xi',\tau)}{(\xi - \xi')} d\xi' \qquad (2.23c)$$

is the Hilbert transform of f, and the symbol P denotes the Cauchy Principal value of the integral taken along the real axis.

2.2.4. The equation of wave evolution

We finally obtain the desired equation governing $f(\xi, \tau)$ by using Eqs. (2.23) and (A.2a') in Eq. (2.15) to get

$$\frac{\partial f}{\partial \tau} + \alpha f \frac{\partial f}{\partial \xi} - \beta \frac{\partial^2}{\partial \xi^2} H\{f\} = 0 \qquad (2.24a)$$

where the coefficients α, β are functions of the stratified layer characteristics and are given by

$$\alpha = \frac{\frac{3}{2} \int_0^h \theta_{vo}^{-1} \phi'^3 dz}{\int_0^h \theta_{vo}^{-1} \phi'^2 dz} \qquad m^{-1}, \qquad (2.24b)$$

$$\beta = \frac{1}{2} \frac{c_o \theta_{vo}^{-1}(h)}{\int_0^h \theta_{vo}^{-1} \phi'^2 dz} \qquad m^2 s^{-1}. \qquad (2.24c)$$

The parameters c_o and ϕ are given by the solution of the eigenvalue problem Eq. (2.12e), and the operator H is defined by Eq. (2.23c). Because in atmospheric inversion layers changes in θ_{vo} are small relative to its mean value in that layer, the coefficients α, β are controlled principally by ϕ. However, ϕ strongly depends on the vertical profile of θ_{vo} through Eq. (2.12e).

In principal, Eq. (2.24), often referred to as the BDO equation in recognition of the work of Benjamin (1967), Davis and Acrivos (1967a), and Ono (1975), can be solved given any long-wave disturbance as an initial condition. Recently Tung et al. (1981) and Christie and Muirhead (1982) have provided

numerical solutions for the KdV equation and BDO equations given an initial wave distribution.

2.3. The Steady-State Solution for Propagating Solitary Waves

One of the most important contributions of Benjamin was to find a simple, closed-form, solution to Eq. (2.24) for waves of permanent form (i.e., $\frac{\partial f}{\partial \tau} = 0$). We now consider the steady-state solution of Eq. (2.24) resulting from the dynamical balance between the competing effects of nonlinearity, the second term, and dispersion, the third term. If we assume that $f(\xi, \tau)$ is a function of $\zeta = \xi - c_1 \tau$ alone, Eq. (2.24) reduces to

$$- c_1 \frac{df}{dr} + \alpha f \frac{df}{d\zeta} - \beta \frac{d^2}{d\zeta^2} H\{f\} = 0 \qquad (2.25)$$

where c_1 is the speed of the solitary wave in the ξ coordinate system, which itself moves toward positive x at a speed c_0 relative to the stationary (earth) coordinate frame x,z,t. Because the ξ axis is stretched by ϵ relative to the x axis, the speed of the wave in the stationary frame is $(c_0 + \epsilon c_1)$, which is easily deduced by the following steps:

$$\zeta = \xi - c_1 \tau = \epsilon(x - c_0 t) - \epsilon^2 c_1 t = \epsilon[x - (c_0 + \epsilon c_1)t] \equiv \epsilon \tilde{x} \qquad (2.26a)$$

where $\tilde{x}$ is the unstretched x coordinate, which moves at the wave speed

$$c = c_0 + \epsilon c_1 \qquad (2.26b)$$

toward positive x.

Ono (1975) has shown that Eq. (2.25) is equivalent to the stationary wave equation derived by Benjamin (1967) and Davis and Acrivos (1967a). A solution of Eq. (2.25) is

$$f(\zeta) = \frac{\psi_0 \lambda_s^2}{\zeta^2 + \lambda_s^2}, \qquad\qquad (0 < z < h). \qquad (2.27)$$

For Eq. (2.27) to be a solution of Eq. (2.25), the relations

$$\psi_0 = \frac{4c_1}{\alpha} \qquad\qquad (2.28a)$$

and

$$\lambda_s = \frac{4\beta}{\psi_0 \alpha} \qquad\qquad (2.28b)$$

must be satisifed. That Eq. (2.27) is a solution can be confirmed by substituting it and Eq. (2.28) into Eq. (2.25) and using the fact that

$$H\left[(\zeta^2 + \lambda_s^2)^{-1}\right] = \lambda_s^{-1} \zeta (\zeta^2 + \lambda_s^2)^{-1}.$$

Equation (2.27) is the algebraic solution first discovered by Benjamin (1967) for internal solitary waves in infinitely deep fluids. The stream function amplitude at $z = h$, $\zeta = 0$ is ψ_0, and λ_s is the wavelength in the stretched coordinate ζ. The width at half amplitude is then $2\lambda_s$ and the stream function $\psi_1^{(\ell)}$ in the lower layer is

$$\psi_1^{(\ell)} = \frac{\psi_0 \lambda_s^2}{\zeta^2 + \lambda_s^2} \phi(z), \qquad\qquad 0 < z < h. \qquad (2.29)$$

Because the half-amplitude width $\ell_{1/2} = 2\lambda$ in the unstretched coordinate frame x,z,t is equal to $2\lambda_s/\epsilon$, and because $\epsilon = h_s/\lambda$, we find that $\lambda_s = h_s$. Because

h_s, α, and β are constants for a specified virtual potential temperature profile, Eq. (2.28) clearly shows that the wave's amplitude and speed, as well as width λ_s, are fixed by the θ_{vo} profile. However, we show in Section 2.3.2 that the wave parameters in the unstretched coordinate frame are not fixed by the θ_{vo} profile but only require, for wave permanency, that amplitude be an inverse function of wavelength. From Eqs. (2.26) and (2.28), we note that the speed of the wave in the fluid is ϵc_1 faster than the speed c_0 for extremely long waves of infinitesimal amplitude. Because waves of the longest wavelengths are the fastest of vanishingly small amplitude waves, and because the solitary wave speed is faster than this, the solitary wave is said to propagate at supercritical speeds.

In terms of the unstretched coordinate axis $\widetilde{x}$,

$$f(\widetilde{x}) = \frac{\psi_0 \lambda^2}{\widetilde{x}^2 + \lambda^2} , \qquad\qquad 0 < z < h. \qquad (2.30)$$

In this coordinate frame we notice that the wave's half-amplitude width $\ell_{1/2}$ is no longer fixed at a value equal to $2h_s$, but is a variable. The steady-state solution for the vertical velocity is obtained using (A.4) of Appendix A:

$$W_1(\widetilde{x},z) = - \frac{1}{\epsilon\pi} \int_0^\infty k e^{-k(z-h)} [\int_{-\infty}^{+\infty} \frac{\psi_0 \lambda^2}{(\widetilde{x}^2+\lambda^2)} \sin k(x'-\widetilde{x})dx']dk; \quad h < z$$

in which $f(\widetilde{x})$ has been substituted for $f(X,\tau)$. The integrations can be executed using the integral formulas found in Gradshteyn and Ryzhik (1965, pp. 407 and 490) to yield

$$W_1(\widetilde{x},z) = \frac{2\psi_0 \lambda}{\epsilon} \frac{(z-h+\lambda)\widetilde{x}}{[\widetilde{x}^2 + (z-h+\lambda)^2]^2} , \qquad\qquad z > h. \qquad (2.31)$$

-29-

Now the stream function in the upper layer is $\psi_1^{(u)} \equiv -\int W_1 d\tilde{x}$, so

$$\psi_1^{(u)} = \frac{\psi_0 \lambda (z-h+\lambda)}{\varepsilon[\tilde{x}^2 + (z-h+\lambda)^2]} , \qquad z > h. \qquad (2.32)$$

That the vertical velocity in the upper layer matches that in the lower layer at $z = h$ is easily demonstrated by substituting Eq. (2.31) into Eq. (2.17b) and using Eq. (2.29) in Eqs. (2.11) and (2.8).

By using Eqs. (2.8) and (2.12d), the dependent variables u, w, p, and ρ can be expressed, to first order in ε, in terms of the stationary frame co-ordinates x, z, t, and a stream function $\psi \equiv \varepsilon \psi_1$ as

$$u(x,z,t) = u_0(z) + \frac{\partial \psi}{\partial z} \qquad (2.33a)$$

$$w(x,z,t) = - \frac{\partial \psi}{\partial x} \qquad (2.33b)$$

$$p(x,z,t) = p_0(z) + c_0 \rho_0 \frac{\partial \psi}{\partial z} \qquad (2.33c)$$

$$\theta_v(x,z,t) = \theta_{vo}(z) - \frac{\psi}{c_0} \frac{d\theta_{vo}}{dz} \qquad (2.33d)$$

where

$$\psi = \psi^{(\ell)} = \frac{\varepsilon \psi_0 \lambda^2 \phi(z)}{(x-ct)^2 + \lambda^2}, \qquad z < h \qquad (2.33e)$$

is the stream function in the stationary frame (i.e., earth coordinates). The wave speed c can be expressed in terms of the stratification parameter β by eliminating ψ_0 between Eqs. (2.28a) and (2.28b) and noting that $h_s = \lambda_s$ so that when c_1 is substituted into Eq. (2.26b) we obtain

$$c = c_0 + \beta/\lambda, \qquad\qquad (2.33f)$$

the speed of the wave relative to this frame. The stream function ψ_1 is defined in Section 2.2.1 in terms of the first-order variables, u_1, w_1, etc., which are related to the first-order components u, w, etc., of Eq. (2.8) by the multiplicative factors ε, ε^2, etc. Therefore we had to define the stream function $\psi = \varepsilon\psi_1$ in order to derive correctly scaled u, w, etc., from Eqs. (2.33a-d). Thus in the unstretched coordinate frame, the stream function amplitude ψ_{max} is equal to $\varepsilon\psi_0$. Substituting this and $\lambda_s = \varepsilon\lambda$ into Eq. (2.28b) gives the expression

$$\lambda = \frac{4\beta}{\alpha\psi_{max}}, \qquad\qquad (2.33g)$$

which clearly shows, for permanent waves, the inverse relation between wavelength and amplitude. Thus, shorter wavelength waves can have larger amplitudes, and consequently more intense shear, without the wave's breaking and dissipating.

In the upper layer $z > h$ the stream function is

$$\psi = \psi^{(u)} = \frac{\varepsilon\psi_0\lambda(z-h+\lambda)}{[(x-ct)^2 + (z-h+\lambda)^2]}, \qquad z > h. \qquad (2.34)$$

Likewise, in the upper region, the first-order terms u, etc., are the products of ε^2 and the first-order variable u_1, etc. Therefore, the stream function $\psi = \varepsilon^2\psi_1$ gives the correct u, etc., when Eqs. (2.33a-d) are applied. It is worthwhile to mention that although these first-order solutions have ψ and $\partial\psi/\partial x$ continuous across the interface, $\partial\psi/\partial z$ is discontinuous there and hence $\partial w/\partial z$ and u are also discontinuous at $z = h$.

Examination of Eqs. (2.33e) and (2.34) shows that, for the dominant mode in which $\phi(z)$ is a monotonically increasing function in the interval $o < z < h$, the stream function is always positive and has a peak amplitude $\epsilon\psi_0$ at $x = 0$, $z = h$. Although the wave's half-amplitude width is a constant equal to 2λ in the region $z < h$, it is a monotonically increasing function equal to $2(z-h+\lambda)$ for $z > h$ where the wave amplitude decreases as z increases. Furthermore, parcels of air are lifted by the wave as it passes and are displaced a fixed horizontal distance. This can be deduced from the finite positive value of the time integral of u. That is, after the wave passes, the parcels of air do not return to their original positions, but are permanently displaced to the right for a wave propagating to the right. However, they do return to their original height.

The horizontal velocity of the wave is maximum at the earth's surface (if friction is ignored) and consequently this is where the parcel displacement and shear would be largest. However, frictional effects of the terrain will diminish the intensity of shear near the ground and lessen parcel displacement. Nevertheless, the wave passage can enhance pre-existing shear which together may be sufficient to cause dynamic instabilities and the formation of Kelvin-Holmholtz waves and turbulence, as observations discussed in Section 3.2 show.

2.3.1. Streamlines and wave properties--comparison with Benjamin's solution

Streamlines give a better visual impression of the flow than of the stream function so we now discuss some of the properties of solitary wave streamlines. To present streamlines, we use a coordinate frame that

translates at the speed c of the wave so that the stream function in this frame is independent of time. In this case the stream functions are

$$\widetilde{\psi}(\widetilde{x},z) = \frac{\varepsilon\psi_0\lambda^2\phi(z)}{(\widetilde{x})^2 + \lambda^2} - cz, \qquad\qquad z < h \qquad (2.35a)$$

and

$$\widetilde{\psi}(\widetilde{x},z) = \frac{\varepsilon\psi_0\lambda(z-h+\lambda)}{[(\widetilde{x})^2 + (z-h+\lambda)^2]} - cz, \qquad\qquad z > h. \qquad (2.35b)$$

where $\widetilde{x} \equiv x-ct$. As $\widetilde{x} \to \infty$, the stream functions have the asymptotic value $-cz$. Thus, we are led to assume some value for z, say n, which a streamline asymptotically approaches, and then solve $\widetilde{\psi}(\widetilde{x},z) = \widetilde{\psi}(\infty,z) = -cn$ for z to determine streamline height, given $\widetilde{x}$. Therefore a streamline is the solution of

$$c(z-n) - \frac{\varepsilon\psi_0\lambda^2\phi(z)}{(\widetilde{x})^2 + \lambda^2} = 0, \qquad\qquad o < z < h \qquad (2.36a)$$

and

$$c(z-n) - \frac{\varepsilon\psi_0\lambda(z-h+\lambda)}{(\widetilde{x})^2 + (z-h+\lambda)^2} = 0, \qquad\qquad h < z. \qquad (2.36b)$$

The displacement $\delta \equiv (z-n)$ of a streamline from its asymptotic height n is

$$\delta = \frac{\widetilde{\psi}(\widetilde{x},z)}{c} + z, \qquad\qquad (2.37)$$

which gives displacements as a function of $\widetilde{x}$, z. From the above equations, it is apparent that the maximum displacement of a streamline occurs at $\widetilde{x} = 0$, where

$$\delta(0,z) = \frac{\varepsilon \psi_0 \phi(z)}{c}, \qquad\qquad o < z < h \qquad (2.38a)$$

$$\delta(0,z) = \frac{\varepsilon \psi_0 \lambda}{c(z-h+\lambda)}, \qquad\qquad h < z. \qquad (2.38b)$$

For the dominant mode, $\phi(z)$ increases to its value of unity at $z = h$. Thus the peak displacement δ_m, or amplitude of the wave, is

$$\delta_m = \frac{\varepsilon \psi_0}{c} = \frac{\psi_{max}}{c}, \qquad\qquad (2.39a)$$

which occurs along the streamline remaining entirely in the lower layer but which is tangent to the level $z = h$. That is, the peak displacement is at the interface. Equation (2.38b) shows that the rate of decrease of $\delta(0,z)$ vs. z (for $z > h$) has an inverse dependence on λ; the longer is λ, the slower is the decrease of $\delta(0,z)$ with height.

To compare our results with those of Benjamin (1967), whose solutions are in terms of streamline displacement, it is most direct to solve Eq. (2.37). But Eq. (2.37) does not give the shift as a function $\tilde{x}$ along a single streamline having the asymptotic height η. In order to obtain that result, we need to substitute $z = \eta + \delta$ into Eq. (2.37) and then solve for δ. The functional form of the solutions in the upper layer are independent of the lower layer stratification and hence it would be convenient to compare solutions there. Therefore we need to solve

$$c\delta - \frac{\varepsilon \psi_0 \lambda(\delta+s)}{(\tilde{x})^2 + (\delta+s)^2} = 0 \qquad\qquad (2.39b)$$

for δ, where $s \equiv \eta - h + \lambda$ defines a streamline. However, the solution of this equation is not easy, so we expand (2.39b) to second order in δ, since it is small compared with s, and solve for δ to obtain

$$\delta \simeq \frac{\lambda s \, \delta_m}{(\tilde{x})^2 + s^2} , \tag{2.39c}$$

an approximate solution that neglects a $\delta_m \lambda$ term because it is small compared with $s^2 > \lambda^2$. Benjamin's solution (1967, Eq. 3.83) is

$$\delta = \frac{a s^2}{(\tilde{x})^2 + s^2} , \tag{2.39d}$$

where a is the peak displacement of the streamline having the asymptote $\eta = h$. But at $\eta = h$, $\lambda = s$ and a comparison of Eqs. (2.39c and d) shows that $a \equiv \delta_m$. Although the difference between Eqs. (2.39c) and (2.39d) is slight for streamlines having asymptotes $\eta \simeq h$, the solutions differ markedly when $\eta - h \gtrsim \lambda$. Benjamin's solution shows that the peak displacement of the fluid in the upper region is independent of height, whereas Eq. (2.39c) shows that peak displacement decreases with height. More specifically, since Benjamin's solution does not satisfy his stipulated boundary condition (i.e., $\delta \to 0$ as $z \to \infty$) we must assume his solution is in error.

2.3.2. Properties of the dominant mode solitary wave

Because the change in θ_{vo} across any inhomogeneous atmospheric layer is usually small compared with the layer mean $\overline{\theta}_{vo}$, Eqs. (2.24b-c) can be approximated by

$$\alpha \simeq \frac{3 \int_o^h (\phi')^3 dz}{2 \int_o^h (\phi')^2 dz} \tag{2.40a}$$

and

$$\beta = \frac{c_o}{2 \int_o^h (\phi')^2 dz} . \tag{2.40b}$$

By substituting $\epsilon\lambda = \lambda_s$ and Eq. (2.39a) for ψ_0 into Eq. (2.28b), and using Eq. (2.33f) to eliminate c, we obtain

$$\delta_m = \frac{4\beta}{\alpha(c_0\lambda+\beta)} , \qquad (2.40c)$$

an equation that specifies the relation between wave displacement amplitude δ_m and wavelength λ in order for the wave to have permanent form.

We shall be principally concerned with the dominant mode eigenfunction $\phi(z)$ since that is most frequently observed. In this case $\phi(z)$ monotonically increases in the interval $0 < z < h$ so we can estimate α and β by assuming that ϕ is approximated by the lowest order power series

$$\phi \simeq 2\left(\frac{z}{h}\right) - \left(\frac{z}{h}\right)^2 , \qquad (2.41a)$$

which satisfies the boundary conditions, $\phi = 0$ at $z = 0$, $\phi'(h) = 0$ at $z = h$. Substituting ϕ' into Eq. (2.40) and integrating, we find that

$$\alpha \simeq \frac{9}{4h} , \qquad (2.41b)$$

and

$$\beta \simeq \frac{3c_0 h}{8} . \qquad (2.41c)$$

By substituting these values into Eq. (2.40c), we find that

$$\frac{\delta_m}{h} \simeq \frac{2h}{3\lambda(1+3h/8\lambda)} . \qquad (2.42a)$$

The first-order terms of the expansions in Eq. (2.8) give satisfying approximate solutions only if $\epsilon \simeq h/\lambda$ is much less than unity. Thus,

$$\frac{\delta_m}{h} \simeq \frac{2}{3} \frac{h}{\lambda} \qquad (2.42b)$$

must have the same order of magnitude as h/λ. In other words, not only must the displacement amplitude of a wave of permanent form have an inverse relation to λ, but also the wave must be weakly nonlinear in order for the solution given by Eq. (2.27) to be valid. However, this does not imply that steady-state solitary waves having displacements comparable with h cannot exist. Tung et al. (1982) showed that large-amplitude internal waves can have a permanent form different than that given by Eq. (2.27) and yet satisfy Eq. (2.25). Thus the condition given by Eq. (2.42b), for a solitary wave to be permanent, is valid only for weakly nonlinear waves and solutions of the form given by Eq. (2.27).

In the more general case of a stratified layer thickness h, much larger than the scale h_s of stratification, α and β will not be a function of h but will depend on h_s. In this case, again for $\phi(z)$ monotonic in the stratified layer, $\phi'(z)$ is roughly h_s^{-1} and so from Eqs. (2.40a) and (2.40b)

$$\alpha \simeq 3/2h_s \qquad (2.42c)$$

$$\beta \simeq c_o h_s/2 \qquad (2.42d)$$

and, when these values are substituted into Eq. (2.40c), the condition on δ_m becomes

$$\lambda \delta_m / h_s^2 \simeq \frac{4}{3}(1 + \frac{h_s}{2\lambda})^{-1} \simeq \text{order of unity}, \qquad (2.42e)$$

since $h_s/\lambda \ll 1$. Thus in the general case, the solution given by Eq. (2.27) is valid only if wave amplitude δ_m is weak (i.e., $\delta_m/\lambda \ll 1$). Thus the theory based on this solution is said to be weakly nonlinear.

Equation (2.42e) applies to the case of internal waves in infinitely deep fluids having a vertical scale h_s of stratification, and is a result first uncovered by Benjamin (1967) who contrasted it with the relation

$$\frac{\delta_{ms}\lambda^2}{h_0^3} \simeq \text{order of unity},\qquad (2.43)$$

appropriate for solitary waves on shallow fluids, where δ_{ms} is the displacement amplitude of the surface wave and h_0 is the depth of the fluid. Thus in the case in which the depth of the shallow fluid is equal to the scale of stratification in the infinitely deep fluid, the latter's solitary waves have much larger amplitude if $h_0/\lambda = h_s/\lambda \ll 1$.

At this juncture, we consider a simple but practical example, so that we can better understand the properties of the steady-state solitary wave. Let us assume that the Brunt-Väisälä frequency is a constant in the region $z \leqslant h$ and zero above (i.e., θ_{vo} = constant for $z > h$). Solution of Eq. (2.12) gives

$$\phi(z) = \sin\left[\frac{(\overline{N^2})^{1/2} z}{c_0}\right].\qquad (2.44)$$

We use the bar above N^2 to signify a lower-layer average of N^2, anticipating that we will accept the eigenfunction $\phi(z)$ as the first approximation to the solution for the case in which N^2 is a function of z. Substituting this function into Eq. (2.40) gives

$$\alpha = \frac{2}{h} \; ; \qquad \beta = \frac{4hc_0}{\pi^2}\qquad (2.45a)$$

where

$$c_0 = \frac{2h}{\pi} (\overline{N^2})^{1/2} \qquad\qquad (2.45b)$$

is the eigenvalue that satisfies the boundary condition $\phi'(h) = 1$ and is the linear wave velocity (i.e., the speed of a wave of infinitesimally small amplitude). Thus the wave speed is linearly dependent on the Brunt-Väisälä frequency of the layer. It is of interest to point out that the wave velocity (computed from Eq. 2.45b) for infinitely deep media, but in which the layer of stratification is small compared with λ, is twice that given by Tung et al. (1981) for shallow media (total depth h small compared with λ) having the same uniform stratification and boundary conditions except that $w = 0$ at $z = h$ for the shallow fluid whereas $w = 0$ at $z = \infty$ for the deep fluid. Thus the nearness of the upper boundary layer can exert an enormous influence on the wave speed (and probably the waveform) and thus its location may be of crucial importance in numerical models in which the upper boundary is usually placed, for practical reasons, at a finite distance above the layer of stratification. Although we have indicated that wave speed in an infinitely deep medium is twice that for a shallow one, Maslowe and Redekopp (1980) have solved a similar pair of problems for sheared flow, and their solution suggests that wave speeds are identical. They specifically note "that the eigenvalue relation is the same for both depth limits is unexpected." This difference appears to be due to the fact that they have matched pressure across the interface $z = h$, and this condition results in $\phi'(h) \neq 0$, whereas in the BDO solutions $\phi'(h) = 0$. Apparently Maslowe and Redekopp use the condition of pressure continuity because they have assumed sheared flow. However, their results suggest that wave speeds for shearless flow are the same for infinitely deep and shallow media (see their Fig. 8). Further investigation is required to determine the root of this apparent discrepancy.

For a vertical profile of θ_{vo}, linear over h,

$$N^2 = \frac{g \Delta\theta_{vo}}{\overline{\theta}_{vo} h} .$$

(2.46a)

For this case we can estimate c_0 using the relation

$$c_0 \simeq \frac{2}{\pi} \left(\frac{g \Delta\theta_{vo} h}{\overline{\theta}_{vo}} \right)^{1/2}$$

(2.46b)

where $\overline{\theta}_{vo}$ is the layer mean. Substituting β from Eq. (2.45a) into Eq. (2.40c), we find that

$$\frac{\delta_m \lambda}{h^2} = \frac{8}{\pi^2} \left(1 + \frac{4}{\pi^2} \frac{h}{\lambda} \right)^{-1} \simeq \text{order of unity},$$

(2.47)

a result similar to the one (i.e., Eq. 2.42b) roughly estimated.

We can express wave speed in terms of δ_m by applying Eqs. (2.28a), (2.45a), and (2.39a) to Eq. (2.23f) to obtain

$$c = 1 - \frac{c_0}{\left(1 - \frac{\delta_m}{2h} \right)} \simeq c_0 \left(1 + \frac{\delta_m}{2h} \right).$$

(2.48)

This agrees with the wavespeed Benjamin (1967) computed for waves propagating in a layer having an exponential decrease of ρ_0, if the argument of the exponential function is small so that $h_s \simeq h$. Equation (2.48) shows that the phase speed increment, added to the phase speed c_0 for extremely long waves of infinitesimal amplitude, is proportional to wave amplitude. This property of nonlinear waves is important to our interpretation of radar data presented in Section 3.0.

3.0. THEORETICAL SOLUTIONS COMPARED WITH OBSERVATIONS

Doviak and Ge (1984) presented evidence that a thin line of reflectivity, commonly associated with gust fronts, was in fact a solitary wave generated by the interaction of thunderstorm outflows. However, they did not make quantitative comparisons of data with theory. Although they emphasized analysis of data collected using a tall (444-m) tower, the Doppler velocity field was shown to be consistent with winds measured by anemometers on the tower. In this section we examine in greater detail the Doppler radar's data fields to determine the wave characteristics that are accessible because of the time and space continuous observations made with Doppler radar. Furthermore the radar data fields of reflectivity and velocity are used to determine the relation between wave amplitude and speed of propagation for comparisons with the weakly nonlinear theory (Section 3.5) as well as (Section 3.6) the theoretical results given by Tung et al. (1982) for strongly nonlinear waves.

We also use the Doppler data fields to examine the vertical profiles of reflectivity and wind of the ambient air in which the solitary wave propagates. We show that refractive index irregularities can account for measured reflectivity in the upper layers but the unusually large reflectivity in the lower layers is probably caused by the presence of insects.

3.1. The Ambient Environment

The virtual potential temperature profile in advance of the wave is calculated from dry-bulb and dew-point temperature data from rawinsondes for altitudes above 444 m by interpolating data at the 1800 CST 5/11/80 and 0600 CST 5/12/80 sounding times to the 2300 CST time of wave passage at the tower. The virtual potential temperatures computed from tower data show the presence of an intense surface-based inversion layer having a thickness of at

-40-

least several hundred meters. The solid line in this figure is the subjectively fitted function,

$$\theta_{vo} = 308.4 - 14e^{-z/350}, \qquad\qquad 0 < z < 1,140 \text{ m} \qquad (3.1a)$$

$$\theta_{vo} = 306.3 + 1.5 \times 10^{-3} z, \qquad\qquad 1,140 \text{ m} < z. \qquad (3.1b)$$

Although $(\theta_{vo})'$ is continuous across the interface, $z = h$, the assumption made in setting the $\phi''(h)$ term to zero in Eq. (2.15), is open to question because we have a non-zero value for $\theta_{vo}'(z)$ for $z > h$. However, it can be shown that the $\phi''(h)$ term in Eq. (2.15) is small compared with the preceding term in that equation. The dashed curve is a hyperbolic tangent function fitted to the data and is discussed in Section 3.6.

Figures 2a and 2b show the vertical profiles of the northwest (u_a) and southwest (v_a) averaged wind components, before wave arrival, which are respectively perpendicular to and along the wave front at the time (2305 to 2315) the wave passed the tower. The estimates from anemometers on the tower (36 km from the radar at azimuth 356°) are 10-min averages of the data spaced 10 s apart about 2245, the time radar data were also used to compute u and v. The ambient winds measured with radar are obtained from estimated Doppler velocities for an assumed horizontally uniform wind model, least-squares-fitted to the Doppler velocities measured over an azimuthal sector from 330° to 30° at ranges near 30 or 40 km where data were free from ground clutter, and range-aliased overlying echoes (Doviak and Zrnic', 1984). However, the upper four data points are taken from Doviak and Ge (1984, Fig. 5). In that study the wind at each height was assumed to be uniform over an approximately 50° azimuthal sector, roughly centered to the north. Approximately five Doppler velocity data at each azimuth in a 1 km range interval were averaged to
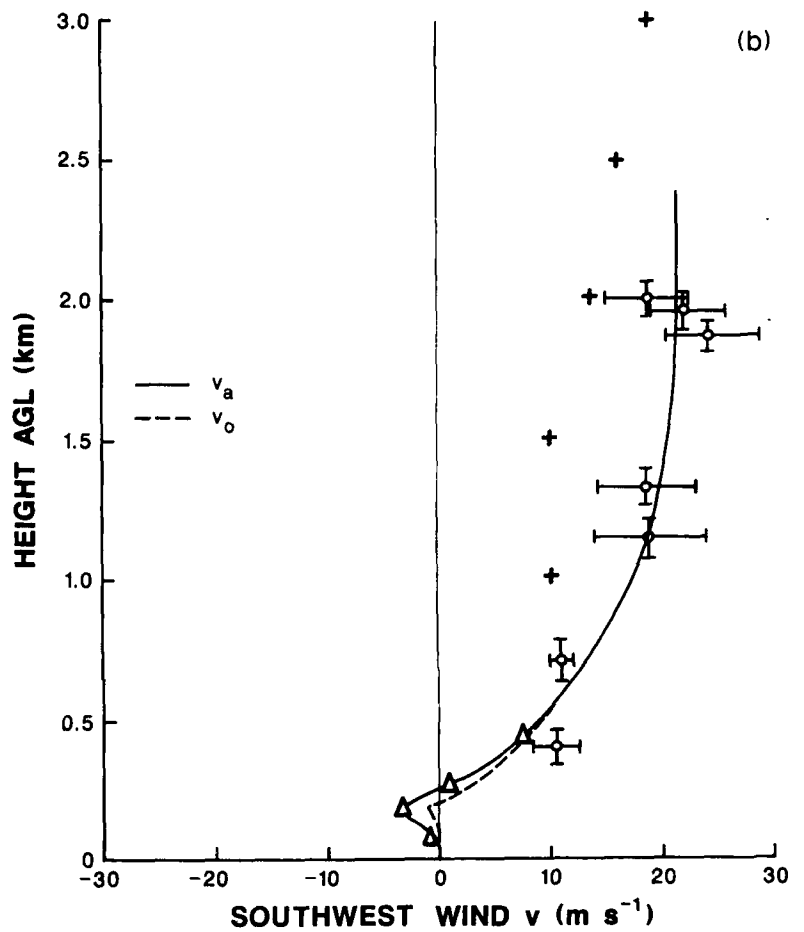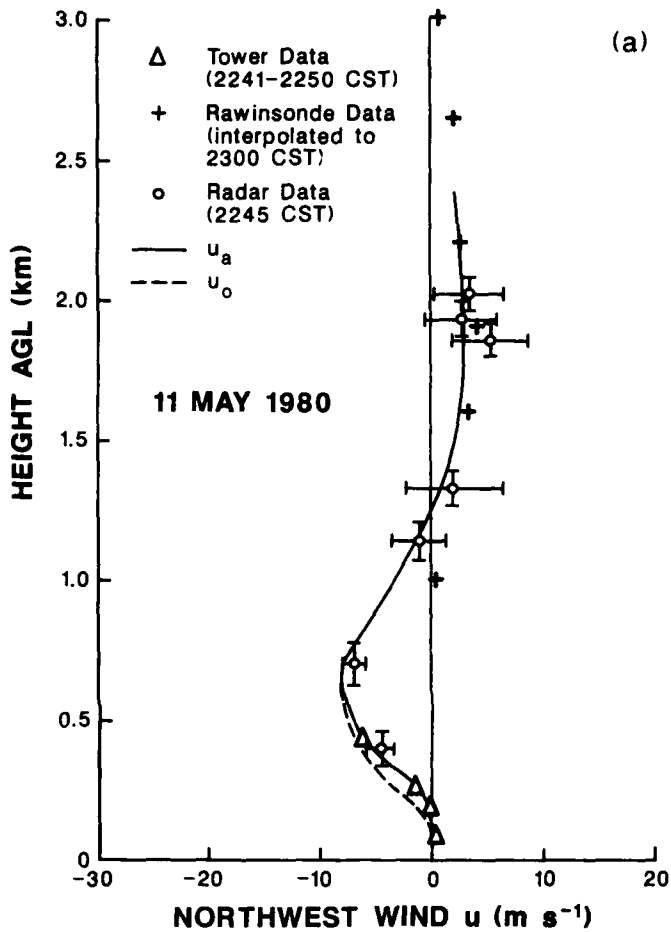
Figure 2a. The ambient wind component u_a, u_o in the direction of wave propagation. The $\triangle$ are data, from tower anemometers, averaged over the indicated 10-minute period. The u_a curve is fitted to these data, whereas the u_o curve is obtained from fitting data averaged over a 2 min period just preceding wave arrival at the tower. Open circles are wind components derived from single Doppler data fields and + are winds interpolated from earlier and later rawinsonde data.

2b. The averaged ambient wind component v_a, v_o in the direction orthogonal to u_a.

reduce the Doppler estimate variance, and pairs of averaged Doppler velocity data with about a 25° azimuthal spacing were used to estimate the wind. Several pairs of data were sought that were within the 1-km range interval at each elevation angle (to have estimates at nearly constant height) and the distribution of winds from these pairs were plotted.

It should be noted that the wind profiles shown on Fig. 2 differ from those given by Doviak and Ge. When comparing the Doppler data with the Doppler velocity predicted from the wind estimates given by Doviak and Ge, we find a poor fit for data at the 0.840 km altitude. This one poorly-estimated datum altered the wind profile significantly. Perhaps winds were not uniform as assumed, or the data selected were not representative samples. On the other hand, the least-squares-fitting method uses all data, and its wind estimates fit the radar data much better at this altitude, and it also gives estimates that have good agreement with tower data. We could not least-squares-fit the data at heights above 1.15 km because echoes were not detected at the 30 to 40 km ranges. But by decreasing the range and increasing elevation angles, we were able to detect echoes from the clear air. Unfortunately, most all of these data were contaminated by ground clutter, and we could not confidently apply the least-squares-fitting algorithm because it weighted excessively data that appeared in clusters with small azimuthal separation (from closely spaced data poor estimates of wind are retrieved; Doviak & Zrnic', 1984, Chapter 9). However, because Doviak and Ge subjectly selected Doppler velocity pairs that had large angular separation, and ones that appeared to be uncontaminated by ground clutter, they seem to have made valid wind estimates for all other heights. The fact that three wind estimates, at around the 2-km height, agree so well, even though they were obtained from data pairs at three different beam elevation angles (i.e., 2.9°, 3.7°, and 4.5°) supports the

validity of these wind estimates, as does the smooth wind profile connecting their datum at 1.36 km altitude with the least-squares-fitted datum at 1.15 km.

The horizontal bars, for the least-squares-fitted data, indicate the 95% confidence limits, assuming errors are Gaussian distributed and using the computed rms values of the data about the model velocity. The vertical bars denote the uncertainty in beam height for a 0.1° uncertainty in elevation angle, and also the variation in beam height because radar data from a 4-km range interval were used in the fitting. The solid lines in Fig. 2 are the inferred profiles of the ambient wind.

The winds measured by rawinsonde are values interpolated from sounding data at 1800 on May 11 and 0600 on May 12. The interpolated temperature profile (Fig. 3) is assumed to reasonably estimate the ambient temperature above the stable layer because there was less than a 2°C change over the 12-h interval between soundings and because the interpolated profile fits well the measured values at low altitudes. However, the wind field changed considerably during this interval, and the interpolated wind differs significantly from the radar-derived wind. Nevertheless, there is good agreement between tower- and radar-measured winds that are from data close to the same time. So we shall accept these estimates to be representative of the ambient wind field. Even though radar-derived wind data extend only to 2 km, it is the wind below 1 km that is important in altering the wave characteristics.

The difference in wind measured by the radar and tower at the common height of 400 m was most likely due to the combined effects of reflectivity gradients, beamwidth, and beam blockage. Beam blockage causes Doppler velocities to be biased toward those in the upper part of the beam. Because the profiles were derived from data in the azimuthal sector to the north, where
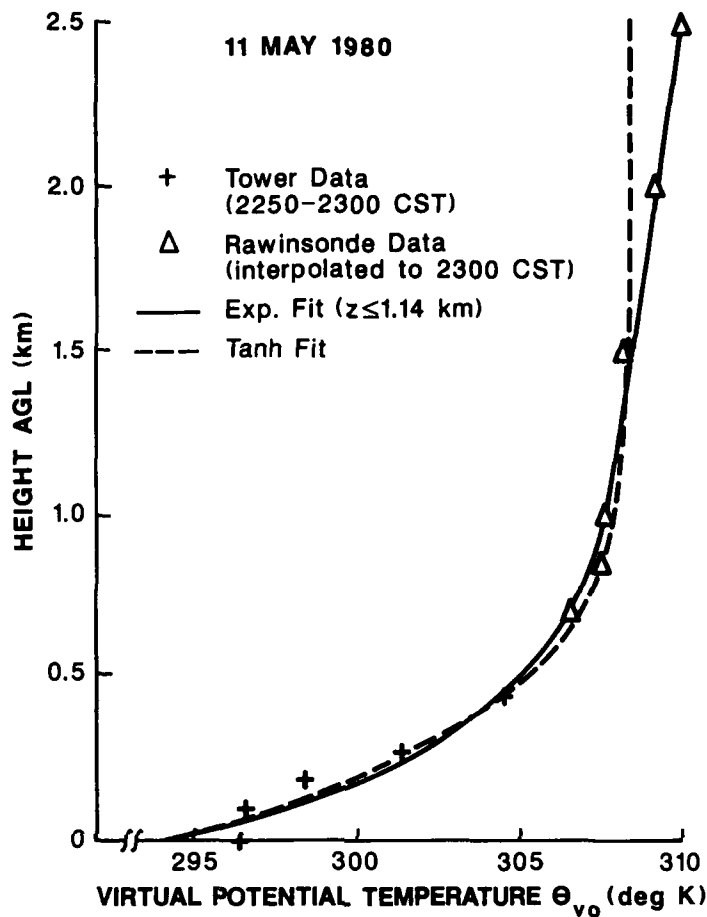
Figure 3.   Virtual potential temperature versus height above ground level
            (AGL) circa 2255 CST on May 11, 1980.

radial winds were increasing rapidly with height, beam blockage could account

for the larger velocity measured by radar at the 400 m altitude.

Another cause for differences is that the wind might not be uniform as

assumed in the model used to fit the Doppler data. For example, Fig. 2 shows

the ambient wind profile $\vec{v}_0$ averaged for the 2-min period just preceding the

solitary wave at the tower. Although the u component changed little from the

values deduced 15 minutes earlier, the v component underwent significant

change in the first few hundred meters of the atmosphere. We assume that

this $\vec{v}_0$ profile, to be used in Section 3.3, represents the values that the ambient wind would have had if the wave were not present.

Although the ambient wind could have changed during the 10-min period of wave passage, it is difficult to determine precisely the change, if any, that would have occurred. Examination of the wind and temperature after wave passage shows that, at altitudes below 100 m, there were quasi-permanent changes caused by the wave and its associated phenomena. At higher altitudes turbulent mixing, apparently induced by the wave, appears to have altered the mean flow. Therefore we could not deduce $\vec{v}_0$ within this 10-min period by interpolating between data at the beginning and end of the wave, so we have instead assumed that the ambient wind in absence of the wave would roughly correspond to an assumed constant $\vec{v}_0$ equal to that 2-min average immediately before wave arrival.

The u profile can be approximated by the function

$$u_0 \simeq 10 - 3.13z - 5.03 \times 10^3 (z+0.4)^{5.51} e^{-5.76(z+0.4)} \text{ m s}^{-1};$$
$$0.2 < z < 2.2 \text{ km.} \tag{3.2}$$

This function could be used to derive an estimate of the bulk Richardson number needed to determine the properties of the solitary wave. Because of the two-dimensionality of the wave, we should not expect shear of the v component to significantly modify the dynamical structure of the wave. Although the Richardson number of pertinence to the generation of Kelvin-Helmholtz waves, and possibly turbulence, requires the use of vector wind shear, we assume it is the Richardson number associated with u shear that is of crucial importance in determining wave properties.

Calculation of u_0'' and comparison with terms in the brackets of Eq. (2.12c) suggests that the ambient wind gradients cannot be ignored. Nevertheless, we solve the problem assuming $u_0'' = 0$ and accept the solution as a first approximation for eigenfunction ϕ. However, the approximate solutions might not be so terribly far from the correct ones because numerical solutions (Tung et al., 1981) show that, in the case of the lowest mode number wave (i.e., one for which there is no reversal in the vertical displacement of streamlines, and the one most likely observed here) for which the initial condition in the evolution equation is a solitary wave in a shearless environment, the wave in the presence of shear has the same shape as in the shearless case, but faster speed. These results apply to the situation in absence of critical levels where the background speed u_0 equals the wave speed. In our problem the wave speed is larger than 10 m s^{-1}, so critical levels should be absent. However, we show in Section 3.3 that vertical shear of u causes significant change in the magnitude of the observed wind perturbations. We account for the effects that u_0'' might have on $\phi(z)$ in a later report.

3.2. The Wave's Equivalent Potential Temperature

Contours of equivalent potential temperature (Fig. 4) show a pool of potentially cooler air (shaded area) within the wave, but somewhat lagging toward its rear. If the wave is steady, and the ambient atmosphere vertically stratified, air parcels travel along surfaces of constant θ_e, and thus Fig. 4 suggests that trapped thunderstorm outflow might have been recirculating within the wave, whereas the environmental air passed through the wave (or the wave passed through the environment) as it was lifted by it. Additional evidence of recirculating flow is presented in Section 3.3.5. Perhaps the trapped air was a cut-off vortex that initially formed at the leading edge of the

-47-
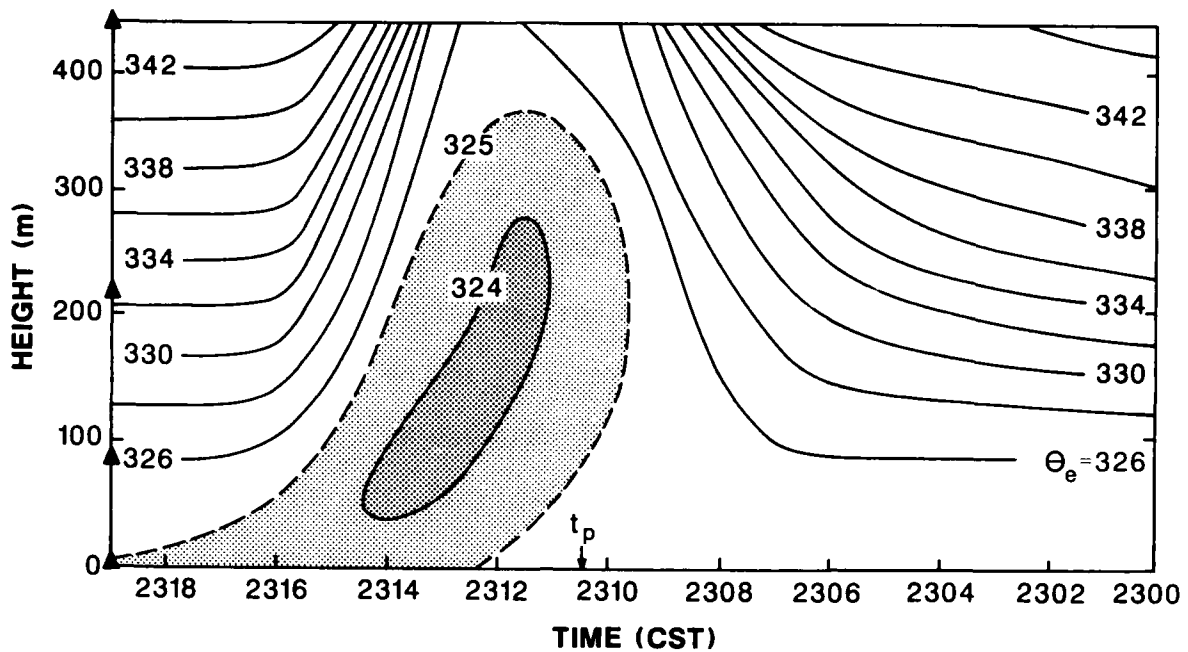
Figure 4. Equivalent potential temperature (K) in the NW-SE cross section through the wave. The shaded area denotes the approximate location of trapped thunderstorm outflow; t_p is the time (roughly the same at all tower levels) at which the wave produces a peak in the u wind component (See Fig. 6a).

horizontally spreading gravity current (i.e., the thunderstorm outflow) as it penetrated the stable layer. Although the formation of the vortex and its eventual separation from the gravity current is not fully understood, it seems reasonable to suppose that once the wave is formed with recirculating outflow inside it, the vortex is trapped by the wave and continues to propagate at the wavespeed, leaving behind the ever-slowing gravity current. The position of the pool of cool air at the trailing edge of the wave (Fig. 4) is evidence that the heavier outflow lagged the wave, giving credence to the idea that the wave dragged the trapped air, or at least the two had some symbiotic relation. If the trapped air in the wave were formed solely of ambient air, it should be

centered within the wave as the numerical results of Tung et al. (1982) indicate.

3.3. Wind Perturbations Observed With Tower Instruments

In Fig. 5a we present the position of the leading edge of the Doppler velocity perturbations (i.e., the wave front) caused by the wave as a function of time. This figure shows that the wave front passes NSSL's tall (444-m) meteorologically instrumented tower at about 2305. The storm that supposedly created this wave was about 100 km north of the radar at 2300 CST and was tracking to the east-northeast. Thus the wave front positions displayed in Fig. 5a are well to the south of the storm, and because there are no other storms south of this one, the wave propagated through an environment undisturbed by other storms. Although the front had curvature (see Section 3.4.1 for discussion of wave curvature) and changed orientation as the wave propagated in a generally southeast direction, it nevertheless had an azimuthal orientation of about 45° at the time it passed the tower. Therefore a time series of data spaced 10 seconds apart is plotted (Fig. 6) to show the temporal dependence of wind components u and v (orthogonal to and along the front) at five levels (7, 90, 176, 266, and 444 m). If we ignore the contribution of storm outflow (i.e., the shaded areas in Fig. 6b), these data exhibit, only at lower altitudes (i.e., $z < 176$ m), a definite wave-like velocity perturbation that is nearly wholly in the NW-SE cross section. However, at the highest anemometer levels (i.e., 266 and 444 m) pronounced wave-like perturbations appear in both the u and v components.

These observations complicate our comparison with theory, which assumes that velocity perturbations are in the plane orthogonal to straight wave
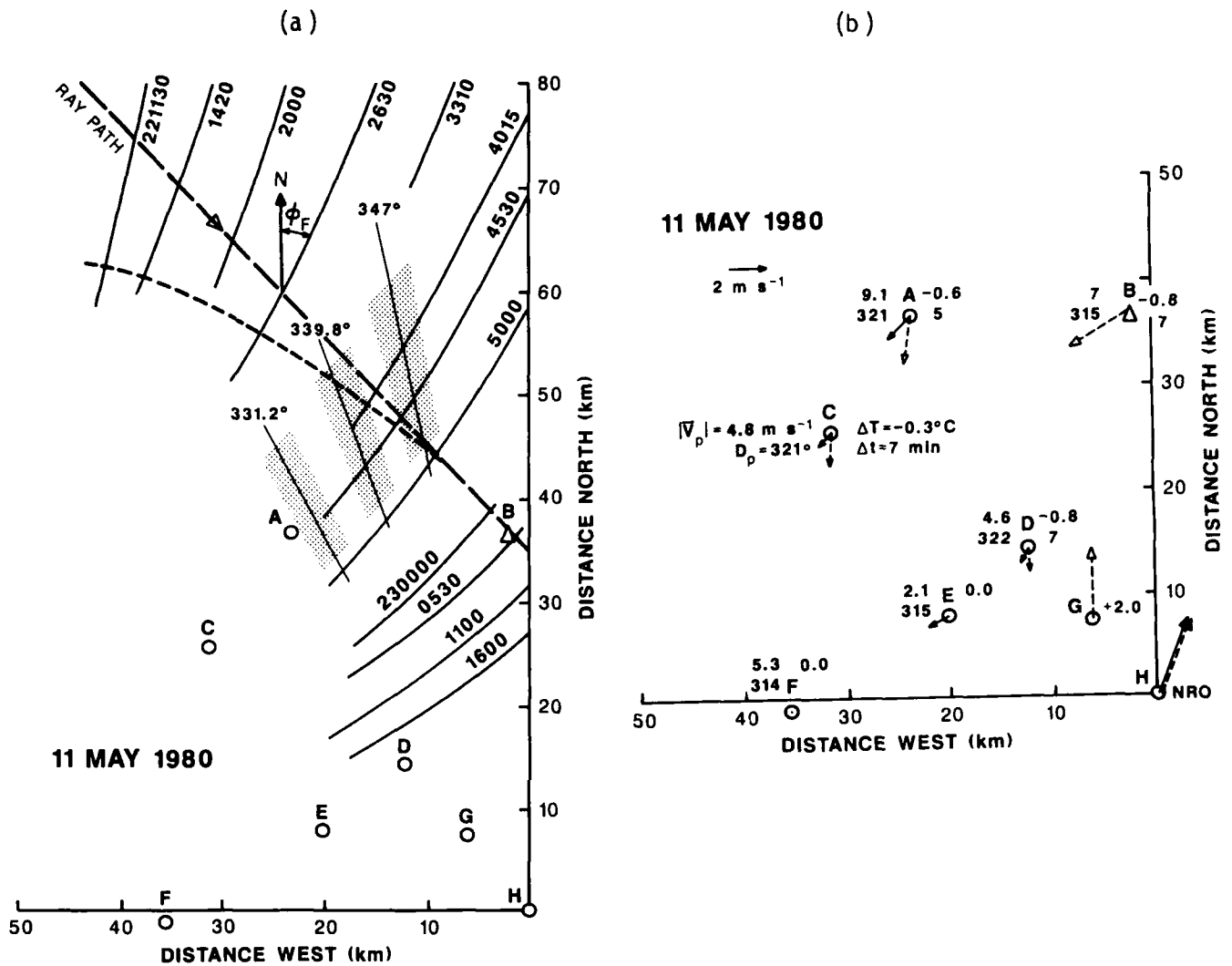
Figure 5a. Isochrones of the leading edge of Doppler velocity perturbations
produced by a solitary wave. The location of the 444-m tower is
indicated by the Δ, and the dashed line is the path of wave front
normals that pass through the tower location. The shaded sectors
highlight the zones from which Doppler data were extracted to de-
termine wave characteristics.

5b. The wind observed at surface sites A to G before (solid arrows)
and after (dashed arrows) wave passage. The 2 m s^{-1} vector scales
the wind. The magnitude $|\vec{v}_p|$ and direction D_p are for the wave's
peak disturbance of the wind, ΔT is the step-like temperature
change (°C) observed, and Δt is the time lag from wave front
passage to the occurrence of the steepest temperature decrease.

(c)

TEMPERATURE AND WIND AT SURFACE SITE 'A'

$$|\vec{V}_p| \equiv \sqrt{(\delta u')^2 + (\delta v')^2}$$

$$D_p \equiv 360 + \tan^{-1}\left(\frac{\delta u'}{\delta v'}\right)$$
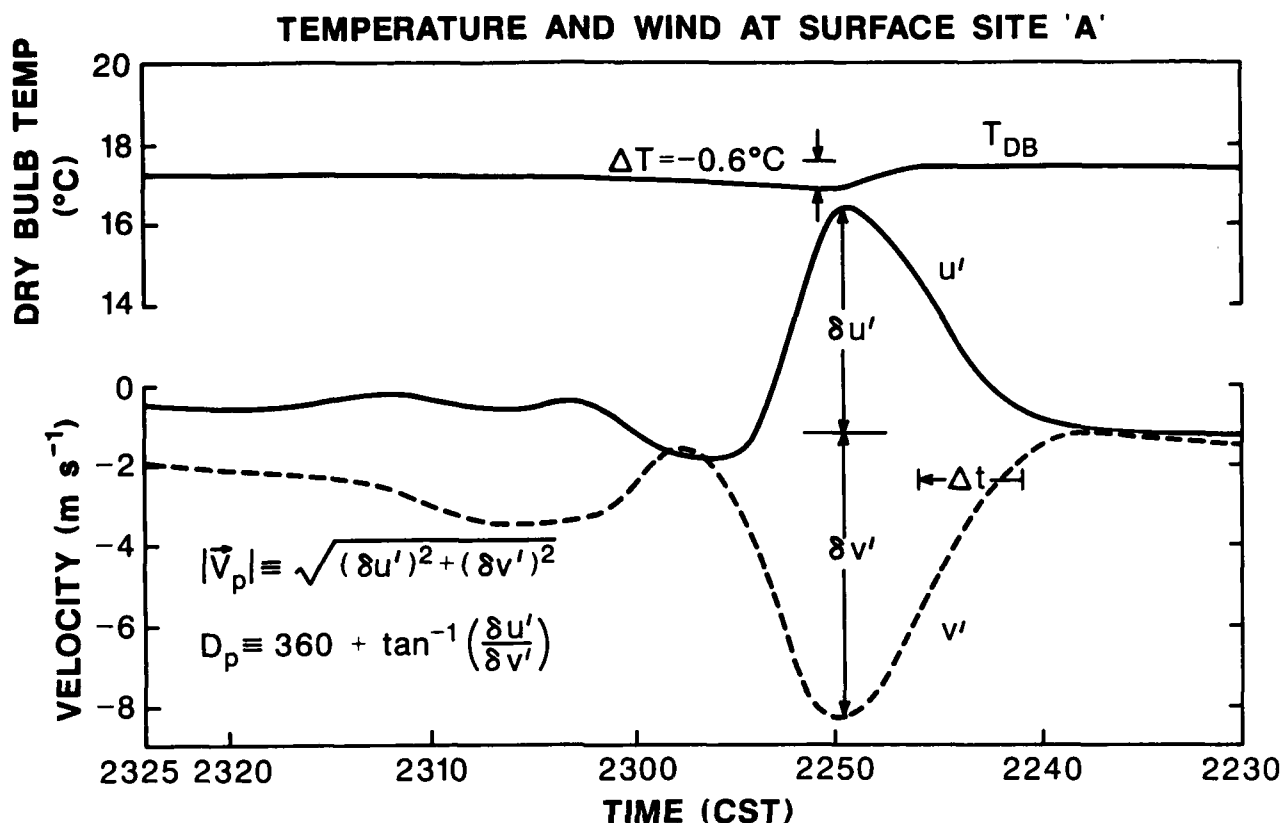
5c. The dry bulb temperature T_{DB} and wind components east (u') and
     north (v') recorded at station A during the time period 2230 to
     2325 CST. The lines through the data points are subjectively
     smoothed estimates of the temperature and wind and are shown to
     aid interpretation.

fronts. Furthermore, we need to decide whether to define the wave character-
istics at all times along directions perpendicular to the wave front, or in
the NW-SE cross section in which wave energy propagates (see Section 3.3.1) or
in the direction of the perturbation wind at the 444-m level, well above the
recirculating outflow. Wave characteristics (speed, wavelength, etc.) are
crucially dependent upon this choice and hence affect our comparison with
theory.
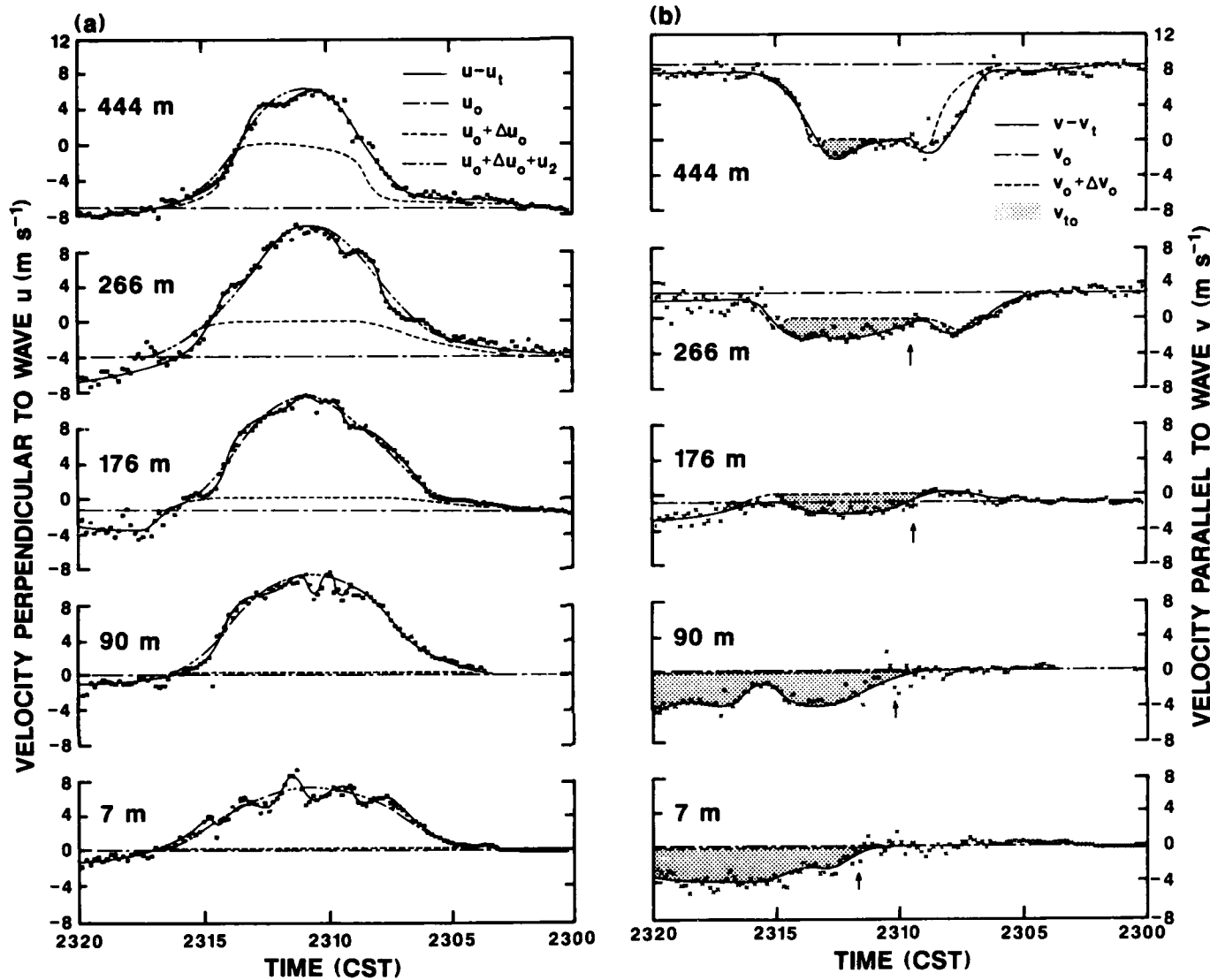
Figure 6a.   The observed (dots) u component of wind vs. time at five tower
             levels.   See text for an explanation of the various curves.
       6b.   Same as 6a, but for the v wind component.   The shaded areas are
             the winds attributed to thunderstorm outflow.

3.3.1.   The direction of wave travel and speed

It is natural to define wave characteristics along lines orthogonal to
the wavefront, but if the wave contains flow circulating in planes, then it

also seems reasonable to expect these circulations to remain in those planes, as the wave propagates, because angular inertia would resist turning. There would have to be an external force acting on the circulations to turn the axis of rotation. But there is no force other than gravity acting on the wave and this will not cause the axis to turn. Supporting this contention are meteorological data at the surface sites (Fig. 5b) which show that wave circulations remain in a plane whose direction is within a few degrees of the 318° mean value over the entire sampled length of the wave even though wave front direction changed considerably. If wave energy traveled in the plane of circulation, then rays of energy paths would be straight, although the speed of energy propagation would depend on the local characteristics (i.e., wave amplitude, inversion thickness, etc.) along the ray. It is not readily apparent from Fig. 6 that the wave circulations are entirely in a plane at all heights, but an analysis of Section 3.3.2 of wind perturbations shows that wave circulations are wholly within the northwest-southeast plane and hence the ray direction is southeastward.

The position of the wavefront along the curved line (i.e., the curve of dashes in Fig. 5a), orthogonal to the observed wave front at various times, is plotted in Fig. 7 from which we deduce a wave speed that decreases with time. To determine wave speed as a function of time along the ray path (Fig. 5a), we have also plotted in Fig. 7 the wavefront position along the southeast direction. Both curves show that the wave speed decreases as the wave propagates, but the rates of decrease are less at later times where it appears that speed might be approaching a steady-state value of about 12 m s^{-1}. However, the time of arrival of a wavelike velocity disturbance at surface sites to the south of the last radar observation indicate that wave speed may have decreased to values of about 10 m s^{-1} or less. We attribute this rather sudden
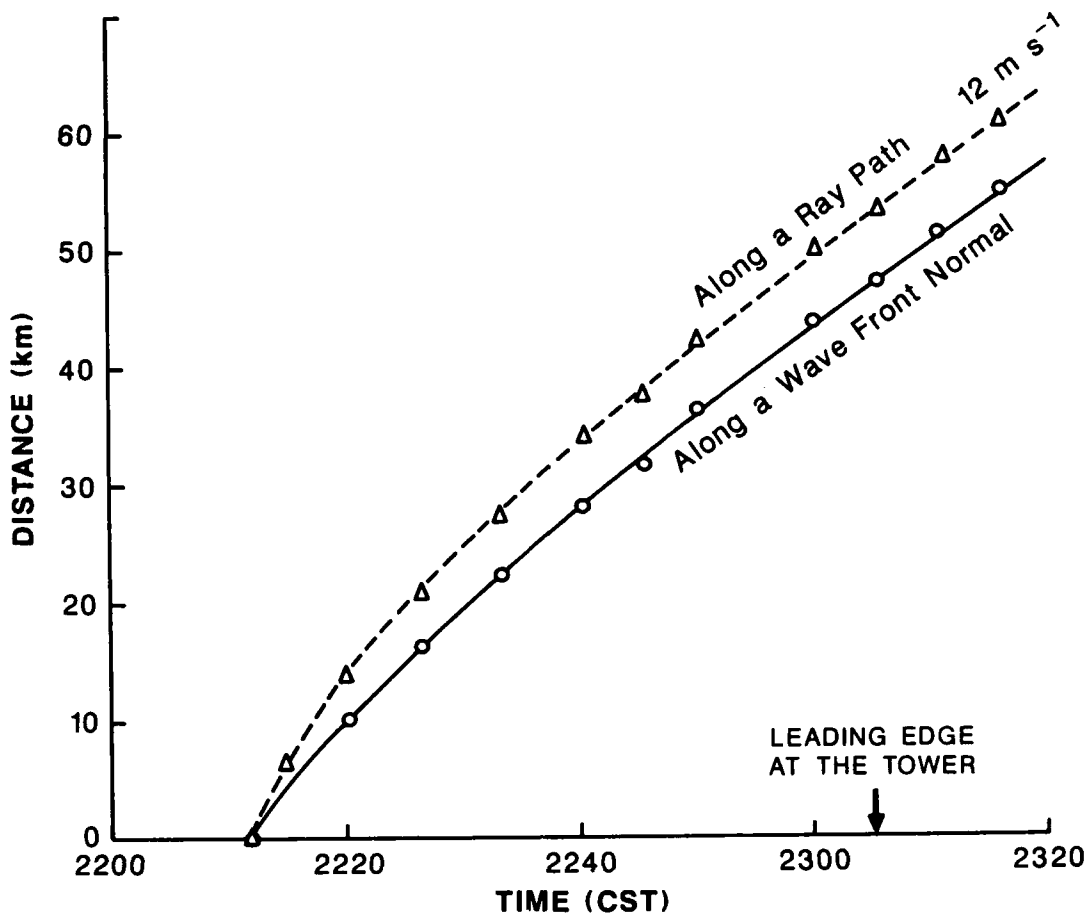
Figure 7.   Position of the leading edge of the wave perturbation along the
path of wave front normals (solid line) and along a ray path
(dashed line). Zero distance is referenced to front position at
221130.

decrease to a thinner inversion layer as the wave approached the leading edge

of the gravity current, generated by an earlier storm, which formed the inver-

sion layer (see Fig. 13 of Doviak and Ge, 1984).

The solitary wave speed given by theory is the group velocity of a wave

packet along a ray because the solitary wave comprises a group of spectral

components that form the packet. It is also the speed of wave energy. There-

fore we assume that the wave front speed, measured along the ray, equals the

wave speed given by theory.

3.3.2. The components of wind change and the plane of circulation

A close examination of the data suggests that the wind field can be ana-
lyzed in terms of six components,

$$\vec{v} = \vec{v}_0 + \Delta\vec{v}_0 + \vec{v}_2 + \vec{v}_{to} + \vec{v}_{KH} + \vec{v}_t \qquad (3.3)$$

where $\vec{v}_0$ is the background flow assumed horizontal in absence of the wave, $\Delta\vec{v}_0$
is the change caused by the wave when it vertically transports different
amounts of $\vec{v}_0$ momentum because of $\vec{v}_0$ shear, $\vec{v}_2$ is the flow that the wave would
produce if wind were uniform but $\vec{v}_2$ can include, for large waves, recirculat-
ing flow as demonstrated by Tung et al. (1982), $\vec{v}_{to}$ is the axial (i.e., paral-
lel to the wave crest) component of the trapped thunderstorm outflow, $\vec{v}_{KH}$ is
the velocity of well-defined, short, wave-like perturbations assumed to be
Kelvin-Helmholtz waves, and $\vec{v}_t$ is the contribution due to turbulence and other
ill-defined small scale-wind perturbations. The flow $\vec{v}_2$ is assumed to be in
vertical planes and its wind perturbations to be those given by the theory for
two-dimensional waves propagating in horizontally uniform media.

For argument's sake we have separated the solitary wave's wind into the
2-part $\vec{v}_2 = \vec{i}u + \vec{k}w$, applicable both within and outside regions of trapped
flow, and a component $\vec{v}_{to}$ assumed to be associated only with the trapped out-
flow. The orientation of our coordinate frame is selected so that the wave
component $\vec{v}_2$ lies wholly in the x,z plane oriented NW-SE. Because the wave
generated perturbations in three directions, parcels of air do not follow
paths that lie wholly in any vertical plane. Nevertheless, $\vec{v}_2$ deduced from
estimates of analyzed wind components is equal to $\vec{v}_2$ given by theory which
assumes flow soley in the plane perpendicular to the front.

Although the wave component $\vec{v}_2$ was in the NW-SE cross section at the time the wave passes the tower, we assume that wave perturbations $\vec{v}_2$ remained in that cross section irrespective of the wave location. Thus wave circulations would have been for the most part, oblique to the front because parts of the front advanced more rapidly than others in response to wave amplitude, inversion thickness, etc. As can be deduced from Eq. (2.48), solitary waves have speeds that increase with amplitude. Although this relation has been derived for waves of permanent form, we nevertheless assume for the case here, in which the wave is not exactly steady, that wave amplitude controlled wave speed in the same way. Wave amplitude was highest near the storm (see Section 3.4.4), and because of losses, amplitude decreased as the wave progressed with a speed determined by wave amplitude as well as inversion layer characteristics.

The above discussion leads us to deduce that wave energy propagated in the southeast direction irrespective of the wavefront orientation, and it is along this direction that wave characteristics (speed, wavelength, etc.) will be determined. The assertion that rays (i.e., energy paths) are not orthogonal to the wavefront might be surprising because the intuitive feeling is that wavefronts and rays are perpendicular to each other. But this is not necessarily so (e.g., see Whitham, 1974, Ch. 14, Sec. 7.9).

The interpretation that the wave component $\vec{v}_2$ remains in the NW-SE plane also helps to explain why the Doppler radar measured strong radial velocity perturbations (> 20 m/s) when the beam was pointed parallel to the wavefront near the thunderstorm. Although axial flow velocity v_{to} was also likely to be stronger there, we show in the following paragraphs that v_{to} is appreciably less than $\vec{v}_2$ at the heights above ground where the beam intersected the wave.

-56-

So it seems likely that it was the $\vec{v}_2$ component that was observed at large distances.

3.3.3. Wave guidance of thunderstorm outflow--the leaky pipe

The shaded areas in Fig. 6b are those perturbations that are assumed to be associated with trapped thunderstorm outflow. The arrows there indicate the arrival times of trapped outflow estimated from Fig. 4. It is seen that the onset of wind perturbations (the shaded areas in Fig. 6b) associated with trapped outflow agrees reasonably well with the location of the trapped air inferred from the θ_e = 325 K contour (Fig. 4) at all tower levels. However, trapped outflow barely reached the 444 m level. The oblong, closed contour of θ_e, trailing to the rear of the wave (Fig. 4) is evidence that the pool of cool air leaked out the rear of the wave in accordance with laboratory observations of fluid flow (Maxworthy, 1980). The component v_{to}, lingering after wave passage, gives further evidence that outflow leaked out the rear of the wave at altitudes below 90 m.

Additional evidence of leaked outflow is seen in the data of wind and temperature at surface sites (2 m above ground level, AGL) displayed on Fig. 5b. The recorded wind and temperature data are 1-min averages of samples spaced 10 s apart, and Fig. 5c shows a sample data set from station A. The solid arrows on Fig. 5b indicate the 10-min average surface wind immediately before wave arrival, and the dashed ones are winds after wave passage. Where arrows are not displayed the wind speed was less than 0.5 m s^{-1}. Also portrayed on this figure are the changes in dry-bulb temperature (°C) and the lags, in minutes, between the time of wavefront arrival (the beginning of velocity change), and the beginning of the step-like temperature change (see station C for the key to interpret this figure). The peak magnitude $|\vec{v}_p|$ of

the wave (i.e., of the 1-min averages) during wave passage is also portrayed on Fig. 5b and c along with the direction D_p from which the wind blew.

In all cases temperature drops did not recover within 30 or more minutes after the passage of the wave, thus indicating that trapped thunderstorm outflow was left behind. Remarkably there was no discernible step change in temperature at sites E and F, suggesting that all the trapped outflow had leaked from the wave before it reached those two sites. Furthermore there was little or no net wind change at these sites. Besides losing trapped outflow before reaching sites E and F, the wave had less amplitude compared with what it had at the sites farthest north. We thus conclude that the large-amplitude wave contained recirculating thunderstorm outflow, which continuously leaked out its rear, causing a concomitant decrease of wave amplitude. It is uncertain how much of this decrease in wave energy is associated with leakage and how much might be lost through waves propagating in the slightly stable region above the surface-based inversion layer.

Although we have deduced that the cool air behind the wave originates in the wave, one might question whether this cool air is a gravity current, and the wave, at its leading edge, its head of remarkably large amplitude. The ratio of gravity current head heights to the depth of the current behind the head, recently measured with radar for 25 cases (Mahoney, 1987), shows an average value of 1.14 and a maximum observed ratio of 1.35. Droegemeier and Whilhelmson (1987), working with numerical models of gravity currents, showed ratios as large as about 2. If the wave reported herein is the head of an advancing gravity current, its height is about 400 m and the depth of the current behind it is less than 100 m; it has a ratio larger than 4, an unusual value.

Although this observation cannot preclude cool air as a gravity current, more damaging evidence against this hypothesis is the disparity between the observed speed of the wavefront (or gravity current?) and that theoretically deduced. Noting that the depth of the gravity current h_g is less than 100 m, and that the difference $\Delta\theta_v$ in virtual potential temperature θ_{vg} of the current and the ambient air [i.e., $\Delta\theta_v = \theta_{vg} - \theta_{vo}(o)$]] is, at most, 0.8°C, the gravity current speed $c_g \simeq \sqrt{gh_g \Delta\theta_v / \theta_{vo}(o)}$ is approximately less than 2 m s^{-1}! This is markedly less than the observed speeds that are faster than 12 m s^{-1}.

Doviak and Ge (1984) assumed that a gravity current, impinging onto the inversion layer formed by the outflow of an earlier thunderstorm, generated the solitary wave, and this wave, propagating at speeds faster than the current, left it behind. Although we have examined data at the surface sites shown on Fig. 5 for times up to 4 hours after wave passage, we found no evidence of a current following the wave. Perhaps the current never reached these sites. It would have been fortunate to have surface sites farther north, but the sites displayed on Fig. 5 were the only ones operating in 1980. Thus, although data suggest that cool air behind the wave is leaked outflow, we have no evidence of a gravity current's initiating the wave that then propagates ahead of it.

Upon examining data from stations G and H we were unable to discern a solitary wave or any step decrease in temperature. On the contrary, at station G, temperature and wind increased (from 22.2° to 24.2°C and from 0 to about 3.5 m s^{-1} from the south) in a step-like way at 2330. No changes in wind or temperature were observed at H. If the wave propagated at the 10 m s^{-1} speed it roughly was observed to have had when propagating to site D, it would have arrived at site G at about 2238, or 8 minutes after the

-59-

beginning of the observed step-like temperature increase. Because wave speed is observed to decrease consistently as the wave proceeds, it is likely that the wave speed is less than 10 m s^{-1}, but certainly no more.

Doviak and Ge (1984) suggested that the wave never arrived at sites G and H because the wave outran the gravity current (generated by an earlier thunderstorm) that formed the inversion layer within which the solitary wave propagated. So the step increase was not associated with the wave. We attribute the increase in temperature and wind to an erosion of the pool of cool air that had been deposited, at 2142, by the outflow of the earlier thunderstorm. The outflow gravity current decreased the temperature, at this time, by about 3.0°C. The ambient flow south of this gravity current is southerly. We deduce that southerly ambient air, above the pool of cool air, mixed downward, erasing the inversion layer in 1 hour and 50 minutes, so that the solitary wave did not have a layer in which to propagate to site G.

On the other hand, Shreffler and Binkowski (1981) attributed similar step increases in temperature, observed far from thunderstorm outflows, to internal bores propagating on nocturnal inversions. However, because we did not observe any associated step increase in pressure to be expected to accompany bores initiated by thunderstorm outflows (on the contrary, the pressure decreased by a few tenths of a millibar shortly before the temperature rise), we affirm that the observed temperature increase is caused by downward mixing through a shallow inversion layer below a low-altitude wind jet (Fig. 2) and, furthermore, that this also is the likely mechanism to explain the temperature increase observed by Shreffler and Binkowski.

There is evidence that thunderstorm downdraft flowed along the axis of the solitary wave, thus replenishing some of that leaked behind the wave. However, it should be noted that the trapped outflow had sufficient volume to

easily cover, without replenishment, the ground with cool air between the storm and the wavefront when it reached the tower, about 60 km southeast of the storm. To demonstrate, consider the trapped outflow to occupy a cross section of the wave 0.5 km deep by 4 km wide, nearly that observed at 2310 in Fig. 5. If this entire air mass is deposited along the 60 km distance from the storm to the tower, it would cover the ground with cool air to a depth of about 30 m. However, examination of tower data at two other altitudes (26 and 43 m) suggests that the leaked outflow had a depth between 45 and 90 m. Considering that the trapped outflow probably occupied a much larger volume earlier, and that leaked outflow could be replenished, a deduced leaked outflow depth between 45 and 90 m is not unrealistic, and thus the observed cool air behind the wave could easily have been supplied by trapped outflow leaking from behind the wave.

The presence of this pool of cool air left behind the wave can complicate relating wind and temperature, measured with instruments 2 m AGL, to large-amplitude solitary waves having recirculation because the temperature drop and wind shifts might be construed to be evidence of an advancing gravity current on top and in advance of which wave-like perturbations can evolve (Crook and Miller, 1985). Only through observations with the tall tower do we gather evidence that the pool of cool air was a quite shallow (i.e., $\lesssim$ 100 m) trapped thunderstorm outflow which leaked out the rear of the wave.

We have shown that the wave trapped cool air having an axial component of momentum directed away from the storm. The axial momentum of the trapped air is generated by the thunderstorm outflow, which recirculates within the wave while being transported by it through the surrounding environment. However, the recirculating $\vec{v}_2$ and axial v_{to} momentum must be attenuated by drag forces of the ground and surrounding air as the outflow is directed away from the

storm by the "guidance tube" formed by the wave. Furthermore, because the trapped air was denser than its surrounding environment, it was continually leaking out of the "guidance tube" leaving behind a shallow pool of cooler air. It is remarkable that the storm outflow had remained in the wave for distances at least 60 km from the storm. Although storm outflows propagate as gravity currents to large distances from the storm, it is suggested that gravity waves and in particular solitary ones, formed by the interaction of the storm's downdraft with the stable layer, can transport the outflow faster and probably, with greater momentum, farther. Thus hazardous shear, normally confined to regions close to the storms might indeed be found at large distances from the storms.

3.3.4. Wind perturbations produced by the vertical transport of horizontal momentum

The $\Delta u_0, \Delta v_0$ components in Fig. 6 are estimated by assuming that parcels of air, traveling along lines of constant θ_e, do not change their momentum. Contours of θ_e should give an accurate depiction of parcel trajectories if the flow is steady and if the atmosphere is horizontally homogeneous. For example, Fig. 4 suggests that air from a height of about 100 m above ground was lifted by the wave to the 444 m altitude of the topmost anemometer. The pair of negative peaks seen in the $v_0 + \Delta v_0$ trace (Fig. 6b, top) was most likely generated as air, having the peak negative v_0 from the 180 m level (see Fig. 2b), passed twice through the anemometer at the 444-m level. Moreover, the shape and amplitude of the waveform $v_0 + \Delta v_0$ at the 444-m level, where the only contributions to changes in $v - v_t$ are from the vertical transport of momentum, agree remarkably well with the observed shape and amplitude. The good agreement of the observed data v and the wind change deduced from Figs. 2 and

-62-

4 suggest that turbulence is weak (i.e., rms values are less than about 0.5 m s^{-1}) and that $v_{KH} = 0$ at the 444-m level. However, at the 90-m level, Kelvin-Helmholtz waves might be the cause of the wave-like perturbation in v.

To compare observations with theory, we assume that $u - u_t - u_{KH}$ (dashed-dotted lines in Fig. 6a) is equal to the sum of Δu_0 due to wave-induced vertical transport of u_0 momentum, the ambient flow u_0, and the wave component u_2 obtained from theory for shearless profiles. The dashed-dotted curves are subjectively estimated to filter turbulence and the apparent wave disturbances that appear to develop in the solitary wave.

Near the ground there is no lifting of air so that $\Delta u_0 = 0$ and hence the wave component u_2 is well estimated from the dashed-dotted curve. Moreover, vertical velocity data show insignificant lifting below 90 m as does Fig. 4 and furthermore, because the vertical shear of u_0 was nearly zero below 100 m (Fig. 2a), u_2 is also given by the dashed-dotted curve at the 90-m tower level. However, at the 266-m level, u_0 was about -4 m s^{-1}, and air of zero momentum was lifted from near the 100-m level, so we can expect that Δu_0 had a peak of about 4 m s^{-1}. The dashed lines on Fig. 6a are the estimates of $u_0 + \Delta u_0$ obtained from Figs. 2a and 4. At the 444-m level, u_0 was much more negative (i.e., -7 m s^{-1}) and because air from near the 100-m level was also brought to this topmost tower level, the peak change in Δu_0 should be about 7 m s^{-1}.

3.3.5. Wave characteristics from tower data

The difference between the trace of $u_0 + \Delta u_0$ and the dashed-dotted one in Fig. 6a gives the estimate of u_2, the wave component to be compared with theory. The amplitude of u_2 and the wave's half-amplitude width $\ell_{1/2}$ are plotted on Fig. 8. The half-amplitude width is determined using the 12 m s^{-1}
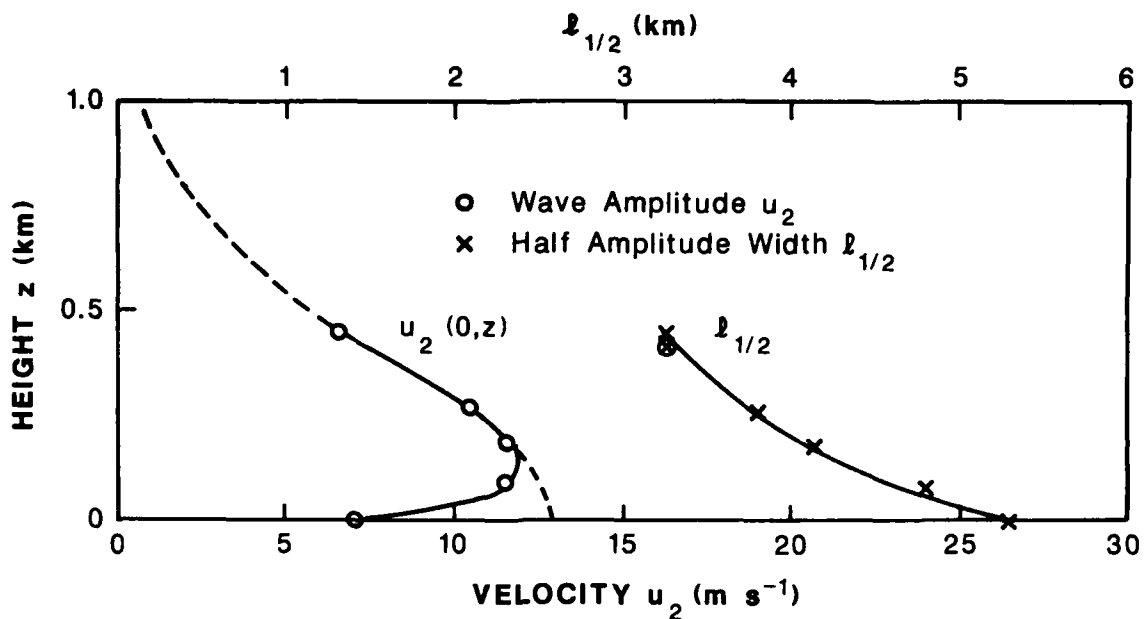
Figure 8. Amplitude of u_2 and half-amplitude width $\ell_{1/2}$ vs. height. Circled x is $\ell_{1/2}$ estimated from radar data (Table 3.2). The dashed lines are extrapolations based upon the eigenfunctions of weakly nonlinear theory and ignoring friction at the surface.

speed estimated (Fig. 7) for the wave when it passed the tower. Above 100 m altitude the wave amplitude decreased monotonically as expected from theory. The relatively small value of the observed wave amplitude (7 m s^{-1}) at 7 m altitude is attributed to the effects of drag caused by the terrain and/or mixing of a r by convective instabilities that develop when cool air is atop warm ground. Without effects of drag it is expected that wave amplitude at the surface would have been 13.0 m s^{-1} (see dashed curve on Fig. 8). The projected 13.0 m s^{-1} amplitude of the horizontal velocity perturbation u_2 at the surface is a little faster, at this time, than the wave propagation speed c = 12.0 m s^{-1}. This gives additional evidence that trapped air is recirculating when it passes the tower.

The dashed line for u_2 above 444 m is an extension based upon the eigen-function solution of weakly nonlinear theory discussed in more detail in Section 3.5. Although the data above 150 m extend over too short a height interval to give confidence that they confirm the eigenfunction form, the data are at least consistent with this shape. However, weakly nonlinear theory shows that half-amplitude width should be constant within h_s, and above the layer of stratification it should slowly increase with height (see Eqs. 2.33e and 2.34). Although the decrease in $\ell_{1/2}$ at the tower levels near the surface could be explained in terms of denser air leaking out the rear of the wave as seen in Fig. 4, there is an inexplicable decrease of $\ell_{1/2}$ for heights well above the surface. Perhaps the $u_0 + \Delta u_0$ traces in Fig. 6a are not accurately representing the changes in u due to vertical transport of horizontal momentum. A more rounded shape of the Δu_0 waveform at $z = 444$ m would result in an $\ell_{1/2}$ larger than 3.2 km. Because Δu_0 is estimated assuming parcel trajectories follow θ_e contours (Fig. 4) it is possible that humidity might have significant horizontal gradients, which would cause erroneous estimates of trajectories. On the other hand, the presence of trapped air could cause the wave to be broader, and thus the decrease of $\ell_{1/2}$ with height would be due to the lessening amount of outflow air. On the contrary, numerical solutions for solitary waves in a three-layer-deep fluid show, for strongly nonlinear waves, that wave width increases with height (e.g., Davis and Acrivos, 1967a, Fig. 2). This dichotomy might be explained by the fact that the observed trapped air is denser than the surrounding air and hence more of it will settle to the surface; whereas, in the numerical model recirculating fluid has the same density.

At the 7-m level, short wave-like features appear to grow in the solitary wave. These short waves decreased in amplitude with height so that they were

barely discernible at the 90-m level. Data at the 26-m and 43-m tower levels (not shown here) also exhibited waves that had temporal coherency with that observed at the 7-m height. These short waves appear to be Kelvin-Helmholtz (K-H) waves that grew on the leading edge of the solitary wave. Prior to the wave passage, the vertical shear was zero in the lowest 100 m of the atmosphere, but the wave generated a strong shear in the first few tens of meters above the ground where $d\theta_{vo}/dz$ was nearly zero (Fig. 2), and hence the Richardson number is then nearly zero. These K-H waves grew and then decayed as the solitary-wave created shear vanished.

On the other hand, there might be an alternate explanation for these short-wavelength waves atop the longer solitary wave. Keulegan and Carpenter (1961) observed that internal waves generated vortices in the stratified layer separating two homogeneous fluids of different densities. But these vortices appeared only when the thickness of the stratified layer became larger than some critical value, an observation that is in direct opposition to what would be expected if the vortices were due to K-H instabilities. Davis and Acrivos (1967b) examined this problem both experimentally and theoretically and showed that resonantly interacting disturbances can induce an instability and, when viscous dissipation is accounted for, their analysis gives the minimum amplitude at which a wave is unstable. Although we shall label the observed short-wavelength disturbances as K-H waves, further investigation is required to determine whether the observed waves are induced K-H waves or those produced by resonant wave interactions.

3.4. Wave Characteristics Observed Using Doppler Radar

Although the tower data give high-resolution in situ velocity measurements, the Doppler radar has the advantage of measuring the radial component

of velocity over a large area. Thus, only with radar could we have deduced that wave fronts are curved as shown in Fig. 5. Furthermore, the radar data give a direct measure of wave speed. On the other hand, because we did not observe the wave with NSSL's two separated Doppler radars, we need to estimate wave perturbations u_2 from single radar data. This determination is further complicated by the large beamwidth (0.8°) and the uncertainty in beam height due to the presence of the strong inversion layer and reflectivity gradients. Notwithstanding these difficulties, much information about the wave can be derived from radar observations.

3.4.1. Wave front curvature and wave speed

As pointed out in Section 3.3, data suggest that thunderstorms, which passed earlier in the evening, deposited a pool of cool air to establish an inversion layer on which a solitary wave was initiated by a later storm. This wave then propagated to the southern edge of the pool (estimated to be about 20 km south of the tower) where it finally dissipated. The orientation of the pool's southern boundary is neither easily nor confidently determined using data from the sparse number of surface stations, but it appears to be aligned along a southwest to northeast line. Although the pool of cool air was generated by thunderstorms, it appeared to form a relatively homogeneous inversion layer, at least away from the immediate boundaries. The contention that the inversion layer was relatively uniform is supported by the surface data, meager as it was, and radar observations that the wave front is straight when it is far from the storm (see Fig. 9). A straight wave front results when the wave propagates at a constant velocity along the front, a condition expected when the environment is uniform and the wave amplitude is constant or small. Supporting evidence comes from the field of Doppler velocities observed in the
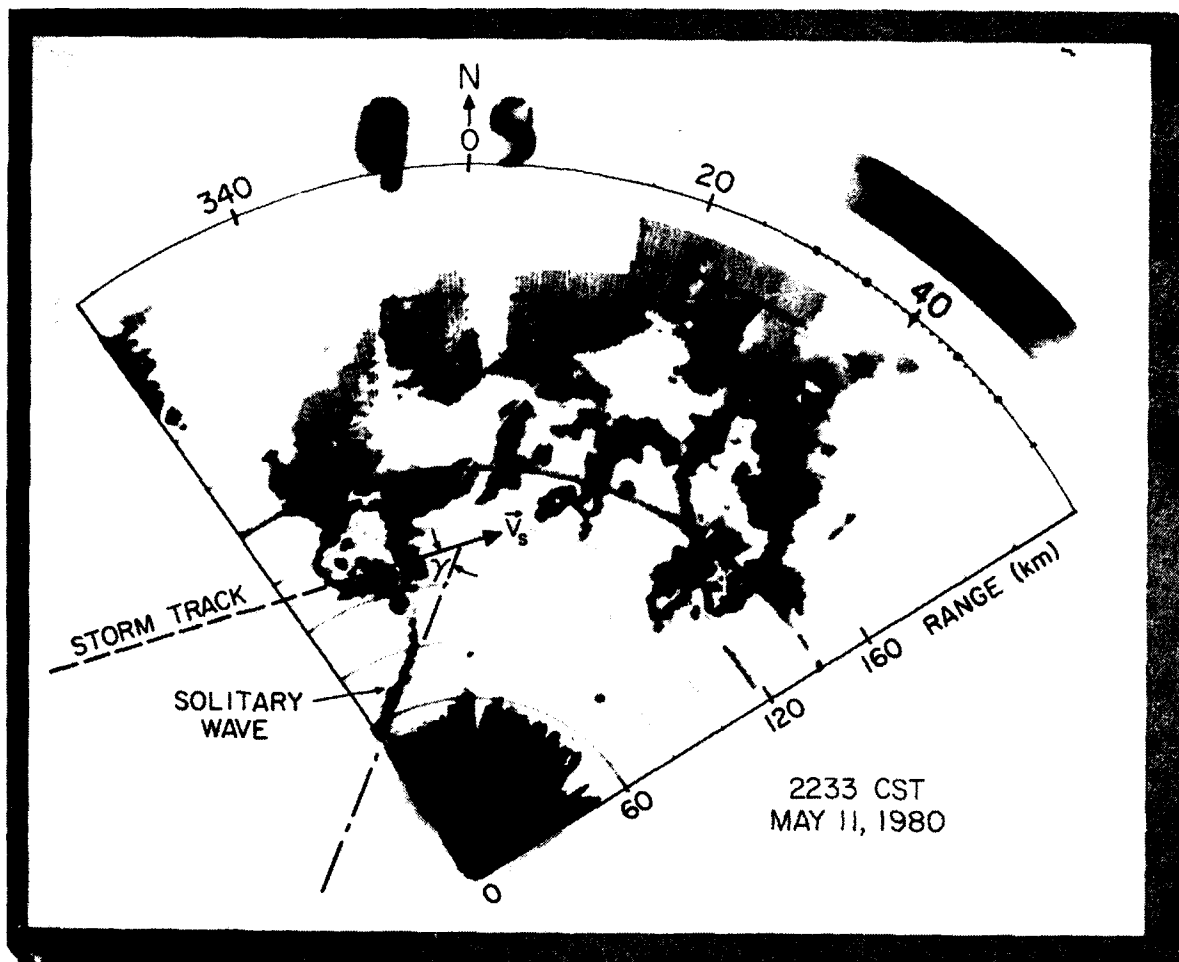
Figure 9.   Plan Position Indicator (PPI) display of echo power contours
            (boundaries of shaded areas) in about 10-dB steps, showing the
            solitary wave joined to the storm that created it. Maximum re-
            flectivity factor in the storm is about 55 dBZ. Elevation angle
            is 0.4°. V_s is the storm velocity vector.

northwest quadrant at low elevation angles before wave arrival that, comple-

mented with data from the few surface stations, show a large shallow pool of

air moving to the south.

        Although we didn't have a sufficient number of surface stations or

in situ data to determine the homogeneity of the atmosphere in which the wave

propagated, it is to be noted that the temperatures, before wave arrival at stations A, B, C, were within 0.3° of 17.7°C, whereas temperatures at stations D, E, F, were 2 to 3° higher. However, these higher temperatures to the south are attributed to the stations being close to the southern boundary of the pool of cool air. It is about there where the wave finally met its demise. Thus to the north where radar and tower observations of the wave were made, surface station data support the premise that the inversion layer was homogeneous.

It can be shown that if a disturbance is generated by a source moving at uniform velocity $\vec{V}_S$ in a homogeneous environment, the disturbance's wavefront should be straight, analogous to a shock front formed by a projectile transversing a homogeneous medium at speeds faster than the wave speed. Because the wave source was within the storm its velocity can be estimated by plotting the location of the storm's peak reflectivity during the 1-h period of observation. These locations fell nearly in a straight line and the positions versus time of the projections of these locations onto the line are plotted on Fig. 10. We thus deduce a uniform source velocity of 24 m s^{-1} along a track directed 73° from north.

However, surprisingly, the wave fronts are not straight but show a definite curvature near the storm. Furthermore, Fig. 5 shows that the wave front is shifting from a north-south orientation when close to the storm, to a northeast-southwest alignment when the wave propagates away from its source. Nevertheless, the front becomes straighter the farther the wave is from the storm (Fig. 9).

The fact that the wavefront remained behind a line drawn orthogonal to the track at the source location is evidence that the source (i.e., the storm) propagated at speeds faster than the wave. In other words, the source of the

-69-
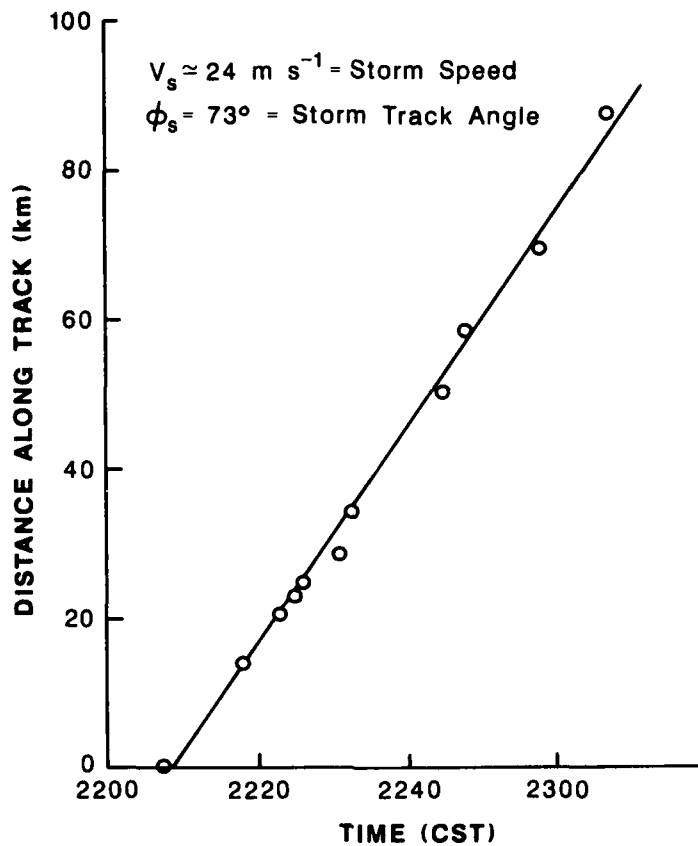
Figure 10. The storm's peak reflectivity position vs. time along the storm's track along the ground.

solitary wave moved at speeds corresponding to an effective Mach number larger than unity. If the wave speed c were constant, the wavefront would have formed a straight line emanating from the source at an angle γ to the track. Then we could have used the Mach relation

$$c = V_s \sin \gamma \qquad (3.4)$$

to derive an estimate of wave speed. However, this relation is based on the assumption that wave velocity is perpendicular to the straight wavefronts, whereas the front observed here is curved and changes orientation as it propagates southeastward. Nevertheless, where the wavefront is straight, it can be

shown that Eq. (3.4), applied to these wavefront portions (Fig. 9), gives the steady final speed of the wave. We attribute the curved wavefront to a decreasing speed of propagation as the wave progresses from its source. However, this decrease is not caused by spatial changes in the ambient environment, but by the dependence of wave speed on its amplitude. Further complicating the use of Eq. (3.4) is the fact that the atmosphere is moving generally in a northerly direction (Fig. 2) and thus the source velocity that is required in Eq. (3.4) is the one relative to the moving frame, whereas Fig. 10 gives the velocity in the stationary earth frame. Thus the source velocity will have a more southerly direction and a slower speed. However, because the inversion layer and wave energy is confined to the first few hundred meters of the atmosphere, where the ambient flow is slow, we expect that our estimate of $\hat{V}_s$

is not ruined.

Because the wave was trapped in an inversion layer, wave propagation is one-dimensional, contrary to the two-dimensional (2-D) flow of a shock wave in a totally uniform fluid. Thus, there was no amplitude decrease due to wave spreading as we would have in an expanding cylindrical shock wave. The decay in amplitude for the trapped wave was a result of energy being lost because some of the components that constitute the solitary wave propagate away through the slightly stable layer above $h = 1.14$ km (Chen, 1985) and/or energy can be lost through leakage of recirculating thunderstorm air trapped in the wave, analogous to leakage observed in laboratory experiments (Maxworthy, 1980).

If c decreased with distance from the source because wave amplitude decreased, then it can be shown that the wavefront should have had a convex shape as observed in Figs. 5 and 9. Although wave amplitude was highest near the source and decreased as the wave progressed southeastward, it should be

noted that this may not always be the case. Christie and Muirhead (1982) solved the equation of evolution (Eq. 2.24a) and showed that solitary waves of increasing amplitude can evolve out of longer wave, smaller amplitude, disturbances.

Although wave amplitude decreased in the case discussed herein, causing wave speed to decrease which in turn caused wavefront curvature, energy is hypothesized to propagate along rays as deduced in Sections 3.3.1 and 3.3.2. It can then be shown (Appendix C) that the Mach relation takes the modified form

$$c_m = \frac{V_s \sin \gamma}{\sin(\gamma + \mu)} \tag{3.5}$$

where μ is the angle between the ray direction (135°) and the direction ϕ_s of source propagation, and γ is the angle between the source path and the line tangent to the wavefront at the location where wave speed is estimated. Thus, $\mu = 135 - \phi_s = 62°$. At the time the front passed the tower, $\gamma = 28°$. Substituting these values and our estimate for V_s into Eq. (3.5), we obtain $c_m = 12.4$ m s^{-1} in reasonably good agreement with the speed $c_t = 12.0$ m s^{-1} deduced from tracking wavefront position versus time along the ray (Fig. 5). Although the agreement is not as good at earlier times (see Table 3.1), both estimates show that c decreases with time. Furthermore, this decrease slows with time so that c seems to approach an asymptote of about 12 m s^{-1} or, at least, to decrease at a much slower rate after 2311. It is unfortunate that data collection stopped at this time. Estimates of wave speed by these two independent methods both show that wave speed decreased by a factor of 2 over the period of observation.

Except for the earliest and latest time, the wave speed c estimated using Eq. (3.5) is somewhat higher than the speed c determined by tracking frontal

position along the ray. This difference could be attributed in part, to the northerly flow of the ambient air which causes the storm track to advect so that ϕ_S is larger and V_S is smaller. The wave speed c tabulated in Table 3.1 is measured relative to the ground but it is c', the wave speed in the coordinate frame advecting with the medium, that needs to be compared with the theoretical estimates presented in Section 2.3. We now consider the effects of advection.

Table 3.1. Comparison of wave speed c_m from the modified Mach relation Eq. (3.5) and wave speed, c_t, computed from tracking frontal position along a ray passing through the tower.

TIME	ϕ_F*	γ	c_m(m s^{-1})	c_t(m s^{-1})
221130	13°	60°	24.5	--
221420	18°	55°	22.1	26.0
2220	21°	52°	20.7	20.5
222630	27°	46°	18.2	17.2
223310	29°	44°	17.3	15.9
224015	33°	40°	15.8	14.1
224530	34°	39°	15.4	13.3
2250	36°	37°	14.6	12.6
2300	40°	33°	13.1	12.0
230530	42°	31°	12.4	12.0
2311	45°	28°	11.3	12.0

* ϕ_F Azimuth angle of the front at the intersection with the ray (Fig. 4).

$\gamma = \phi_s - \phi_F$.

Note: Wave front passed the tower at 2305.

The velocity at which the wave advects is difficult to estimate because the wind is nonuniform in height, and does vary somewhat along the horizontal and/or time as indicated, for example, by the difference in the ambient wind (Fig. 2). However, because most of the wave's energy is confined to the lowest 400 to 500 m of the atmosphere, we assume that it is within this layer that an unweighted average of the ambient wind determines the advection velocity. From Fig. 2 we estimate the advection velocity

$$\langle \vec{v}_o \rangle = \vec{i} \langle u_o \rangle + \vec{j} \langle v_o \rangle,$$

(3.6a)

-74-

to be approximately

$$\langle u_o \rangle \simeq -2.5 \pm 1 \text{ m s}^{-1} \tag{3.6b}$$

$$\langle v_o \rangle \simeq 2.0 \pm 1 \text{ m s}^{-1}. \tag{3.6c}$$

The angle brackets (< >) denote a vertical average, and the error limits arise from the uncertainty in the vertical profile of the wind and the height interval over which the average needs to be made. A more complete theory, which accounts fully for the effects of wind shear, needs to be made in order to precisely estimate the advection velocity and the effects that shear has on wave characteristics.

The storm velocity vector $\vec{V}_s'$ in the frame advecting with velocity $\vec{V}_o$ is

$$\vec{V}_s' = \vec{V}_s - \langle \vec{V}_o \rangle, \tag{3.7}$$

and it is $|\vec{V}_s'|$ and ϕ_s' that need to be used in Eq. (3.5) for moving media. The estimates of $\vec{V}_s'$ give

$$|\vec{V}_s'| = 23.6 \pm 1.5 \text{ m s}^{-1} \tag{3.8a}$$

$$\phi_s' = 80.7 \pm 3.5°. \tag{3.8b}$$

Using these values in the Mach relation we compute c_m', the wave speed in the moving coordinate frame. The c_m' values are plotted onto Fig. 11 along with error bars that denote the variance in our estimate of c_m' caused by the ± 1 m s^{-1} uncertainty in advection velocity. We also estimate c_t', the wave
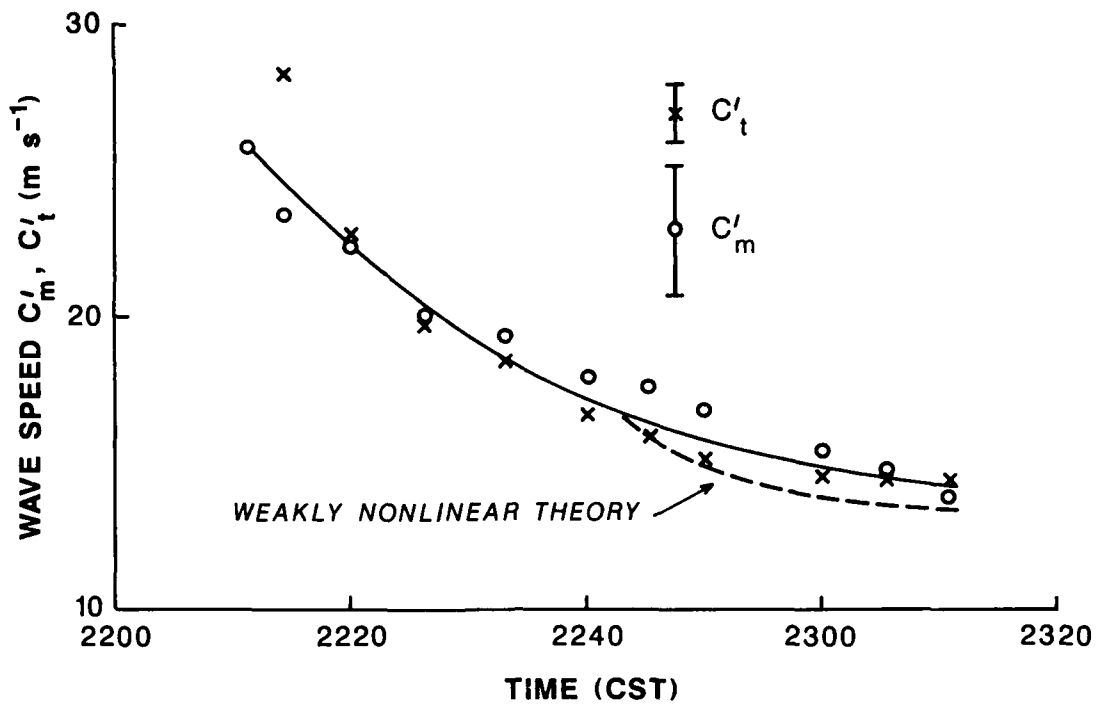
Figure 11. Wave speed versus time. c_m' is wave speed computed using the Mach relation, and c_t' is the wave speed computed from tracking wave fronts. The solid line is the estimated actual wave speed.

speed computed from tracking wave fronts in the moving frame. The $\langle v_0 \rangle$ component does not affect c_t because v_0 is normal to the direction of propagation. Thus

$$c_t' = c_t - \langle u_0 \rangle \pm 1 \text{ m s}^{-1}. \tag{3.9}$$

These c_t' values are also plotted onto Fig. 11 to compare with c_m'. We note that the two independent estimates of wave speed agree better than those in Table 3.1, but more importantly, it shows that the wave speed to be compared with theory is faster than the speed observed relative to the ground and listed in Table 3.1. The c_t' value at the earliest time might be an

-76-

overestimate because then the wave is at long range from the radar, and hence the beam intersects the wave at higher altitudes. Since the wave has a gentle sloping front, the range of the leading edge of the wave will appear to be at longer ranges than the leading edge near the ground. Thus c_t' would appear to be larger than it actually is. The solid line in Fig. 11 is the subjectively estimated actual wave speed when the earliest c_t' datum is ignored.

It would also be helpful to have a rigorous theoretical treatment to determine whether ray paths for nonlinear waves created by a moving source are indeed straight when the medium is homogeneous, to determine the curvature of the front, and to determine the relation between wave front speed, wave characteristics, and the ambient air characteristics.

3.4.2. Doppler velocity perturbations

At 2245 the radar beam intersects the wave to the northwest at ranges of about 50 km. This is about the latest time for which we have digitally recorded Doppler data to derive quantitative estimates of velocity profiles along the beam. Data at this time have the best spatial resolution (700 m) because the wave is nearest the radar.

In Fig. 12 we present the radial component v_r of the wind deduced from Doppler velocity measurements through the wave at 2245. Each curve is Doppler velocity data averaged over a 4° azimuthal sector (see Fig. 5) for a beam elevation angle of 0.4°. Each sector contains radial velocity data along four or five beam positions, and the data are spaced 180 m apart along the beam. A wave profile along each radial is then subjectively fitted to the data, and the four or five fitted profiles are then averaged to form a velocity profile for each sector centered at azimuth ϕ_c. The vertical bars on Fig. 12 indicate the Standard Deviation, S.D., (plus, minus) of the fitted profiles. The S.D.
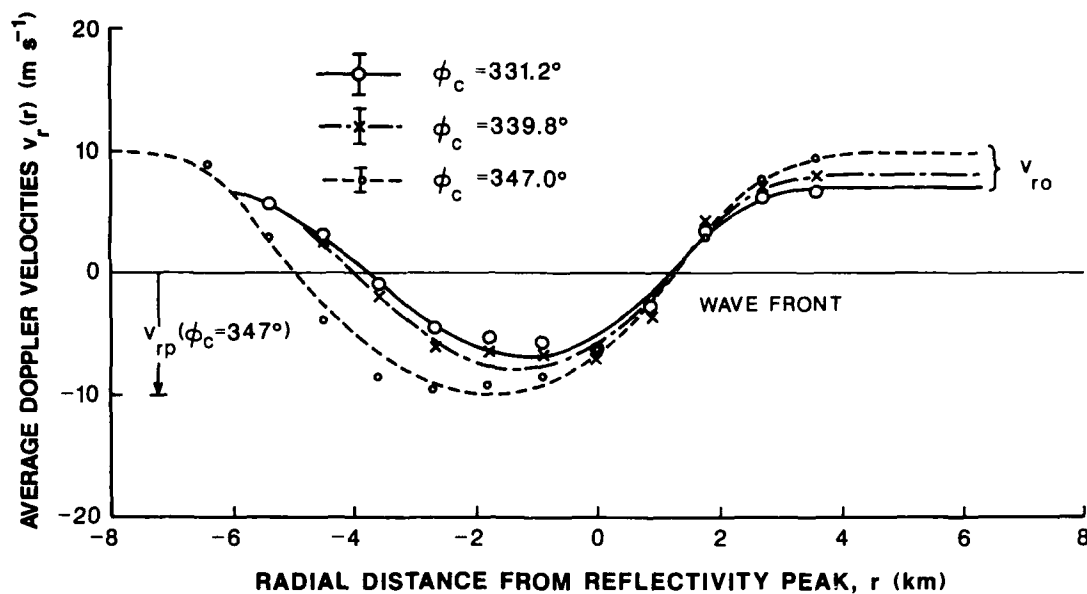
Figure 12. Average radial velocity in each azimuth sector of about 5° width centered on ϕ_c vs. radial distance from the wave's reflectivity peak. Vertical bars are the estimated standard deviation of the data. v_{ro} and v_{rp} are the radial components respectively of the ambient wind in advance of the wave and at the wave peak.

is obtained by computing, at ranges spaced 900 m apart, the S.D. of the fitted profile at each range, and then averaging the S.D. for all ranges in the wave. The averaged profiles are then plotted on Fig. 12 along a distance scale that is relative to the location of peak of the wave's reflectivity used to obtain a reference distance.

3.4.2.1. Wave reflectivity

It is observed that the peak in horizontal velocity perturbations lags behind the peak of reflectivity by about 1 or 2 kilometers, an unexpected re-sult. Because the reflectivity factor Z (Doviak and Zrnic', 1984) of the am-bient environment has a strong vertical gradient (-17 dBZ/km), but is

otherwise horizontally homogeneous, we should expect peak reflectivity to occur at the location of the wave crest. The observed difference is attributed to the response of insects and/or night-flying birds or mammals (which are assumed to be the targets) to the wave. As they are lifted by the wave they become cooler, and we assume they would fly downward to try to maintain their temperature. Since the vertical velocity, estimated with the anemometer at the 444-m tower level and averaged over the time that targets are being lifted, is about 1.5 m s^{-1} and less at lower heights, the insects/birds should easily manage to descend fast enough to alter the reflectivity profile during the wave passage, and thus cause peak reflectivity to precede peak wave displacement.

The hypothesis that insects or birds are the targets is supported by the large scatter of the mean Doppler velocity estimates from one resolution volume V_6* to the next V_6 (Doviak and Zrnic', 1984) and the unusually high equivalent reflectivity factor (10 dBZ_e at 300 m altitude) in the otherwise clear air. Clear air reflectivity estimated from in situ refractivity data obtained with an airborne refractometer, and that remotely measured with a ground-based radar observing the clear marine air boundary layer during daytime periods of strong mixing gave Z_e values about -5 dBZ_e (Doviak and Berger, 1980) which are practically the largest ones that might be expected from refractivity index irregularities (see Doviak and Zrnic', 1984, Fig. 11.17). Now considering the large scatter of velocity estimates, we have found that standard deviation of the spatial fluctuations, from V_6 to V_6, of the mean Doppler velocity in each V_6 is larger than 2 m s^{-1}, whereas estimated standard

*The subscript 6 refers to the -6 dB surface circumscribing the volume of space within which the target cross sections are weighted by factors larger than 1/4.

deviation, based on observed signal-to-noise ratios (SNR in dB $\simeq$ 15 dB) and spectral widths ($\sigma_v \simeq 6$ m s^{-1}), should be less than 1 m s^{-1} (Doviak and Zrnic', 1984, Chapter 6). Thus evidence suggests that insects or other fast, but randomly moving targets responsive to the wave are responsible for the unusually large reflectivity and large standard error of mean Doppler velocity estimates, and that they descend in response to being lifted by the wave. Furthermore, the reflectivity was 10 dB lower after the wave had passed than before the wave's arrival, further suggesting that targets have descended in response to the action of the wave.

3.4.2.2. Effective beam height

In order to relate tower and radar measurements we need an estimate of beam height at the range r to the wave peak at 2245. But this determination is complicated by the intense vertical gradients of reflectivity and refractive index. The temperature and moisture profiles in the inversion layer are such that below 500 m the gradient of refractive index is nearly zero, and in a layer between 500 m and 700 m it is -2.3 x 10^{-4} km^{-1}. Applying the equations developed in Chapter 2 of Doviak and Zrnic's text (1984) we determined that rays at elevation angles less than 0.3° will be totally reflected, but straight, below 500 m. Thus a significant fraction of the beam energy, in the 0.8° width of the beam, directed at elevation angles of 0.4°, could be trapped in the inversion layer. Thus not only is the gravity wave energy trapped by the inversion, but so is the energy of the electromagnetic wave. However, because the lower portions of the beam are blocked by nearby obstacles (e.g., buildings, trees) for rays below 0.2°, the amount of microwave energy likely to be trapped is expected to be small compared with the energy that will remain in the beam above the inversion. Furthermore the resolution volumes V_6

at short ranges ($\lesssim$50 km) and at low elevation angles (0.4°) remain mostly below the reflecting layer, so its effect should be negligible at these short ranges. However, electromagnetic wave trapping might account for the unusually long range ($\simeq$ 120 km, see Fig. 1 of Rust and Doviak, 1982) to which the solitary wave is observed. That is, if electromagnetic waves propagated along straight lines, V_6 would probably be well above the solitary wave at 120 km ranges.

If refractive index gradients are ignored, computation of the straight ray path, launched at an elevation angle of 0.4°, places the beam center height in the solitary wave at about 550 m above ground at the range of 50 km. However, reflectivity data acquired at shorter ranges with higher resolution show that reflectivity decreases exponentially with height and that there is at least a 15-dB change across the 3-dB beamwidth at the 50-km range. This suggests that the targets that contribute to the mean Doppler velocity in each of the resolution volumes, having a range extent of 150 m and spaced 180 m apart, are principally from regions below 550 m. On the other hand, because the lower portion of the beam is blocked, the effective beam height, for homogeneous reflectivity fields, would be shifted to altitudes higher than 550 m. It is rather difficult, using electromagnetic theory, to obtain a precise estimate of the effective beam height at the wave location, so we have resorted to another approach.

Effective beam height h_e is obtained by relating our best estimate of the radial component of wind (i.e., from Fig. 2, using tower data at low altitudes and radar data at higher altitudes where the wind should be negligibly deleterious to the radar beam) to the measured radial component V_{ro} (Fig. 12) in the ambient air, at the approximate range $r \simeq r_p - 6$ km, just in advance of the wave where r_p is the range to the wave peak. Figure 13 shows the

WIND HODOGRAPH
11 MAY 1980
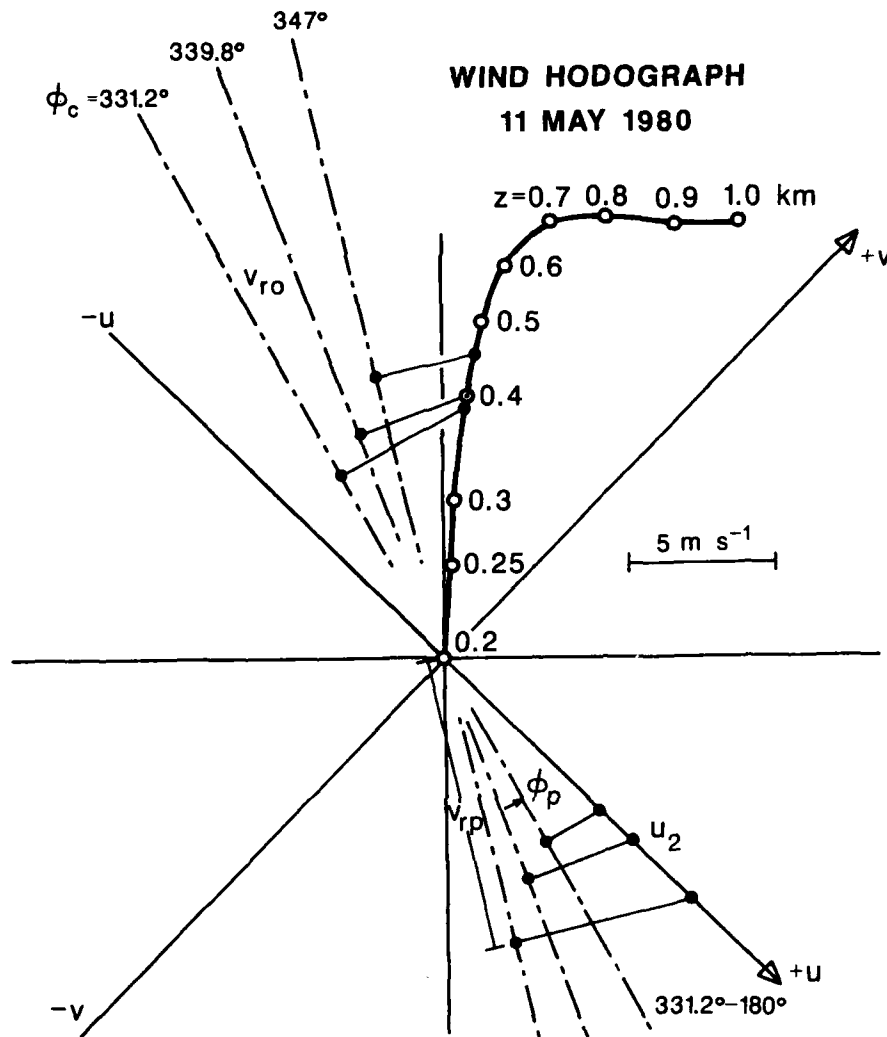
Figure 13. Hodograph of the ambient wind $\vec{V}_o(z)$ obtained from tower and radar data. The dots on the three azimuths ϕ_c give the measured radial component v_{ro} of the ambient wind preceding the wave. The angle ϕ_p is between the radar beam direction minus 180° and the south-east direction; v_{rp} is the measured peak radial velocity perturbation.

hodograph of the wind obtained from Fig. 2, and the three radial components V_{ro} (at three azimuths) from which we deduce h_e at r_p. The perpendicular

-82-

projection of V_{ro}, at each ϕ_c, onto the hodograph gives the estimate of h_e. These parameters are listed in Table 3.2. The height h_c, listed for reference, is the beam center height at r_p if gradients of reflectivity and refractive index and blockage were ignored. Thus some lowering of beam height is caused by the observed gradients.

Table 3.2. Wave characteristics along the front.

ϕ_c	v_{ro}	r_p	h_c	h_e	$u_o(h_e)$	v_{rp}	$u_2(0,h_e)$	ϕ_F	$\ell_{1/2}$	t_e
(Deg)	(m s^{-1})	(km)	(m)	(m)	(m s^{-1})	(m s^{-1})	(m s^{-1})	(Deg)	(km)	(CST)
331.2	7.1	46.8	500	430	6.1	-7.0	7.3	41	3.2	225630
339.8	8.0	50.3	550	440	6.3	-8.0	8.8	38	3.1	225030
347.0	9.8	56.2	640	500	7.0	-10.0	11.8	32	3.2	224330
TOWER	---	---	---	444	---	---	6.4	--	3.2	2311

h_e	= effective height of beam at range r_p
h_c	= beam center height at r_p, assuming straight line propagation paths
r_p	= range to wave peak
v_{ro}	= Doppler velocity of the ambient wind
ϕ_c	= azimuth of the Doppler data sector
v_{rp}	= radial velocity at the wave peak
$u_2(0,h_e)$	= amplitude of the wave's horizontal velocity
t_e	= equivalent time along wave front (see Sec. 3.4.4)
u_o	= ambient wind at height h_e
ϕ_F	= azimuth of a line tangent to the front (Fig. 5a)
$\ell_{1/2}$	= wave width at half amplitude

3.4.3. Estimates of wave amplitude and half width

Because momentum of the ambient environment is nearly zero below 200-m altitudes, and because it is lifted by the wave to the 400- to 500-m altitudes of the beam, $u_0 - \Delta u_0 \simeq v_0 - \Delta v_0 \simeq 0$ at the wave peak. Trapped outflow reaches the beam but its velocity v_{t0} is likely to be less than a few meters per second at the heights where it intersects the beam (see Fig. 6b). Furthermore, because the beam direction is northwesterly, the weight that v_{t0} gives to the Doppler velocity v_r is less than that received from u_2. Thus we shall ignore its contribution to v_r so that the observed peak Doppler velocity v_{rp} (see Figs. 12, 13) equals approximately the projection of the amplitude of the horizontal velocity $u_2(0, h_e)$ onto the beam direction. This estimate of $u_2(0, h_e)$ along each of the azimuth sectors is tabulated in Table 3.2.

The half-amplitude width $\ell_{1/2}$ (Fig. 1) is much more difficult to estimate because the waveform $v_r(r, z)$ is a complicated function of the streamline's vertical displacement $\delta(r, \eta)$, the ambient wind profile $u_0(z)$, $v_0(z)$, and the waveform $u_2(r, z)$. If the wave is weakly nonlinear, u_2 should have the $\tilde{x}$ dependence given by Eq. (2.30). However, the waveforms of $u_2(\tilde{x}, z)$ observed (Fig. 6a) at the tower do not fit precisely the form given by Eq. (2.30) but instead exhibit, especially at lower altitudes, crests that are more rounded and sides that are steeper. These differences are probably a result of the trapped outflow and large amplitude of the observed wave. Indeed Tung et al. (1982) showed numerically simulated solitary waves of permanent form having shapes similar to the shape observed on Fig. 6. However, these simulated waves were generated in a somewhat shallow fluid of total depth 4 times the stratification scale h_s and it is suspected that the boundary might also modify the waveshape from that expected when the boundary is infinitely far away.

-84-

Rather than trying to deduce an analytic formula for $v_r(r,z)$ from which we can estimate $\ell_{1/2}$, we can use observations to deduce the approximate waveform of $v_r(r,z)$. Since the inferred $u_0 + \Delta u_0$ waveform at the tower follows somewhat closely the leading and trailing edges of the observed waveform and then abruptly becomes constant at a value of zero during most of the wave period when u_2 has appreciable value, we assume during the radar observations that the u waveform has similar characteristics. Certainly evidence shows that the wave has larger amplitude earlier, and hence zero momentum air from low altitudes would be brought to even higher heights than 444 m. So we should expect that $u_0 + \Delta u_0 \simeq 0$ for much of the wave period during the radar observations. Thus, $\ell_{1/2}$ can be estimated from Fig. 12, assuming that the 2-D wave is, for the most part, depicted by the negative portion of $v_r(r)$. Thus from the geometrical arrangement of the sectors centered at azimuth ϕ_c, and the orientation of the wavefronts (Fig. 5a), we determine that

$$\ell_{1/2} = \ell_r \frac{\sin(\phi_F - \phi_c)}{\sin(135 - \phi_F)} \tag{3.10}$$

where ℓ_r is the half-amplitude width, deduced from Fig. 12, along the azimuth ϕ_c, and ϕ_F is the azimuth of the solitary wave front at its intersection with the radar beam. Values of $\ell_{1/2}$ and ϕ_F are tabulated in Table 3.2 showing that the wave width is relatively constant along the front whereas wave amplitude shows significant decrease away from the source. Comparing these values for $\ell_{1/2}$ with the values obtained at the tower (Fig. 8) we see that they agree with the half width measured at the 444 m tower level. The anomalously larger values of $\ell_{1/2}$ for heights below 444 m are assumed to be caused by the trapped outflow which, because of its higher density, might cause the wave to be broader at the lower altitudes. Thus, we assume that $\ell_{1/2} \simeq 3.2$ km roughly

represents the half-amplitude width of the wave. However, because tower data do not show $\ell_{1/2}$ to be constant with height as theory indicates, we don't have complete confidence that this estimate is appropriate for substitution into formulas of nonlinear wave theory to derive other wave properties (e.g., wave speed) to compare with observations.

3.4.4. Time dependence of wave amplitude--comparison of radar and tower data

Wave amplitude is not nearly so constant as wave width so to compare tower and radar observations further we assume that points along the wavefront farther from the storm correspond to older portions of the wave. Thus we can compare wave amplitude observed at the tower with those amplitudes observed by radar at 2245. An equivalent time scale along the wavefront can be deduced by noting that the wave source propagates, in the moving ambient air, at a uniform speed $|\vec{V}_s'|$ of about 23.6 m s^{-1} in the direction $\phi_s' = 80.7°$, and by assuming that elements of the wavefront travel along straight rays in a southeast direction (135°) as inferred in Section 3.3.2. Then it can be shown, by constructing a tangent line to the wavefront, that

$$dt_e = \frac{d\ell}{V_s^r} \frac{\sin(135-\phi_F)}{\sin(135-\phi_s')} \tag{3.11}$$

where $d\ell$ is the element of distance along the front, measured relative to the point where the ray intersects the front at 224530, and dt_e is the equivalent increment in time. Then dt_e is relative to 224530, which is the time the radar observes the peak of the wave front element that passes through the tower about 25 minutes later. Since ϕ_F is nearly a constant equal to about 34° at the intersection of the front with the radials at ϕ_c, we deduce the

equivalent times t_e listed in Table 3.2. The amplitude $u_2(0,444)$ of the wave at 2211 is 6.4 m s^{-1} and this is also listed in Table 3.2 because the 444-m tower level is nearest h_e for all three radials. To better compare wave amplitudes we have plotted $u_2(0,h_e)$ on Fig. 14 to show that the wave amplitude decreases with time, losing about half its value (or 75% of its energy) in less than 30 minutes. Although we don't have radar data for the time when the wave passes the tower, this figure and Table 3.2 show that the radar and tower observations of u_2 and $\ell_{1/2}$ suggest that wave amplitude is nearly constant after 2300, consistent with the observation that c is nearly constant after this time.
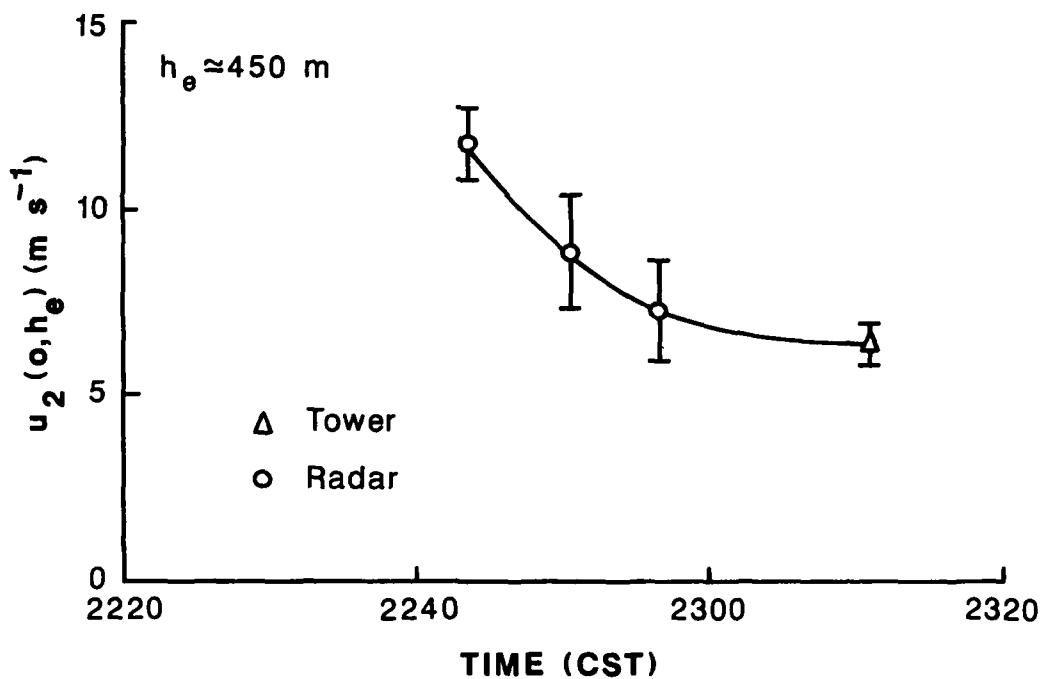

Figure 14. The solitary wave's horizontal velocity amplitude, $u_2(0,h_e)$, at about 450 m AGL versus time.

3.5. Comparison with Weakly Nonlinear Theory

Because wave amplitude and speed change with time, we obviously don't have a wave of permanent form, and thus comparisons with theory for steady waves are open to criticism. Nevertheless, we will compare observed wave characteristics with those deduced from the weakly nonlinear theory, presented in Section 2.3, to determine whether the observed wave characteristics might adjust, as energy is lost, in such a way as to be in accord with this theory for steady waves. For example, theory shows that waves of permanent form have speeds that increase with amplitude. Thus the decrease of speed and amplitude with time observed here (i.e., Figs. 7 and 14) is consistent with this theoretical expectation. Although evidence of trapped outflow suggests that the wave might be strongly nonlinear, it is instructive to compare observations with weakly nonlinear theory. We compare results with numerical solutions for strongly nonlinear waves in Section 3.6.

3.5.1. Comparison of wave speed and amplitude

Using Eq. (3.1a) we find that the Brunt-Väisälä frequency squared is

$$N^2(z) = N^2(o)\exp(-bz) \qquad\qquad 0 < z < 1.14 \text{ km} \qquad (3.12)$$

where $N^2(o) = 1.32 \times 10^{-3} \text{ s}^{-2}$ (i.e., the oscillation period is about 28 seconds) and $b = 2.86 \text{ km}^{-1}$. Thus the eigenvalue equation (i.e., Eq. (2.12e)), becomes

$$\phi'' + \frac{N^2(o)}{c_o^2} e^{-bz} \phi = 0. \qquad (3.13)$$

-88-

If Eq. (2.44) is taken as the first-order approximation to the exact solution, we need the average of $N^2(z)$ over the depth h of the inversion. This average is

$$\overline{N^2} = \frac{N^2(o)}{h} \int_0^h e^{-bz} \, dz = 3.75 \times 10^{-4} \, s^{-2}. \qquad (3.14)$$

Using Eq. (2.45b), the linear wave speed c_0 (i.e., the speed for waves of infinitesimally small amplitude) is computed, to first order, to be

$$c_0 \simeq c_{01} = 14.1 \, m \, s^{-1}. \qquad (3.15a)$$

This is a rather crude estimate because $N^2(z)$ does change considerably in the interval 0 to h. Hence in Appendix B we have employed an iterative technique to derive analytical equations for the eigenfunction ϕ from which we derived the estimates

$$c_0 \simeq c_{02} = 9.6 \, m \, s^{-1} \qquad (B.7b)$$

$$\alpha \simeq \alpha_2 = 2.4 \times 10^{-3} \, m^{-1} \qquad (B.12a)$$

$$\beta \simeq \beta_2 = 3.5 \times 10^3 \, m^2 \, s^{-1} \qquad (B.12b)$$

in which the subscript "2" denotes the second-order approximations. We have also presented, in Appendix B, a numerical solution of Eq. (3.13) and this compares well with the iterative one. For example, the numerically estimated linear wave speed is

$$c_0 = 9.9 \text{ m s}^{-1}, \qquad (B.10)$$

in close agreement with the second-order estimate.

The wave speed c is computed by substituting values of c_0 and β from Eqs. (B.10) and (B.12b) into Eq. (2.33f), using the experimentally derived estimate of 1.6×10^3 m for $\lambda = 0.5 \, \ell_{1/2}$ in this latter equation. Thus the theoretically estimated wave speed is

$$c = 12.1 \text{ m s}^{-1}, \qquad (3.15b)$$

in surprisingly good agreement with the observed speed of 12 m s^{-1} relative to the ground. This close agreement is fortuitous because the ambient air moves relative to the ground and because, as we will shortly show, the wave is not weakly nonlinear.

Nevertheless, using Eqs. (2.33a,e,f, and g) we can show that

$$c' = c = c_0 + \frac{\alpha \, u_2(o,z)}{4 \, \phi'(z)}, \qquad (3.15c)$$

which is the wave speed in still media. So given radar or tower anemometer measurements of $u_2(o,z)$ versus time, as for example those shown in Fig. 14, we can estimate c' vs. time. Substituting Eqs. (B.12a and b) for α and β, and using $\phi'(z)$ given by Eq. (B.11), we plotted the theoretically estimated c' versus time onto Fig. 11 (i.e., dashed line). We see that wave speed given by weakly nonlinear theory is slightly less than that observed, and both data and theory show similar decreases as time increases. Moreover, theoretical estimates are within the uncertainty of measurement.

We next turn our attention to comparison of the horizontal velocity $u_2(\tilde{x},z)$ computed from theory, and that observed by Doppler radar at 224530,

and tower instruments 25 minutes later. The maximum value, or wave amplitude, $u_2(o,z)$, is obtained from Eqs. (2.33a and e) which give, at $\tilde{x}=0$,

$$u_2(o,z) = \varepsilon \psi_0 \phi'(z) \qquad (3.16)$$

for heights z below 1.14 km.

ψ_0 is obtained by solving Eq. (2.28b), in which $\lambda_s \equiv h_s$; substituting this solution into Eq. (3.16) we obtain the equation

$$u_2(o,z) = \frac{4\beta}{\alpha\lambda} \phi'(z) \qquad (3.17)$$

which relates the eigenfunction $\phi(z)$ and parameters α, β of the stratified layer to u_2. Then $u_2(x,z)$ can be estimated if λ is known. Substituting our second-order estimates of α, β and ϕ' (Appendix B), and our experimentally derived estimate of λ into Eq. (3.17), we find that

$$u_2(o,z) = 3.65\left\{-0.17 + e^{-z/0.35}\left[4.55\sin\left(\frac{\pi z}{2.28}\right) + 2.18\cos\left(\frac{\pi z}{2.28}\right)\right]\right\} \text{ m s}^{-1} \quad (3.18)$$

where z is in kilometers. At z=0, where the wave amplitude should be largest, Eq. (3.18) gives

$$u_2(o,o) = 7.3 \text{ m s}^{-1}, \qquad (3.19)$$

which compares very well with the observed value of 7 m s^{-1} (see Fig. 8). Again we have near agreement of theory and experiment!

The agreement of the theoretically estimated wave amplitude $u_2(o,o)$ and that observed is obviously fortuitous because the wave amplitude at z=100 m is

nearly 12 m s^{-1} (Fig. 8), whereas theory stipulates that wave amplitude decreases with height! Furthermore, we infer from Fig. 8 that $u_2(o,o)$ is likely to be 13 m s^{-1}, almost twice the amount indicated by theory. Radar data (Table 3.2) show that $u_2(0,450 \text{ m}) \gtrsim 7$ m s^{-1}, whereas Eq. (3.18) produces a value of about 4 m s^{-1} at z=450 m, about half that observed! Finally, weakly nonlinear theory indicates that waves of permanent form must have amplitudes that are inversely dependent upon wave width λ (i.e., Eq. 2.42e), but Fig. 14 shows that amplitude decreases by a factor of 2, whereas wave width λ is nearly constant (Table 3.2).

We attribute these large discrepancies to the premise that the wave is strongly nonlinear, and thus we need to resort to higher order approximations (i.e., use second-order and higher terms in Eq. (2.8a)) or, in what might be a more profitable approach, to employ numerical methods that should produce results in complete accord with observations. These numerical methods will be developed and reported on in a subsequent report in which the effects of wind shear will also be accounted for.

The surprisingly good agreement betweem theoretical estimates and observed wave speeds and wave amplitude at the surface clearly demonstrates that, if measurements near the ground were the only ones available, we could realize excellent agreement between theory and observations (e.g., wave speeds within 0.1 m s^{-1} and amplitudes within 0.4 m s^{-1}) but for the wrong reasons. Only because we had radar and tower observations well above the ground were we able to infer that this agreement was anomalous and that the wave was strongly nonlinear.

3.5.2. Simplified strongly nonlinear theory to estimate amplitude

Although we shall not elaborate a theory of strongly nonlinear waves, we can still estimate theoretically some of the velocities to be expected in these waves, and these can be compared with measurements. For example, the fact that air appears to recirculate in the wave leads us to conclude that, within this portion of the wave, there must be a stagnation region at height z_0, where the trapped outflow does not move relative to the wave. Therefore, the air in this region must translate over the ground at the ground-relative wave speed c. Then, after turbulence and K-H waves are filtered from the observed u data, the peak perturbation in the u component of velocity should be

$$u_2(o,z_0) + \Delta u_0(z_0) = c - u_0(z_0). \tag{3.20}$$

When the wave passes the tower, a peak perturbation velocity of about 12.8 m s^{-1} occurs at the 176-m height (Fig. 6a), which is within the interval 100-200 m where we expect the altitude of stagnation to lie. Since in this height interval $u_0 \simeq -1$ m s^{-1}, we then infer from Eq. (3.20), after inserting c=12 m s^{-1} from Fig. 7 and $\Delta u_0 = +1$ m s^{-1}, that the peak wave velocity $u_2(o,z_0)$ is 12 m s^{-1}, in excellent agreement with the extrapolated observed value seen in Fig. 8.

Let us now extend these ideas on strongly nonlinear waves to the radar observations at 224530, when the wave had a speed c of about 13.3 m s^{-1} (Table 3.1) along the path passing through the tower, and the beam was at an effective height of about 475 m (Table 3.2). From Fig. 2a we find that $u_0(4.75) \simeq -7$ m s^{-1} and thus

$$c - u_0 \simeq 20 \text{ m s}^{-1}. \tag{3.21}$$

Because the path is about midway between the true azimuths, 340° and 347°, we deduce from Fig. 12 that $u_2 + \Delta u_0 \simeq 18$ m s^{-1}, about 2 m s^{-1} less than that estimated from Eq. (3.21). Of course an equality could be obtained only if the stagnation height was at 475 m. Because the wave was stronger at 224530 than it was at 2211, when it passed the tower, we expect the stagnation level z_0 to be higher than the 100-200 m deduced for the later time. However, whether z_0 has reached the beam height is in doubt, but the lower observed velocity (18 vs. 20 m s^{-1}) suggests that the beam is still above z_0.

Thus, using simplified arguments for strongly nonlinear waves, we are able to explain the observed wave amplitudes.

3.5.3. Comparison of waveforms

To determine the functional form of $u_2(\tilde{x},z)$, data obtained from Fig. 6a for each minute of observation at the 266- and 444-m heights on the tower are plotted onto Fig. 15. Also plotted in this figure are the theoretical waveforms (solid lines) obtained from Eqs. (2.33a and e) in which $u_2(o,h)$ is normalized to fit the data. The half amplitude width $t_{1/2}$ when multiplied by c ($\simeq 12$ m s^{-1} when the wave passes the tower) gives $\ell_{1/2}$, which is plotted in Fig. 8. We notice that the wind at 444 m AGL fits, reasonably well, the theoretical waveform, although the data suggest a faster decrease of u_2 at the extremities of the wave. Chen (1985, Fig. 7) compared vertical wave velocities with those determined by theory, and found very good agreement at all heights.

At the height of 266 m (and also at lower heights) $u_2(t)$ data show the wave crest to be more rounded and the sides to be steeper than indicated by theory. This could be anticipated because the numerical results of Tung et al. (1982) show that strongly nonlinear waves do have more rounded crests and steeper sides. Furthermore, Cummins and Le Blond (1984) compared

-94-

(a)

z=444m

$$\frac{u_{max}\, t_{1/2}^2}{4\, t^2 + t_{1/2}^2}$$

× DATA

VELOCITY u_2 (t,444) (m s^{-1})

$t_{1/2}$

TIME (CST)

(b)

z=266 m

VELOCITY u_2 (t,266) (m s^{-1})

$t_{1/2}$

TIME (CST)
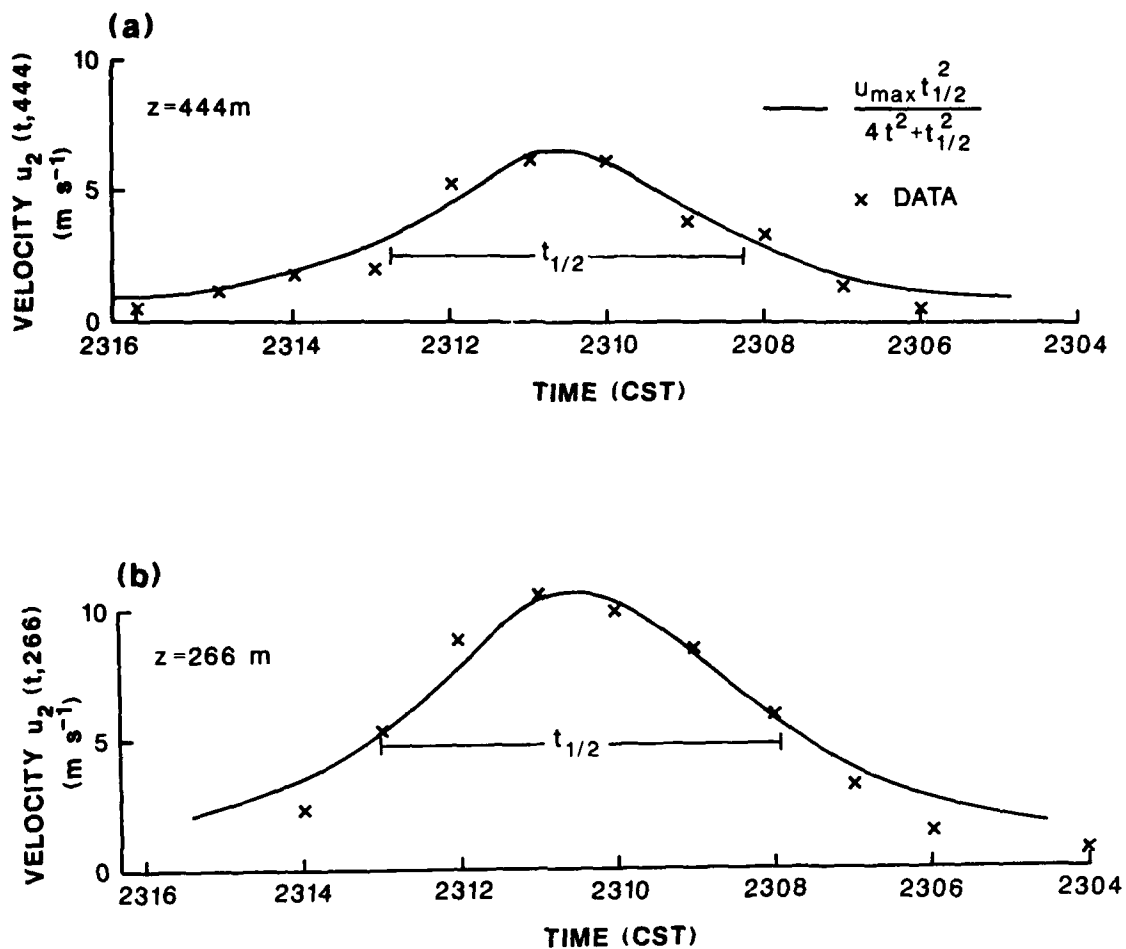
Figure 15. Comparison of the theoretical solitary waveform from weakly non-
linear theory (solid line), and the observed waveform (x) for
heights (a) 444 m and (b) 266 m. $t_{1/2}$ is the wave's half-width
(in time units) at half-amplitude.

waveforms of observed oceanic solitary waves with those shapes produced by

weakly nonlinear theories, and they also found in all cases, that the observed

waveforms exhibited more rounded crests and steeper sides. As in the case of

the atmospheric solitary wave examined herein, the oceanic waves had ampli-

tudes that violated weakly nonlinear assumptions. Therefore the departure of

the observed waveform from that given by weakly nonlinear theory might be

explained by the large amplitude of the observed wave. On the other hand, Tung's numerical results were given for fluid depths 4 times the vertical scale of stratification, and certainly the ocean is not infinitely deep. Consequently the finiteness of the fluid depth, and the nearness of the upper boundary to the lower one, might also have influenced the shape of the wave. To summarize, although the observed waveform and wave speed agree well with those stipulated by weakly nonlinear theory, wave amplitudes differ markedly.

3.5.4. Attenuation due to the vertical propagation of gravity waves

When the upper layer is stratified, as in this case (Fig. 2), waves can propagate vertically, thus robbing the solitary wave of its energy. Figure 14 shows that wave amplitude decreases as a function of time and we now estimate whether vertically propagating gravity waves can account for this attenuation. The solitary wave packet contains a continuum of spectral components with wavelengths ranging from extremely long (compared to λ) to those shorter than h_s. The stratified upper layer can support propagation of the long wavelength components which carry away energy from the solitary wave.

Maslowe and Redekopp (1980) have estimated the rate at which the stream function amplitude ψ_0 will decrease when the upper layer is weakly stratified with a Brunt-Väisälä frequency N_∞. Adapting their theoretical formulations we can show that the equation controlling the horizontal velocity perturbation $u_2(o,z,t)$, in the inversion layer, is

$$\frac{du_2(o,z,t)}{dt} = -\frac{\gamma u_2^2(o,z,t)}{\phi'(z)}, \qquad 0 < z < h \qquad (3.22a)$$

where

$$\gamma = \frac{\alpha\lambda}{h_2^2} \left(\frac{\lambda N_\infty}{c_0}\right)^3 f(\beta), \qquad (3.22b)$$

$$f(\beta) = \frac{1}{3} - \frac{\pi}{2\beta} \left[I_2(\beta) - L_2(\beta) \right], \qquad (3.22c)$$

$$\beta = \frac{2\lambda N_\infty}{c_0}, \qquad (3.22d)$$

and I_2, L_2 are modified Bessel and Struve functions of second-order (Abramowitz and Stegun, 1968). The solution of Eq. (3.22a) is

$$u_2(o,z,t) = \frac{u_2(o,z,t_0)}{1 + \gamma u_2(o,z,t_0)(t-t_0)/\phi'(z)} \qquad (3.23)$$

where t_0 is a reference time. Substituting $\lambda = 1.6 \times 10^3$ m, Eq. (B.12a) for α, Eq. (B.10) for c_0, and the estimate $h_s = b^{-1} = 350$ m into the above we obtain

$$\beta = 2.26,$$

$$f(\beta) = 0.1,$$

$$\gamma = 4.54 \times 10^{-6} \text{ m}^{-2}.$$

From Fig. 14 we determine that, for $z = 450$ m, $u_2(o,450,t_0) = 11.8$ m s^{-1} at $t_0 = 224330$. Substituting this value and γ into Eq. (3.23), and using Eq. (B.11) to evaluate $\phi'(450)$, we estimate u_2 at the next data time (225030) to be 0.5 m s^{-1}, considerably less than the 8.8 m s^{-1} observed at that time! Accepting the theory we need to explain why the wave lasted as long as it did.

Perhaps an elevated inversion layer may have reflected energy back to the ground (Crook, 1987). On this day an elevated inversion having a θ_{vo} change of 2 K in a layer of about 100 m thickness was observed at a height of 0.6 km AGL in the 1800 CST sounding. This elevated inversion increased in height to about 4.1 km in the sounding 12 h later. Assuming a linear increase in the inversion height during this interval, this inversion would be 3.2 km AGL at

the time of the solitary wave. Further numerical analyses would have to be performed to determine how much of the energy in the upward propagating gravity waves would be returned to the lower layer, and whether this return is sufficient to account for the slow decrease of the observed wave amplitude. On the other hand, wind curvature u_0'' could duct gravity wave energy (Chimonas and Hines, 1986; Crook, 1987).

3.6. Comparison with Numerical Results for Strongly Nonlinear Waves

Results presented in the preceding section support the view that the wave is strongly nonlinear. So we are naturally led to make comparisons with the numerical solutions for the case of large amplitude waves of permanent form. Tung et al. (1982) presented numerical results that relate stream function amplitude $\epsilon\psi_0 \equiv \psi_{max}$ to wave speed c' (wave speed in the coordinate frame advecting with the fluid) for fluids of various depths, the deepest of which was 40 times the scale of stratification h_s. However, Tung et al. (1982) solved for the strongly nonlinear wave characteristics for waves propagating in a medium in which the vertical profile of density change is described by a hyperbolic tangent function, whereas we have fitted θ_{vo} data with an exponential function. Nevertheless, the results should be similar, because the scales of stratification and net change in $N^2(z)$ should be the same since both the tanh and exponential functions fit the θ_{vo} data quite well (Fig. 3). The hyperbolic tangent function that fits the θ_{vo} data well is

$$\theta_{vo} = 294.4 \left(1 + 4.755 \times 10^{-2} \tanh sz\right) \tag{3.24}$$

where

$$s = 2.07 \times 10^{-3} \text{ m}^{-1}.$$

We have taken from Tung et al. (1982; Fig. 14, H=40) their numerically evaluated normalized stream function amplitude $(\psi_{max}/c'h_s)$ values and replotted them onto Fig. 16, except that we use a wave speed c' normalized to the linear wave speed c_0 for the hyperbolic tangent profile. Then, interestingly, the strongly nonlinear wave speed shows a linear dependence versus normalized stream function amplitude. The linear dependence can be expressed as

$$\frac{c'}{c_0} \simeq \left(1 + 0.55 \frac{\psi_{max}}{c'h_s}\right). \qquad (3.25)$$
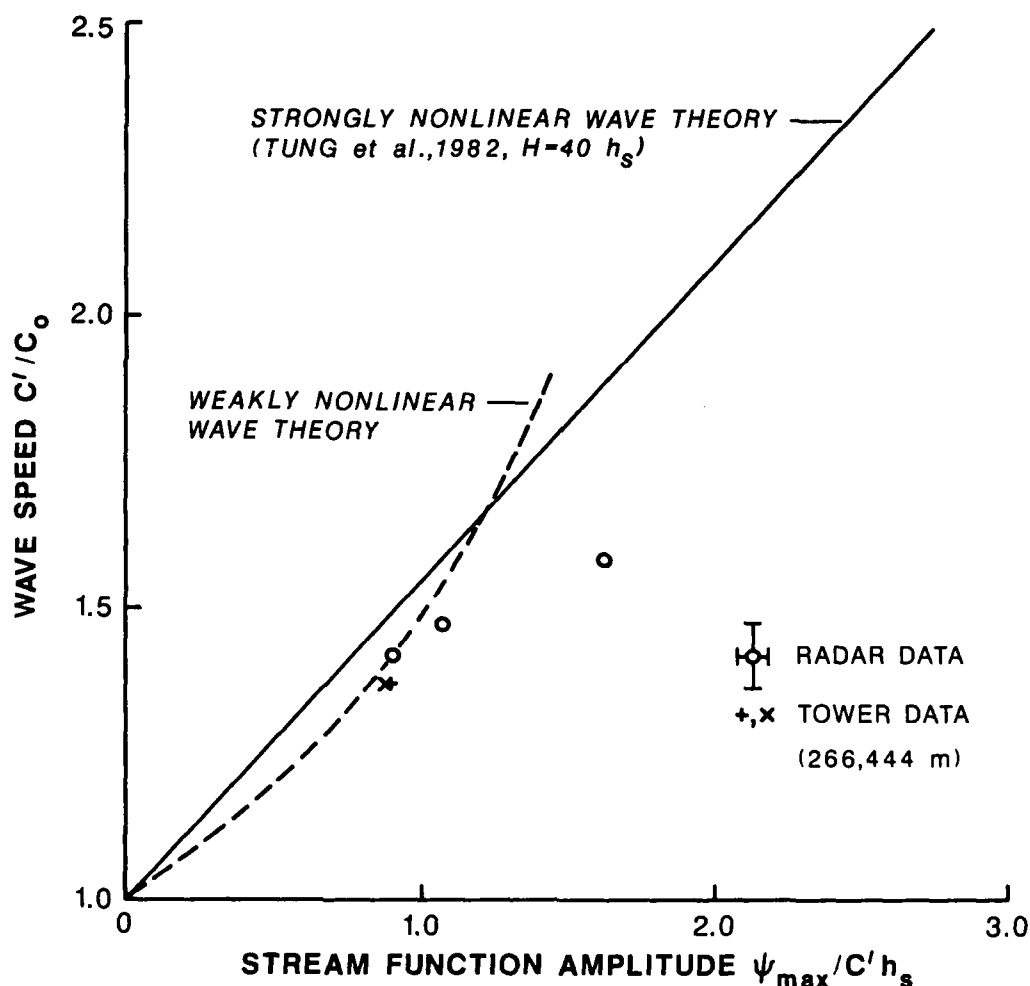
Figure 16. Normalized wave speed versus normalized stream function amplitude. c' is the wave speed relative to the ambient air, which advects in a northerly direction.

The scalings of the axes depend on how h_s is defined, and we use a definition slightly different from that used by Tung et al. Our definition, which we now develop, is based upon the comparison of analytical solutions of weakly non-linear theory with numerical ones for the limit point $\psi_{max} \to 0$.

To compare analytical and numerical results, as well as data, we can use Eqs. (2.33f and g) to obtain

$$\frac{\psi_{max}}{c'h_s} = \frac{4}{\alpha h_s}\left(1 - \frac{c_0}{c'}\right), \qquad (3.26)$$

which expresses the normalized stream function amplitude, for weakly nonlinear waves, in terms of wave speed. Now we can adapt the eigenfunction solutions given by Benjamin (1967) for a hyperbolic tangent profile of density stratification. Thus we find that

$$\phi = \tanh sz \qquad (3.27a)$$

and

$$K^2 = 2s^2, \qquad (3.27b)$$

which are the eigenfunction and eigenvalue $K^2 \equiv N^2(o)/c_0^2$ (see Appendix B) for the θ_{vo} profile given by Eq. (3.24). Tung et al.'s plotted numerical data suggest that $\phi_{max} \to 0$ when $c_{oo}^2/(c')^2 \approx 2.2$, where

$$c_{oo}^2 \equiv \frac{g \Delta\theta_{vo}h_s}{\theta_{vo}(o)} \qquad (3.28)$$

is a scaling velocity equal to the speed of a linear wave propagating in a medium composed of two homogeneous layers having a virtual potential temperature difference $\Delta\theta_{vo}$ equal to the total change in θ_{vo} across the upper half of the hyperbolic tangent profile (i.e., in our case, above the ground). Although Tung et al.'s numerical solution applies when a rigid boundary is

-100-

atop the upper layer at z=H=40 times 1/s, they did state that there is prac-
tically no difference between these results and those for the case in which
H=20 or 30 times 1/s. Accepting their solution as accurately representing the
situation of an infinitely deep upper layer, we conclude that when $\psi_{max} \to 0$,
$c' = c_{oo}/\sqrt{2.2}$. Thus, using Eq. (3.27b) and solving for c_0^2 in terms of c_{oo}^2
gives

$$c_0^2 = \frac{c_{oo}^2}{2sh_s},$$ (3.29)

and substituting this into Eq. (3.24), we obtain

$$\frac{\psi_{max}}{c'h_s} = \frac{4}{\alpha h_s} (1 - \frac{c_{oo}}{c'\sqrt{2sh_s}}).$$ (3.30)

Evaluating the α parameter for the hyperbolic tangent profile by substituting
Eq. (3.27a) into Eq. (2.40a), we find

$$\alpha = 1.2s.$$ (3.31)

We are now in a position to define h_s. Tung et al. (1982) speci-
fied $h_s \equiv 1/s$, in which case Eq. (3.30) becomes

$$\frac{\psi_{max}}{c'h_s} = \frac{10}{3} (1 - \frac{c_{oo}}{c'\sqrt{2}}).$$ (3.32)

However, Eq. (3.32) does not agree with strongly nonlinear analysis in the
limit $\psi_{max} \to 0$ because this analysis shows that $\psi_{max} \to 0$ at $c_{oo}^2/c^2 \simeq 2.2$ and
not at 2.0 as determined by Eq. (3.32). Furthermore, the data of Davis and
Acrivos (1967a) seems to suggest that $c_{oo}^2/(c')^2$ is larger than 2.0 when
$\phi_{max} \to 0$. This disparity between weakly and strongly nonlinear analysis can be
avoided if we define

$$h_s \equiv 1.1/s = 531 \text{ m}, \tag{3.33}$$

which is slightly larger than that obtained using Tung et al.'s definition.

In order to place our observations onto Fig. 16, we need to estimate ψ_{max}. But because we do not have $u_2(x,z)$ at various heights from radar observations, we can only roughly estimate ψ_{max}. To obtain an estimate we assume that, as wave amplitude increases, the stream function retains the same functional form suggested by nonlinear theory. This may not be a bad assumption in view of the good agreement between weakly nonlinear waveforms $u_2(\tilde{x},h)$ and the measured ones shown on Fig. 15, and because the $u_2(o,z)$ data for $z > 150$ m (Fig. 8) are consistent with the $u_2(o,z)$ (dashed line on Fig. 8) derived from the eigenfunction form based on weakly nonlinear theory. With this assumption we can estimate ψ_{max} from the $u_2(o,h_e)$ measurements made by radar and/or tower anemometers. The amplitude of the u wave component, obtained from Eqs. (2.33a and e), is,

$$u_2(o,h_e) = \left.\frac{\partial \psi}{\partial z}\right|_{h_e} = \psi_{max} \phi'(h_e), \tag{3.34}$$

where $\phi'(h_e)$ is $s \cdot \text{sech}^2(sh_e)$. Values of $u_2(o,h_e)$ and h_e, obtained from Table 3.2, are substituted into Eq. (3.34) to obtain ψ_{max} at the equivalent times t_e listed in the table. Corresponding to these t_e we obtain estimates of c' from Fig. 11, and these are normalized by the linear wavespeed $c_0 = 10.6$ m s^{-1} for waves propagating in the medium having the stratification given by Eq. (3.24). The data of normalized stream function amplitude is then plotted on Fig. 16. We have also added tower data at $h_e = 266$ m to see how well they agree with data at 444 m. In principle, since the tower data are collected at the same time, ψ_{max} should be the same at $h_e = 444$ m as it is at

266 m. Figure 16 shows that they are coincident. The error bars denote the uncertainties in $\psi_{max}/c'h_s$ and c'/c_0 because of the rms fluctuations of c' data about the fitted curve (Fig. 11). We see fair agreement between observations and strongly nonlinear theory. However, observations show wave speed to be consistently less than that given by theory. Perhaps we have underestimated the advection velocity of the ambient wind. An increase of 1 m s^{-1} would bring the cluster of four data points onto the line. On the other hand, it is possible that the cooler, denser, trapped air slows the wave. The numerical analysis of Tung et al. assumes the trapped fluid to have the same density as the ambient air.

Even though weakly nonlinear theory is strictly valid for $\psi_{max}/ch_s \ll 1$, it is of interest to determine how well this theory compares with that for large amplitude waves, as well as with data. So we have also plotted values of Eq. (3.26) onto Fig. 16, again assuming $h_s = 1.1/s$. It is surprising that weakly nonlinear theory agrees so well with numerical results, even for normalized amplitudes as large as 1.3 or, equivalently, for displacements δ_m as large as 1.3 times the scale of stratification!

We should not be led by these good agreements that weakly and strongly nonlinear theories are in complete accord for wave displacements as large as 1.3 h_s because we have not considered wave width. Nonlinear waves have wave amplitude, speed, and width that are all interdependent and, as we now show, the good agreement with respect to wave amplitude and speed does not extend to the wave's half-width, λ. We have plotted onto Fig. 17 λ (dashed line) computed from Eq. (2.33f). That is,

$$\lambda = \frac{\beta/c_0}{(c'/c_0)-1} = \frac{0.75s}{(c'/c_0)-1}, \qquad (3.35)$$

in which $\beta = 0.75\ c_0/s$ is obtained by substituting Eq. (3.27a) into

Eq. (2.40b). We also have plotted λ data from Table 3.2. Now we see large

differences between data and λ values obtained from weakly nonlinear theory.

For sake of completeness, we have also plotted values of λ obtained from the

strongly nonlinear analysis of Tung et al. for the case $H=4h_s$. Unfortunately,

Tung et al. did not present data for other values of H. However, they did

plot streamlines for few values of c/c_0 for the case H=40, and we have ex-

tracted rough estimates of λ from these figures. We found λ to be appreciably

larger than that for $H=4h_s$, so much so that theory for $H=40h_s$ seems to esti-

mate a λ significantly larger (by about 40%) than that observed! Because

our λ data lie between theoretical estimates for H=4 and $40h_s$, we conclude

that, in our observations, an effective upper boundary at which vertical ve-

locity is zero lies somewhere in the interval 2 to 20 km.
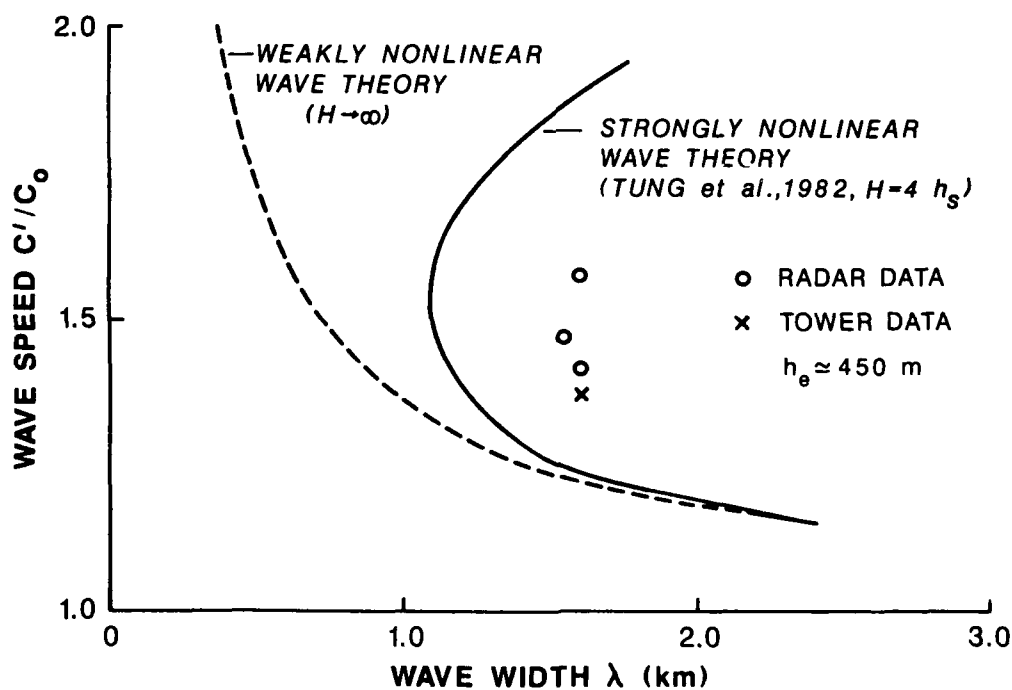
Figure 17. Normalized wave speed versus wave width.

Furthermore, we note that whereas weakly nonlinear theory gives λ monotonically decreasing with wave amplitude and/or wave speed, strongly nonlinear analysis shows that wave width reaches a minimum value, at which point recirculation appears, and thereafter further increases in amplitude cause increases of the wave's half-width. The relatively constant observed half-width indicates that the wave has recirculation within it, and we see that data fall within the speed range where strongly nonlinear theory suggest width to be nearly constant.

4.0. AVIATION WIND SHEAR HAZARD POTENTIAL OF THUNDERSTORM GENERATED GRAVITY WAVE PHENOMENA

The principal hazard of the much studied downbursts is not necessarily confined to the direct effects of downdrafts but, as Lee et al. (1978) pointed out, the aircraft, in passing beneath a downdraft, "experiences first a strong headwind, then roughly no horizontal wind at all as it enters the downflow area, and finally experiences a strong tailwind. These wind shifts from head-wind to tailwind, with a vector difference of 40 m s^{-1} or more in 4 km in the horizontal, may be more dangerous than the well-organized gust front." One of the earliest accidents that has been attributed to changes in headwind is that reported by Stewart (1958) who described a "microburst-type" wind shear event (Fig. 18) which downed a BOAC Argonaut on its take-off from the Kano Airport
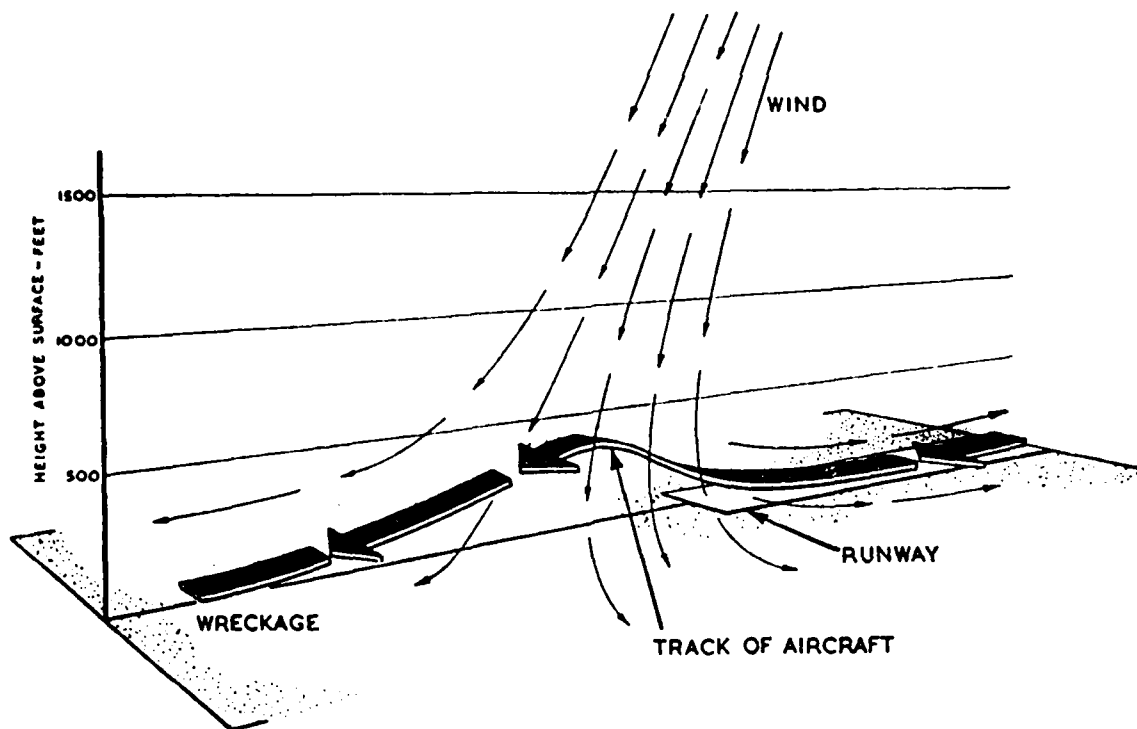

Figure 18. The unusual conditions which led to the Kano accident in 1956. The height indications are those of the accident investigation committee (from Stewart, 1958).

in Nigeria in June 1956. The investigating board concluded that "The accident was the result of the loss of height and airspeed caused by the aircraft encountering, at approximately 250 ft after take-off, an unpredictable thunderstorm cell which gave rise to a sudden reversal of wind direction, heavy rain, and possible downdraft condition."

Much of the earlier research on wind shear hazard focused attention to the gust front, which is often thought to be synonymous with the leading edge of gravity currents. However, it is now known that gust fronts and associated thin lines of reflectivity are observed at the leading edge of bores (Fulton, 1987) and solitary waves (Doviak and Ge, 1984) as well as gravity currents. In its simplest form the gravity current is a shallow layer of laminar flow having a leading edge that expands at a velocity dependent upon the depth of the current, and the difference in density (or temperature) of the ambient air, and that within the current (Von Karman, 1940). In this case, wind shear hazards are minimal because the aircraft would only experience a net increase in headwind. However, currents are not necessarily laminar, and they often have at their leading edge a mass of recirculating air (gravity current head) that is somewhat deeper than the current behind it, and it is this region of circulating flow that also generates a pattern of increasing and decreasing head or tailwind. Furthermore, it is the opinion of some (e.g., Linden and Simpson, 1985) that the wind shear at the leading edge of a radially expanding gravity current might be a more significant hazard than the change in head/ tailwind associated with the divergent flow of microburst. Support for this contention is given in the flight pattern of the aircraft "Delta Flight 191," which apparently flew across a microburst (Fig. 19). The recorded flight path and vertical velocity shows that the aircraft negotiated most of the microburst with no significant departure from the glide slope, but upon entering

-107-
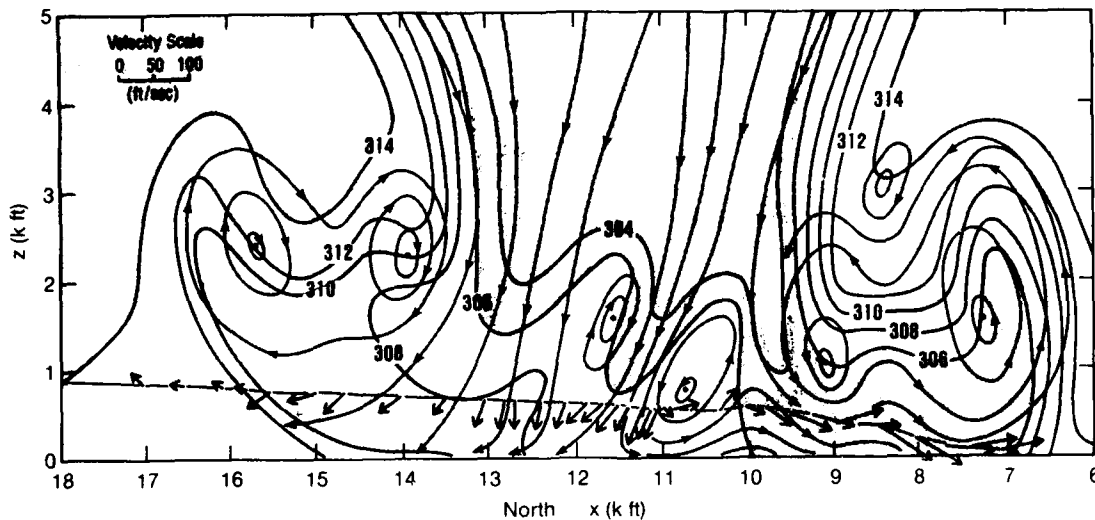
Figure 19a. A conceptual model of the vertical airflow structure in the DFW
microburst, based on the analysis of flight recorder data.
Shaded contours are potential temperature (K); arrowed lines are
streamlines. Arrows are wind vectors (see velocity scale).
Dashed line represents the aircraft track.

the region near the leading edge of the gravity current, strong wave-like per-
turbations, similar to those observed in undular bores emanating from gravity
currents (Fulton, 1987, Fig. 17), appeared to have caused the aircraft to
rapidly lose altitude.

Hazardous low-altitude shear has been associated with mountain lee waves,
sea breezes, cold frontal passages, and more recently, with large-amplitude
gravity wave disturbances. Gossard (1983) observed gravity waves that had
wind speed changes of as much as 20 m s^{-1} (40 kt) in a distance of 5 km
(3 mi). Gravity waves are seen to be evolving out of the leading edge of
thunderstorm-generated gravity currents (Fulton, 1987).

Although there is no documentation with conclusive evidence linking soli-
tary waves to crashes, there are accidents in which solitary waves cannot be
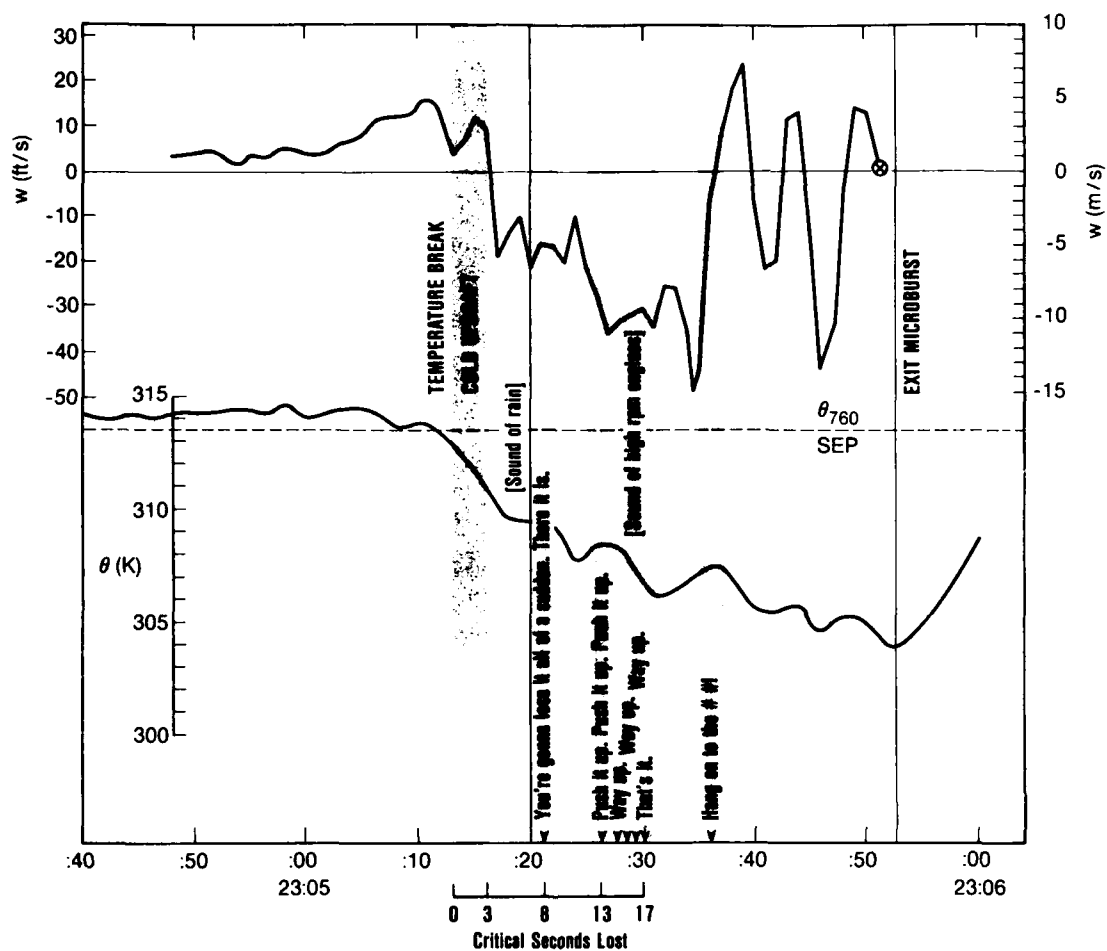
Figure 19b. A time series plot of vertical wind component (w) and static air
temperature (θ) from the Delta Flight 191 flight recorder to-
gether with comments from the flight crew that were recorded on
the cockpit voice recorder (from Caracena et al., 1986).

dismissed as the cause. One of the best documented aircraft crashes, where

wind shear in fair weather was identified as the cause, occurred in Bathurst,

New South Wales, Australia. In that case, investigators determined that the

aircraft experienced a 30 m s^{-1} (60 kt) airspeed change in less than 24 s

(Christie and Muirhead, 1985). Furthermore, a study by Anderson and Clark

shows that, of 43 meteorologically-related wind shear incidents in Australia,

only 16% could be attributed, with any certainty, to frontal and thunderstorm activity (Anderson and Clark, 1979 and 1983). Thus, considering the insidious nature of solitary waves and their frequency of occurrence, Christie and Muirhead inferred that it is reasonable to assume that many of the remaining incidents, and quite possibly some of the former, can be attributed to solitary wave activity in the first few hundred meters of the atmospheric boundary layer (Christie and Muirhead, 1983). It is to be emphasized that the horizontal wind shear associated with the wave is strongest near the ground where aircraft are most vulnerable.

The effect of a solitary wave on aircraft performance is complicated because it depends on the pilot's response to physical stimuli. Furthermore, the response depends on the direction of approach into the wave. For example, Fig. 20 reproduces the streamlines of a numerically modeled and an observed
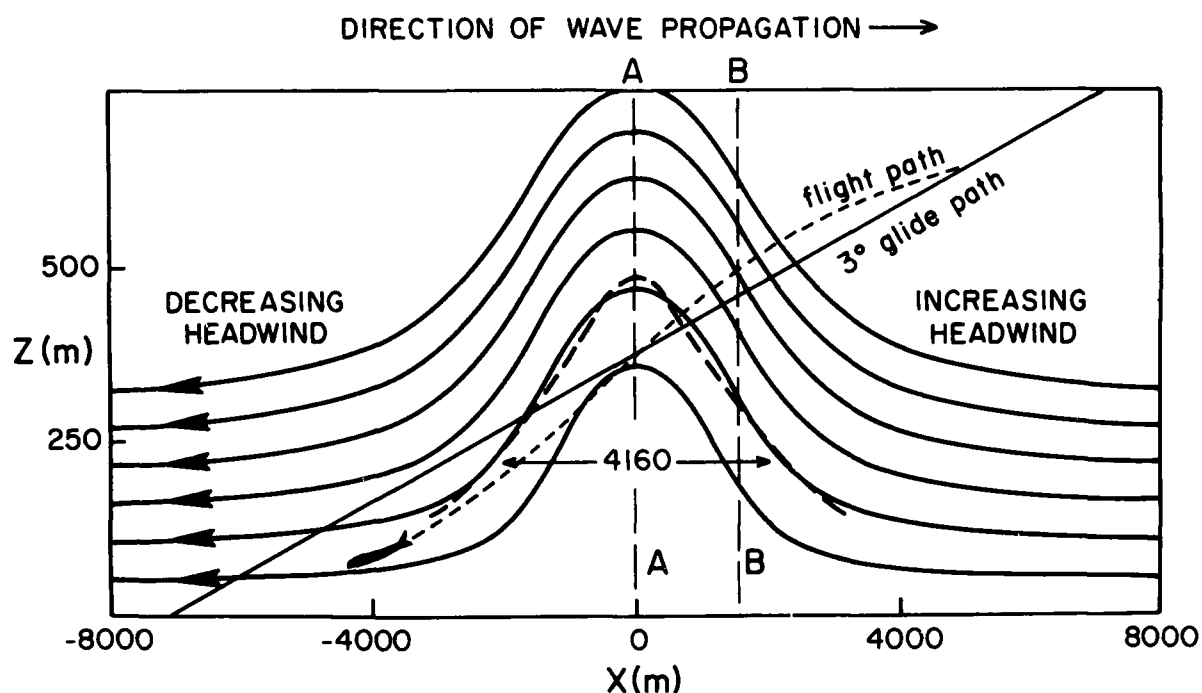

Figure 20.   Hypothetical flight path in a head-on encounter of a plane with a solitary wave. Solid waves are streamlines from a numerical model (Christie and Muirhead, 1982) and the dashed one is obtained from observation (Doviak and Ge, 1984).

solitary wave on which is superimposed a 3° glide path for an aircraft approaching the wave propagating towards it. The streamlines are drawn for the wind relative to a coordinate frame which moves with the wave. It can be deduced, for this case, that the aircraft would first experience an increase in headwind and updraft followed by a decrease in headwind and downdraft. The short-dashed line suggests the flight path that could result as a consequence of aircraft response to the effects of shear. For aircraft approaching from the opposite direction, the flight path would initially be below the glide path and then, if the aircraft is still airborne, above with the possibility that the aircraft would overshoot the runway.

The wind profile through a solitary wave differs from that encountered in a microburst because a single-crested solitary wave produces only an increase in headwind (or tailwind) and then decreases to the initial wind state, whereas the microburst generates both headwind and tailwind components. That is, the horizontal wind shift is unimodal in a solitary wave whereas it is bimodal in a microburst. However, a sequence of two or more waves is sometimes observed and can give the pilot the appearance of alternating headwind and tailwind components.

Although the observed solitary wave reported herein was 60 km (32 n mi) from the storm that apparently generated it, it still had significant horizontal and vertical shears (e.g., 4.4×10^{-3} s^{-1} and 60×10^{-3} s^{-1}) of the horizontal wind 90 m (300 ft) above the ground. The horizontal shear persisted over a distance of about 1500 m (i.e., $\simeq 3/4$ n mi). Short-wavelength waves, which developed atop this solitary wave, intensified the horizontal shear to 7.6×10^{-3} s^{-1} over a distance of 700 m (0.4 n mi). For a perspective on the significance of such shears on aircraft performance, note that a decrease in headwind along an imagined 3° glide slope through the solitary wave is larger

(38 kt or 19 m s^{-1}) than the one (35 kt or 17.5 m s^{-1}) that caused a 50-m (150 ft) drop in altitude of a 747 aircraft on its approach into Melbourne, Australia (Woodfield, 1983). Turbulence behind the wave possessed even stronger horizontal shears with wind changes as large as 6 m s^{-1} (12 kt) over a 130-m (400 ft) distance, or a shear value near 50 x 10^{-3} s^{-1}. An aircraft landing at a speed of 72 m s^{-1} (140 kt) could experience a 6.2 m s^{-1} (12 kt) headwind decrease in ~ 2 s. These large solitary wave shears were observed at the tall-tower site when the storm was 60 km away. At points closer to the storm the shear should be significantly larger. For example, the wave amplitude observed by Doppler radar at 2245 CST for locations 45 km from the storm's edge, was almost double that observed at the tower.

Christie and Muirhead (1983a,b) showed how an initially smooth long wave with relatively benign shear can evolve under the influence of nonlinearities and frequency dispersion into an amplitude-ordered family of solitary waves of large amplitude and short half-amplitude widths, in which shear is markedly increased. Their work suggests that the intense, transient shear zones generated with these waves constitute a serious hazard to the safety of flight at low altitudes.

Much effort in the research and development community is being expended to develop equipment and techniques to detect phenomena, such as microbursts, hazardous to safe flight. However, these phenomena are usually short-lived with lifetimes often less than 5 minutes, and thus their timely detection and communication of the potential threat they pose is extremely challenging. Doviak and Lee (1985) suggested that it is equally important to focus effort on the detection of the larger scale, more predictable phenomena that lead to the formation of these transient hazards, in addition to seeking methods to quickly detect and warn of the hazard itself. In this respect, the long life

of the solitary wave lends itself to easy, early detection by high-performance Doppler weather radars, if wave reflectivity is sufficiently intense.

It is remarkable that the storm outflow remained in the wave for distances of at least 60 km from the storm. Although storm outflows propagate as gravity currents to large distances, it is suggested that gravity waves, and in particular solitary waves formed by the interaction of the storm's downdraft with the stable layer, can transport the outflow faster and probably, with greater momentum, farther. Thus hazardous shear, normally confined to regions close to the storms, might indeed be found at large distances from them.

After observing laboratory simulations of radially diverging gravity currents, Linden and Simpson (1985) suggested that thunderstorm downdraft (microburst) hazards might also be linked to wind shear and vertical drafts of an intense rotor which forms at the gravity current front. The vorticity in the rotor increases to conserve angular momentum as the vortex tube is stretched. Near the source the intensification of vorticity was largest and produced a vortex that occupied almost the full depth of the gravity current to become nearly cut-off from the following flow.

To answer the question whether solitary waves pose a shear hazard to aircraft we reviewed the paper of Rudich who summarized the weather conditions leading to 33 weather-involved air carrier accidents that have been investigated and formally reported on by the National Transportation Safety Board for incidents that occurred during the period 1962-1984 (Rudich, 1986). In 11 cases fatalities occurred, and in 27 cases injuries and/or damage to the aircraft occurred in which wind shear may have been the cause, or the contributing cause, of the accident. In nine of the fatal cases (18 of the nonfatal ones) the aircraft either penetrated thunderstorm rain or was in the area of

thunderstorm rain. In one case the aircraft flew through heavy rain, but thunder was not reported. If thunderstorm generated waves were involved in these accidents they would likely be in their earliest stage of formation but, of course, it is at the time when waves might have the largest amplitude. For example, wave-like perturbations are seen in the outflow gravity current of the thunderstorm that caused the crash of Delta Flight 191 at the Dallas/Fort Worth International Airport on 2 August 1985 (Caracena et al., 1986). In only one fatal accident was wind shear noted as a possible cause without rain being mentioned, and therefore it is possible that waves might have been present. In two of the fatal cases, it was reported that the aircraft was near, or had entered a roll cloud that was out in advance of a squall line which produced moderate rain. The presence of a roll cloud is strong evidence for the existence of a horizontal rotor and the formation of a wave. In nine of the non-fatal accidents there were no reported thunderstorms in the vicinity of the accident, and thus it is possible that waves or wave-induced turbulence might have been the cause or a contributing factor of the accidents. Thus, waves might be implicated in 11 of the 33 investigated accidents.

5.0. SUMMARY AND CONCLUSIONS

To understand the interrelationships between the observed solitary wave parameters and ambient environment we have reviewed weakly nonlinear wave theory and made a detailed study of an observed solitary wave. Because the wave was propagating in a sheared environment, we have examined the governing equations for sheared ambient flow and have deduced that, for the observed ambient environment, the Taylor-Goldstein equation is the necessary eigenfunction equation to be solved. Analytic solutions to this equation are not easily obtained, especially for the vertical profiles of θ_{vo} and u_0 encountered in practice, so to derive an approximate one we have ignored the wind curvature term. Although this might first appear to be an oversimplification, the work of Tung et al. (1981) suggests that the solitary wave solution to the nonlinear evolution equation is unchanged by the presence of shear. Nevertheless, we found that shear had to be considered when computing the advection speed of the ambient environment, and also when estimating the wind perturbations caused by the wave vertically transporting horizontal momentum. Furthermore the upper boundary can exert an enormous influence on the wave speed (and probably the waveform), and thus its location may be of crucial importance in numerical models in which this boundary is usually placed, for practical reasons, at a finite distance above the layer of stratification. For example, when the upper boundary is infinitely far above the stratified layer, the wave speed is twice that when the boundary is at the top of the layer.

The thunderstorm that generated the solitary wave was traversing the medium at speeds ($\simeq 25$ m s^{-1}) that would be considered "supersonic" with respect to the solitary wave speed. Because large amplitude waves have amplitude-dependent speeds, and because the thunderstorm traversed an advecting atmosphere, we derived a modified Mach relation to compute wave speed from the

measured storm velocity and the convex shape of the wave front. This wave speed showed fairly good agreement with wave speeds computed from tracking wave front positions versus time along lines of energy propagation paths.

The surprisingly good agreement of observed wave speed and amplitude at the surface, compared with estimates from weakly nonlinear theory, clearly demonstrated that, if measurements near the ground were the only ones available, we could realize excellent agreement between theory and observation (i.e., wave speeds within 0.1 m s^{-1} and amplitudes within 0.4 m s^{-1}), but for the wrong reasons. Only because we had radar and tall tower measurements well above the ground were we able to infer that this agreement was anomalous and that the wave was strongly nonlinear.

We were then led to compare results of numerical solution for strongly nonlinear waves in a shearless environment. In spite of the fact that vertical shear was significant (i.e., $\simeq 10^{-2}$ s^{-1}) the observed wave characteristics agreed well with that estimated from theory when vertical transport of horizontal momentum and advection were accounted for. Although weakly nonlinear theory shows that wave amplitude δ_m must have an inverse relation to wave width $\ell_{1/2}$ in order for the waves to have permanent form, Tung et al. (1982) showed that large-amplitude waves with trapped circulation can have permanent form, but then the inverse relation between δ_m and $\ell_{1/2}$ is no longer valid.

The relationship between wave amplitude and wave speeds, given by weakly nonlinear theory, agree surprisingly well with both data and the theory for strongly nonlinear waves; even for peak wave displacements as large as 1.3 times the scale of stratification h_s (Fig. 16). However, this agreement does not extend to wave width $\ell_{1/2}$. The observed wave widths are much larger than those given by weakly nonlinear theory, but are in accord with the numerical results of Tung et al. (1982), who show that wave width reaches a minimum

value when recirculation appears within the wave at which instance the normalized stream function amplitude $\psi/c'h_s$ equals about 0.9. Further increase in wave amplitude brings increases in wave width, whereas weakly nonlinear theory shows width to decrease monotonically with wave amplitude.

Data suggest that the observed solitary wave had trapped thunderstorm air which was cooler and drier than the wave's ambient environment and thus, being more dense, leaked out the rear of the wave. The presence of this cool pool of air behind the wave can complicate the interpretation of measurements, if they are made only with instruments near the ground, because temperature drop and wind shift data might be misinterpreted as evidence of an advancing gravity current on top and in advance of which wave-like perturbations can form. However, observations with tall-tower and Doppler radar show that this pool of air is very shallow (less than 100 m) air leaking out the wave. Furthermore, the thunderstorm outflow appears to be guided by the wave and to flow down the wave's axis.

The results of this study suggest a scenario for the evolution of the solitary wave (Fig. 21). A thunderstorm downdraft generates a gravity current and a horizontal rotor at its leading edge. If the gravity current and the rotor are also embedded in an inversion layer, they launch a wave-like disturbance that propagates at speeds determined by wave amplitude and the vertical profile of wind and virtual potential temperature of the ambient environment. But because the gravity current front has a speed that is dependent on the depth of the current, and because this depth is continually decreasing, the frontal speed will constantly diminish, thus allowing the wave to propagate out ahead of the current. As the wave propagates away from the gravity current, it drags the vortex of outflow along with it, separating the vortex from its source. The wave and circulating outflow air continue to propagate
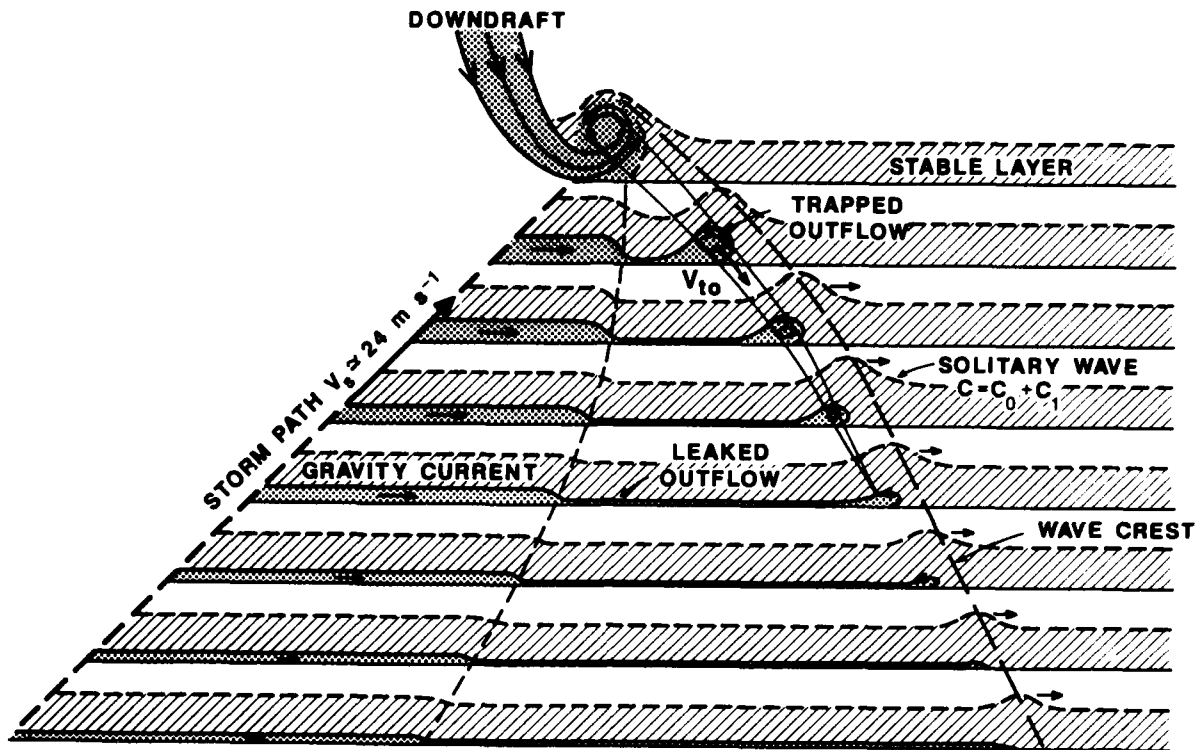
Figure 21. A scenario for the evolution of the thunderstorm-generated solitary wave.

away at velocities faster than any wave of small amplitude, and thus can leave the gravity current farther and farther behind. The recirculating trapped air in the wave creates strong shear near the earth's surface. However, as the trapped outflow slowly leaks out the rear of the wave, leaving behind a shallow pool of cool air, its amplitude decreases. After the outflow air is completely gone, the wave can continue on as a wave of permanent form, if energy loss due to ground friction and radiation can be ignored. If the part of the troposphere that overlies the inversion layer is not neutrally stable, wave energy will be radiated away from the inversion layer. Furthermore, because the inversion layer would have finite horizontal extent, especially if formed

by the cold air of thunderstorm outflows, it is expected that the solitary wave would dissipate upon encountering the boundaries of the pool of cool air. There is the possibility that some of the wave energy might be reflected, but this would be small because the change in inversion characteristics is not abrupt.

Recently Chimonas and Nappo (1987) gave a different interpretation for the generation of this wave. They concluded that all its well-defined characteristics are consistently modeled as a thunderstorm-generated bow wave, ducted in the boundary layer. Furthermore, they suggested that secondary features, such as the later onset of turbulence, the solitary echo in the radar return, and the apparent rarity of such events, can also be understood through a bow wave model. Their results are based on the observations reported by Doviak and Ge (1984) and it is hoped that the more complete data analyses and comparisons with nonlinear gravity wave theories, reported herein, have helped to resolve some of the features of the data that puzzled Chimonas and Nappo as well as us.

We have no conclusive evidence to date that solitary or gravity waves have been a cause or a contributing factor of fatal accidents. Nevertheless, the data, as meager as they are, suggest that strongly nonlinear solitary waves can pose a hazard to safe flight and may have caused accidents. Thus, they should be studied both experimentally and theoretically. Furthermore, because it is the strongly nonlinear waves that pose the threat, theoretical studies should resort to numerical models. Experiments must employ equipment, such as tall towers, Doppler radar, and aircraft, that can provide the unambiguous observations far above the ground.

APPENDIX A:

Upper-Layer Solution

For an upper-layer of constant density the vertical velocity $W(x,z,\tau)$ satisfies Laplace's equation

$$\frac{\partial^2 W}{\partial X^2} + \frac{\partial^2 W}{\partial z^2} = 0 \qquad\qquad\qquad \text{(A.1a)}$$

subject to the boundary conditions,

$$W(X,z,\tau) \to 0 \qquad\qquad \text{as } z \to \infty, \qquad\qquad \text{(A.1b)}$$

$$W(X,z,\tau) = w(\xi,z,\tau) \qquad \text{at } z = h \qquad\qquad \text{(A.1c)}$$

where $w(\xi,z,\tau)$ is the lower-layer solution and $\xi \equiv \epsilon X$. Since W_1 satisfies Laplace's equation to $O(\epsilon^3)$, the boundary condition (A.1c) can be expressed as

$$\epsilon^2 W_1(X,h,\tau) = \epsilon^2 w_1(\xi,h,\tau) + \epsilon^3 w_2(\xi,h,\tau) \qquad\qquad \text{(A.2a)}$$

to third order in ϵ in which $\xi \equiv \epsilon X$. Therefore

$$w_2(\xi,h,\tau) = 0 \qquad\qquad\qquad \text{(A.2a')}$$

and

$$W_1(X,h,\tau) = w_1 = -\frac{\partial f}{\partial \xi}(\xi,\tau) = -\frac{1}{\epsilon}\frac{\partial f(X,\tau)}{\partial X}, \qquad\qquad \text{(A.2b)}$$

$$W_1(X,z,\tau) \to 0 \qquad\qquad\qquad \text{as } z \to \infty$$

where $f(X,\tau) = \psi_0 \lambda^2/(X^2+\lambda^2)^2$. This set of boundary conditions and (A.1a) define a Dirichlet problem whose general solution is given in many mathematical texts (e.g., Hildebrand, 1956, p. 453). The solution $W_1(X,z,\tau)$ satisfying these boundary conditions is

$$W_1(X,z,\tau) = -\frac{1}{\varepsilon\pi} \int_0^\infty \left[e^{-k(z-h)} \int_{-\infty}^{+\infty} \frac{\partial f(X',\tau)}{\partial X'} \cos k(X'-X)dX' \right] dk. \qquad (A.3)$$

Integrating the inner integral by parts and then reversing the order of integration, we obtain

$$W_1(X,z,\tau) = -\frac{1}{\varepsilon\pi} \int_{-\infty}^{+\infty} f(X',\tau) \left[\int_0^\infty k e^{-k(z-h)} \sin k(X'-X)dk \right] dX'. \qquad (A.4)$$

The inner integral can be evaluated (Gradshteyn and Ryzhik, 1965, p. 490), yielding

$$W_1(X,z,\tau) = \frac{2}{\varepsilon\pi} \int_{-\infty}^{+\infty} \frac{f(X',\tau)\,(X-X')\,(z-h)}{[(X-X')^2 + (z-h)^2]^2} dX'. \qquad (A.5)$$

APPENDIX B:

Eigenfunction Solution

We seek a second-order solution to the eigenfunction equation

$$\phi'' + \frac{N^2(o)}{c_0^2} e^{-bz} \phi = 0 \qquad (3.13)$$

by using the iterative method of Stodola and Vianello (Hildebrand, 1956, p. 218). We first write Eq. (3.13) in the form

$$\phi'' = -K^2 e^{-bz} \phi \qquad (B.1)$$

where $K^2 \equiv N^2(o)/c_0^2$ is the eigenvalue that needs to be determined along with the eigenfunction ϕ. Equation (B.1) and the boundary conditions constitute a Sturm-Liouville system which determines a set of eigenvalues $K^2(n)$ ($n = 1,2,3,...$) and consequently a set of wavespeeds $c_0^{(n)}$ to each of which there is a set (modes) of eigenfunctions $\phi^{(n)}$ all of which are solutions to (B.1). We are most interested in the dominant mode $\phi^{(1)}$ corresponding to the smallest eigenvalue $K^2(1)$. The method of Stodola and Vianello is one that leads to an estimate of the smallest eigenvalue. To implement this iterative technique we first replace ϕ on the right side of (B.1) with a conveniently chosen first-order approximation ϕ_1. We shall henceforth delete the superscript (n) but it should be understood that the solutions we seek correspond only to the dominant mode. We choose for ϕ_1 the function

$$\phi_1 = \sin az, \qquad a = \frac{\pi}{2h} \qquad (B.2)$$

which is our first-order solution (2.44) when Eq. (2.45b) is substituted into it. We then integrate (B.1), after (B.2) is substituted on the right side, to obtain

$$\phi' = \frac{K^2 e^{-bz}}{(a^2+b^2)} [b \sin (az) + a \cos (az)] + S_1 \qquad (B.3)$$

where S_1 is an integration constant. Integrating once again we obtain

$$\phi(z) = \frac{K^2 e^{-bz}}{(a^2+b^2)^2} [(a^2-b^2)\sin(az)-2ab \cos(az)] + S_1 z + S_2. \qquad (B.4)$$

S_1, S_2, the integration constants, are to be determined from the boundary conditions,

$$\phi(o) = 0 \qquad (B.5a)$$

$$\phi'(h) = 0. \qquad (B.5b)$$

From boundary condition (B.5a) we find that

$$S_2 = \frac{2abK^2}{(a^2+b^2)^2} ,$$

and from boundary condition (B.5b) we obtain

$$S_1 = - \frac{bK^2 e^{-bh}}{(a^2+b^2)} .$$

Thus the eigenfunction, at the second iteration, is

$$\phi_2(z) = K^2 \left\{ \frac{e^{-bz}}{(a^2+b^2)^2} \left[(a^2-b^2)\sin(az) - 2ab\cos(az) \right] \right.$$

$$(B.6)$$

$$\left. - \frac{bze^{-bh}}{(a^2+b^2)} + \frac{2ab}{(a^2+b^2)^2} \right\} \equiv K^2 f_2(z)$$

If this process is repeated indefinitely wherein $\phi_{n-1}(z)$ is substituted on the right side of (B.1) and the nth iterative solution $\phi_n(z)$ is obtained, it can be shown that the ratio $f_n(z)/\phi_n(z)$ converges exactly to the smallest eigenvalue K and hence ϕ_n converges to the dominant eigenfunction. An estimated eigenvalue K_2 is obtained at the second iteration by equating the integrals

$$\int_0^h \phi_1(z)dz = \int_0^h \phi_2(z)dz \equiv K_2^2 \int_0^h f_2(z)\,dz \qquad (B.7)$$

so that the solutions ϕ_1, ϕ_2 agree in an integral sense.

Solving (B.7) for K_2^2 we have for our estimate

$$K_2^2 = 14.35 \text{ km}^{-2} = 14.35 \times 10^{-6} \text{ m}^{-2} \qquad (B.7a)$$

of K^2 and so our second-order estimate of wave speed is

$$c_{o2} = N(o)/K_2 = 9.6 \text{ m s}^{-1}. \qquad (B.7b)$$

Normalizing $\phi_2(z)$ so that $\phi_2(h) = 1$ we obtain the normalized eigenfunction

$$\phi_2(z) = 1.23 - 0.17z - e^{-bz}[0.99\sin(az) + 1.23\cos(az)] \qquad (B.8)$$

when

$$0 < z < 1.14 \text{ km}.$$

This solution is plotted in Fig. B.1. To ascertain the accuracy of this approximation Eq. (B.1) has been numerically integrated from the top down using the Runge-Kutta method and, initially, the estimate (B.7a) as a trial
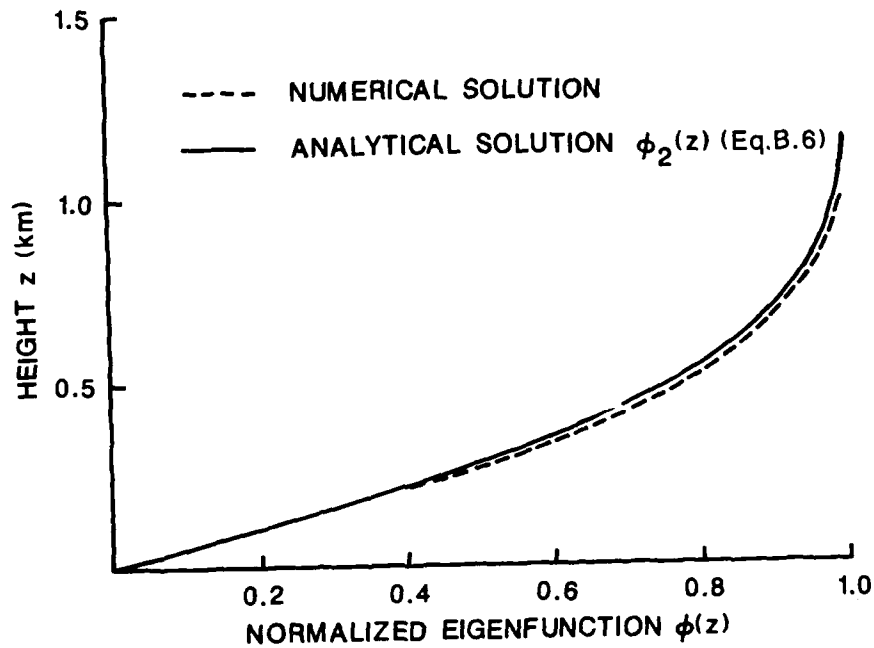

Figure B.1. Comparison of the analytic eigenfunction solution $\phi_2(z)$ and that estimated through numerical integration using iterative procedure.

eigenvalue, and then iterating eigenvalues until the eigenfunction ϕ satisfies the boundary condition $\phi = 0$ at $z = 0$ to the sixth decimal place. The resulting eigenvalue is

$$K^2 = 1.345 \times 10^{-5} \ m^{-2} \qquad\qquad (B.9)$$

which is close to that initially estimated. The numerically evaluated eigenfunction is also plotted on Fig. B.1 demonstrating that Eq. (B.8) is an excellent approximation to the more exact numerical solution.

Using the eigenvalue in Eq. (B.9) to compute c_0 we find that

$$c_0 = \frac{N(o)}{K} = 9.9 \ m \ s^{-1} \qquad\qquad (B.10)$$

which compares reasonably well with our second-order estimate $9.6 \ m \ s^{-1}$ in Eq. (B.7b).

Now to determine the parameters α, β for the steady-state nonlinear wave Eq. (2.25) we need to evaluate (2.24). The derivative $\phi_2'(z)$,

$$\phi_2'(z) = -0.17 + e^{-bz}[4.55 \sin(az) + 2.18 \cos(az)] \ km^{-1} \qquad (B.11)$$

is needed only in the approximate solutions for α, β given by (2.40). Substituting (B.9) into (2.40) and numerically integrating we find

$$\alpha_2 = 2.39 \times 10^{-3} \ m^{-1} \qquad\qquad (B.12a)$$

$$\beta_2 = 3.49 \times 10^3 \ m^2 s^{-1}. \qquad\qquad (B.12b)$$

APPENDIX C:

A Modified Mach Relation for Amplitude Dependent Wave Speeds

Consider a storm moving in a homogeneous medium at a constant velocity V_s along a straight line and continuously generating a gravity wave disturbance which propagates with a time dependent velocity $c(t)$ related to its time dependent height (i.e., its amplitude). Because theory shows that gravity waves of finite amplitude have speeds faster than infinitesimal waves, and because it is assumed that amplitude decreases as the wave progresses away from the source, the wave front will have the curvature shown in Fig. C.1. Paths of
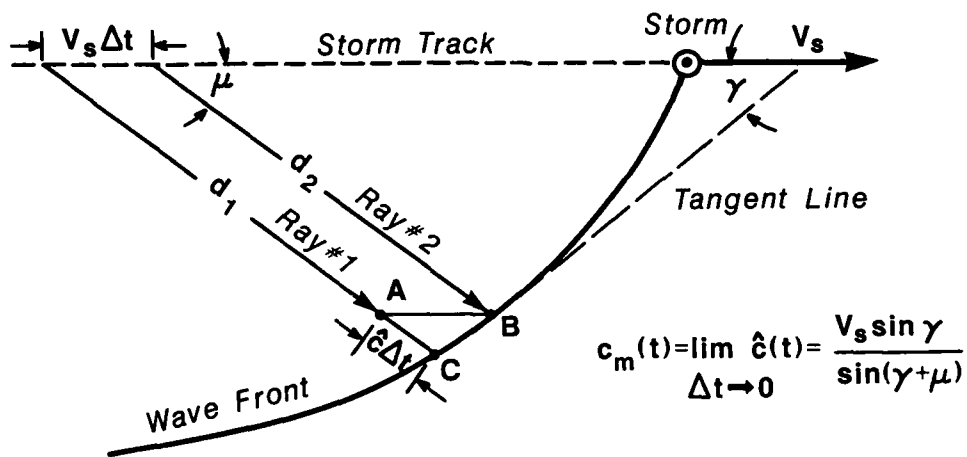

Figure C.1. Geometric construction to derive a modified Mach relation.

energy travel (rays) in homogeneous media are straight (Whitham, 1974, Ch. 14, p. 254) so rays will be parallel to one another and intersect the source path at an angle μ. Thus after time t (reference time t=0 is when $d_2 = 0$) the wave front would have propagated along ray #1 a distance

$$d_1 = \int_0^{t+\Delta t} c(t)dt = \int_0^t c(t)dt) + \int_t^{t+\Delta t} c(t)dt \simeq \int_0^t c(t)dt + \hat{c}(t)\Delta t,$$

where $\hat{c}(t)$ is the average wave speed along the incremental path A-C whereas the distance traveled along ray #2 is

$$d_2 = \int_0^t c(t)dt$$

The limit

$$\lim_{\Delta t \to 0} \frac{d_1 - d_2}{\Delta t} = c(t)$$

defines the wave speed at B at the time t. Now construct a line tangent to the front at B and apply the law of sines to the triangle ABC, that is,

$$\frac{\hat{c}(t)\Delta t}{\sin(\gamma)} = \frac{V_s \Delta t}{\sin(180-\gamma-\mu)} = \frac{V_s \Delta t}{\sin(\gamma+\mu)},$$

to derive the relation

$$c(t) = \frac{V_s \sin\gamma}{\sin(\gamma+\mu)} \qquad (C.1)$$

in the limit $\Delta t \to 0$, where γ is the angle between the source path and the tangent line.

REFERENCES

Abdullah, A.J., 1955: The atmospheric solitary wave. <u>Bull. Amer. Meteor.</u>
<u>Soc.</u> 36, 515-518.

Abramowitz, M., and I.A. Stegun, 1968: Handbook of Mathematical Functions.
NBS Appl. Math. Ser. 55, 7th printing. Super. Doc., U.S. Gov't. Printing
Office, Washington, D.C. 20402, 10046 pp.

Anderson, K.W., and B.A.J. Clark, 1979: Wind shear in Australia. <u>Avia. Saf.</u>
<u>Dig.</u> 106, 14-20.

Anderson, K.W., and B.A.J. Clark, 1981: A study of wind shear effects on air-
craft operations and safety in Australia. Systems Report 24, Aeron. Res.
Lab., Dept. of Defense, Melbourne, Victoria, Aust.

Benjamin, T.B., 1966: Internal waves of finite amplitude and permanent form.
<u>J. Fluid Mech.</u> 25, 241-270.

Benjamin, T.B., 1967: Internal waves of permanent form in fluids of great
depth. <u>J. Fluid Mech.</u> 29, 559-592.

Benney, D.J., 1966: Long non-linear waves in fluid flows. <u>J. Math. Phys.</u> 45,
52-63.

Boussinesq, M.J., 1871: Théorie de l'intumescence liquide, appelée onde soli-
taire ou de translation, se propageant dans un canal rectangulaire. <u>Acad.</u>
<u>Sci. Paris, Comptes Rendus</u> 72, 755-759.

Caracena, F., R. Ortiz, and J.A. Augustine, 1986: The crash of Delta
Flight 191 at Dallas-Fort Worth International Airport on 2 August 1985:
Multiscale analyses of weather conditions. NOAA Tech. Rept. ERL 430-ESG2,
U.S.D.O.C./NOAA Environmental Research Laboratories, Boulder, CO, 33 pp.

Chen, H.H., Y.C. Lee, and N.R. Pereira, 1979: Algebraic internal wave solitons and the integrable Calogero-Moser-Sutherland N-body problem. _Phys. Fluids_ 22, 187-188.

Chen, S., 1985: A theoretical analysis and comparison of the theory and observation of wind and pressure fields in an atmospheric solitary wave. M.S. Thesis, University of Oklahoma, Department of Meteorology, Norman, OK.

Chimonas, G., and C.J. Nappo, 1987: A thunderstorm bow wave. _J. Appl. Sci._ 44, 533-541.

Christie, D.R., and K.J. Muirhead, 1982: Solitary waves: a hazard to aircraft operating at low altitudes. Report, Res. School of Earth Sci., Australian National University, 33 pp.

Christie, D.R., and K.J. Muirhead, 1983a: Solitary wavaes: a hazard to aircraft operating at low altitudes. _Aust. Meteor. Mag._ 31, 97-109.

Christie, D.R., and K.J. Muirhead, 1983b: Solitary waves, a low-level wind shear hazard to aviation. _Int. J. Aviat. Saf.,_ 1, Sept., 169-190.

Christie, D.R., and K.J. Muirhead, 1985: Solitary waves and low-altitude wind shear in Australia. _Avia. Saf. Dig._ 123, 3-8.

Christie, D.R., K.J. Muirhead, and A.L. Hales, 1978: On solitary waves in the atmosphere. _J. Atmos. Sci._ 35, 805-825.

Christie, D.R., K.J. Muirhead, and A.L. Hales, 1979: Intrusive density flows in the low troposphere: a source of atmospheric solitons. _J. Geophys. Res._ 84, 4959-4970.

Christie, D.R., K.J. Muirhead, and R.H. Clarke, 1981: Solitary waves in the lower atmosphere. _Nature_ 293, 46-49.

Clarke, R.H., 1972: The morning glory: an atmospheric hydraulic jump. _J. Appl. Meteor._ 11, 304-311.

Clarke, R.H., R.K. Smith, and D.G. Reid, 1981: The morning glory of the Gulf of Carpentaria: an atmospheric undular bore. Mon. Wea. Rev. 109, 1726-1750.

Corliss, W.R., 1977: Handbook on unusual natural phenomena. Published by The Sourcebook Project, Glen Arm, MD 21057, 542 pp.

Crook, N.A., and M.J. Miller, 1985: A numerical and analytical study of atmospheric undular bores. Quart. J. Res. Meteor. Soc. 111, 225-242.

Crook, N.A., 1986: The effect of ambient stratification and moisture on the motion of atmospheric undular bores. J. Atmos. Sci. 43, 171-181.

Crook, N.A., 1987: Trapping of low level internal gravity waves. Paper submitted to J. Atmos. Sci.

Cummins, P.F., and P.H. Le Blond, 1984: Analysis of internal solitary waves observed in Davis Strait. Atmosphere-Ocean 22(2), Canad. Meteor. and Oceanic Soc., 173-192.

Davis, R.E., and A. Acrivos, 1967a: Solitary internal waves in deep water. J. Fluid Mech. 29, 593-607.

Davis, R.E., and A. Acrivos, 1967b: The stability of oscillatory internal waves. J. Fluid Mech. 30, 723-736.

Dodd, R.K., J.C. Eilbeck, J.D. Gibbon, and H.C. Morris, 1982: Solitons and Nonlinear Wave Equations. Academic Press, Orlando, Florida, 630 pp.

Doviak, R.J., and M. Berger, 1980: Turbulence and waves in the optically clear planetary boundary layer resolved by dual-Doppler radars. Radio Sci. 15, 297-317.

Doviak, R.J., and R.S. Ge, 1984: An atmospheric solitary gust observed with a Doppler radar, a tall tower and a surface network. J. Atmos. Sci. 41, 2559-2573.

Doviak, R.J., and D.S. Zrnic', 1984: Doppler Radar and Weather Observations. Academic Press, Orlando, Florida, 458 pp.

Doviak, R.J., and J.T. Lee, 1985: Radar for storm forecasting and weather hazard warning. J. Aircraft 22, 1059-1064.

Droegemeier, K.K., and R.B. Whilhelmson, 1987: Numerical simulation of thunderstorm outflow dynamics. J. Atmos. Sci. 44(8), 1180-1210.

Egger, J., 1983: The morning glory: a nonlinear phenomenon. Meso. Meteor. Theories, Obs. Model, NATO ASI series C 114, 339-384.

Elmore, K.L., J. McCarthy, W. Frost, and H.P. Chang, 1986: A high resolution spatial and temporal multiple Doppler analysis of a microburst and its application to aircraft flight simulation. J. Clim. Appl. Meteor. 25, 1398-1425.

Fujita, T.T., and R.M. Wakimoto, 1983: Microbursts in JAWS depicted by Doppler radars, PAM, and aerial photographs. Preprints, 21st Conf. on Radar Meteorology, Edmonton, Amer. Meteor. Soc., Boston, MA, 638-645.

Fulton, Richard, 1987: Observations of the interactions of a nocturnal thunderstorm outflow with a stable environment. M.S. Thesis, University of Oklahoma, Department of Meteorology, Norman, OK.

Gossard, E.E., 1983: Aircraft hazard assessment from a clear-air radar and meteorological tower study of gravity wave events. U.S. National Oceanic and Atmospheric Admin., Boulder, CO (PB83-257139, National Tech. Info. Service, Springfield, VA 22161) 18 pp.

Gradshteyn, I.S., and I.M. Ryzhik, 1965: Table of integrals, series, and products. Academic Press, New York, 1086 pp.

Haase, S., and R.K. Smith, 1984: Morning glory wave clouds in Oklahoma: a case study. Mon. Wea. Rev. 112, 2078-2089.

Hildebrand, F.B., 1956: Advanced Calculus for Engineers. Prentice Hall, Englewood Cliffs, NJ, 594 pp.

Keulegan, G.H., 1953: Characteristics of internal solitary waves. J. Res.
Natl. Bur. Stand. 51, 133-140.

Keulegan, G.K., and L.H. Carpenter, 1961: An experimental study of internal
progressive oscillatory waves. Natl. Bur. Stand. Rep. No. 7319.

Koop, C.G., and G. Butler, 1981: An investigation of internal solitary waves
in a two-fluid system. J. Fluid Mech. 112, 225-251.

Korteweg, D.J., and G. de Vries, 1895: On the change of form of long waves
advancing in a rectangular canal and on a new type of long stationary
waves. Phil. Mag. 39, 422-443.

Lee, J.T., and R.J. Doviak, 1981: Radar for storm forecasting and weather
hazard warning. J. Aircraft 22, 1059-1064.

Lee, J.T., J. Stokes, Y. Sasaki, and T. Baxter, 1978: Thunderstorm gust
fronts--Observations and modeling. FAA Report No. FAA-RD-78-145, Systems
Research and Development Service, Washington, DC 20590.

Levi-Civita, T., 1925: Détermination rigoureuse des ondes permanentes
d'ampleur finie. Math. Ann. 93, 264-314.

Long, R.R., 1956: Some aspects of the flow of stratified fluids. Part I: a
theoretical investigation. Tellus 5, 42-47.

Long, R.R., 1965: On the Boussinesq approximation and its role in the theory
of internal waves. Tellus 17, 46-52.

Mahoney, W.P., III, 1987: Gust front characteristics and the kinematics asso-
ciated with interacting thunderstorm outflows. Submitted to the Mon. Wea.
Rev., July 1987.

Maslowe, S.A., and L.G. Redekopp, 1980: Long nonlinear waves in stratified
shear flows. J. Fluid Mech. 101, 321-348.

Matsuno, Y., 1979: Exact multi-soliton solution of the Benjamin-Ono equation.
J. Phys. A, Math. Gen. 12, 619-621.

Maxworthy, T., 1980: On the formation of nonlinear internal waves from gravi-
tational collapse of mixed regions in two and three dimensions. J. Fluid
Mech. 96, 47-64.

Neal, A.B., I.J. Butterworth, and K.M. Murphy, 1977: The morning glory.
Weather 32, 176-183.

Ono, H., 1975: Algebraic solitary waves in stratified fluids. J. Phys. Soc.
Japan 39, 1082-1091.

Peters, A.S., and J.J. Stoker, 1960: Solitary waves in liquids having non-
constant density. Pure Appl. Math. 13, 115-164.

Rayleigh, Lord., 1876: On waves. Phil. Mag. 1, 257-279.

Rudich, R.D., 1986: Weather-involved U.S. air carriers accidents 1962-1984--A
compendium and brief summary. Preprints AIAA 24th Aerospace Sciences Meet-
ing, Paper # AIAA-86-0327, American Institute of Aeronautics and Astro-
nautics, New York, NY, 7 pp.

Rust, W.D., and R.J. Doviak, 1982: Radar research on thunderstorms and light-
ning. Nature 297, 461-468.

Scott Russell, J., 1840: Experimental researches into the laws of certain hy-
drodynamic phenomena that accompany the motion of floating bodies, and have
not been previously reduced into conformity with known laws of the resist-
ance of fluids. Edinb. Roy. Soc. Trans. 14, 47-109, + 2 plates.

Shreffler, J.H., and F.S. Binkowski, 1981: Observations of pressure jump
lines in the midwest, 10-12 August 1976. Mon. Wea. Rev. 109, 1713-1725.

Stewart, O., 1958: Danger in the Air. Philosophical Library, New York, NY,
55-63.

Ter-Krikorov, A.M., 1963: Théorie exacte des ondes longues stationnair dans
un liquide hétérogene. J. Méc. 2, 351-376.

Tung, K.K., D.R.S. Ko, and J.J. Chang, 1981: Weakly nonlinear internal waves in shear. Stud. Appl. Math. 65, 189-221.

Tung, K.K., T.F. Chan, and T. Kubota, 1982: Large amplitude internal waves of permanent form. Stud. Appl. Math. 66, 1-44.

von Karman, T., 1940: The engineer grapples with nonlinear problems. Bull. Am. Math. Soc. 46, 615-683.

Whitham, G.B., 1974: Linear and Nonlinear Waves. John Wiley & Sons, New York, 636 pp. (Ch. 14).

Wilson, J.W., R.D. Roberts, C. Kessinger, and J. McCarthy, 1984: Microburst wind structure and evaluation of Doppler radar for airport wind shear detection. J. Clim. Appl. Meteor. 23, 898-915.

Woodfield, A.A., 1983: Wind shear and vortex wake research in U.K. 1982. Proc. Sixth Annual Workshop on Meteorological and Environmental Inputs to Aviation Systems, W. Frost and D.W. Camp, Eds., NASA Rept. CP-2274 and Dept. of Trans. Rept. No. DOT/FAA/RD-82/72, 66-83.

Yih, C.-S., 1960: Gravity waves in a stratified fluid. J. Fluid Mech. 8, 481-508.

Zabusky, N.J., and M.D. Kruskal, 1965: Interaction of "solitons" in a collisionless plasma and the recurrence of initial states. Phys. Rev. Lett. 15, 240-243.